

MOMENT-PRESERVING COMPUTATIONAL APPROACH FOR HIGH ENERGY CHARGED PARTICLE TRANSPORT

Anil Kant Prinja and David Andrew Dixon

**University of New Mexico
MSC01 1120, Chemical and Nuclear Engineering Department
Albuquerque, NM 87131**

16 May 2016

Final Report

APPROVED FOR PUBLIC RELEASE; DISTRIBUTION IS UNLIMITED.



**AIR FORCE RESEARCH LABORATORY
Space Vehicles Directorate
3550 Aberdeen Ave SE
AIR FORCE MATERIEL COMMAND
KIRTLAND AIR FORCE BASE, NM 87117-5776**

NOTICE AND SIGNATURE PAGE

Using Government drawings, specifications, or other data included in this document for any purpose other than Government procurement does not in any way obligate the U.S. Government. The fact that the Government formulated or supplied the drawings, specifications, or other data does not license the holder or any other person or corporation; or convey any rights or permission to manufacture, use, or sell any patented invention that may relate to them.

This report was cleared for public release by the PRS OPSEC Office and is available to the general public, including foreign nationals. Copies may be obtained from the Defense Technical Information Center (DTIC) (<http://www.dtic.mil>).

AFRL-RV-PS-TR-2016-0102 HAS BEEN REVIEWED AND IS APPROVED FOR PUBLICATION IN ACCORDANCE WITH ASSIGNED DISTRIBUTION STATEMENT.



Adrian Wheelock
Program Manager, AFRL/RVBXR



Dr. Thomas R. Caudill, Acting Chief
AFRL Battlespace Environment Division

This report is published in the interest of scientific and technical information exchange, and its publication does not constitute the Government's approval or disapproval of its ideas or findings.

REPORT DOCUMENTATION PAGE				<i>Form Approved</i> OMB No. 0704-0188	
Public reporting burden for this collection of information is estimated to average 1 hour per response, including the time for reviewing instructions, searching existing data sources, gathering and maintaining the data needed, and completing and reviewing this collection of information. Send comments regarding this burden estimate or any other aspect of this collection of information, including suggestions for reducing this burden to Department of Defense, Washington Headquarters Services, Directorate for Information Operations and Reports (0704-0188), 1215 Jefferson Davis Highway, Suite 1204, Arlington, VA 22202-4302. Respondents should be aware that notwithstanding any other provision of law, no person shall be subject to any penalty for failing to comply with a collection of information if it does not display a currently valid OMB control number. PLEASE DO NOT RETURN YOUR FORM TO THE ABOVE ADDRESS.					
1. REPORT DATE (DD-MM-YYYY) 16-05-2016		2. REPORT TYPE Final Report		3. DATES COVERED (From - To) 28 Apr 2011 – 28 Apr 2016	
4. TITLE AND SUBTITLE Moment-Preserving Computational Approach for High Energy Charged Particle Transport				5a. CONTRACT NUMBER FA9453-11-1-0276	
				5b. GRANT NUMBER	
				5c. PROGRAM ELEMENT NUMBER 62601F	
6. AUTHOR(S) Anil Kant Prinja and David Andrew Dixon				5d. PROJECT NUMBER 1010	
				5e. TASK NUMBER PPM00011354	
				5f. WORK UNIT NUMBER EF004076	
7. PERFORMING ORGANIZATION NAME(S) AND ADDRESS(ES) University of New Mexico MSC01 1120, Chemical and Nuclear Engineering Department Albuquerque, NM 87131				8. PERFORMING ORGANIZATION REPORT NUMBER	
9. SPONSORING / MONITORING AGENCY NAME(S) AND ADDRESS(ES) Air Force Research Laboratory Space Vehicles Directorate 3550 Aberdeen Avenue SE Kirtland AFB, NM 87117-5776				10. SPONSOR/MONITOR'S ACRONYM(S) AFRL/RVBXR	
				11. SPONSOR/MONITOR'S REPORT NUMBER(S) AFRL-RV-PS-TR-2016-0102	
12. DISTRIBUTION / AVAILABILITY STATEMENT Approved for public release; distribution is unlimited. (OPS-16-12062 dtd 13 June 2016)					
13. SUPPLEMENTARY NOTES					
14. ABSTRACT This report covers the work under the University of New Mexico (UNM)/Air Force Research Laboratory research grant FA9453-11-1-0276 during the period of April 2011 to April 2016. The focus of the research grant was the theoretical development and implementation of a novel, single-event Monte Carlo charged particle transport method that is accurate and efficient. In addition, detector modeling and simulation was completed for various DsX instruments including CEASE, HEPS, and LEESA, with the intention of establishing such a modeling and simulation capability at UNM.					
15. SUBJECT TERMS Reduced Physics Models, Geant4, CEASE					
16. SECURITY CLASSIFICATION OF:			17. LIMITATION OF ABSTRACT Unlimited	18. NUMBER OF PAGES 88	19a. NAME OF RESPONSIBLE PERSON Adrian Wheelock
a. REPORT Unclassified	b. ABSTRACT Unclassified	c. THIS PAGE Unclassified			19b. TELEPHONE NUMBER (include area code)

This page is intentionally left blank.

Table of Contents

1. SUMMARY.....	1
2. INTRODUCTION.....	1
3. BACKGROUND.....	2
3.1. The Analog Problem.....	3
3.2. Condensed History	4
3.3. Reduced Order Physics Models.....	5
4. METHODS, ASSUMPTIONS, AND PROCEDURES	7
4.1. Analog Differential Cross-Sections and the Analog Transport Model	8
4.1.1. Elastic and Inelastic Analog Differential Cross-Sections	8
4.1.2. Analog Transport Model.....	11
4.2. Moment-Preserving Method.....	13
4.2.1. Reduced Order Physics Differential Cross-Sections	15
4.2.2. Derivation of the Reduced Order Physics Collision Operators	16
4.2.3. Generation of the Discrete and Hybrid Differential Cross-Sections	18
4.3. Development of the Geant4 Toolkit Moment-Preserving Method Classes.....	22
4.3.1. Physics Processes.....	22
4.3.2. Physics Models	22
4.3.3. Cross-Section Library and Data Processing	23
5. RESULTS AND DISCUSSION.....	24
5.1. Angular Distributions and Energy Spectra.....	25
5.1.1. Angular Distributions.....	26
5.1.2. Energy Spectra	31
5.1.3. Efficiencies for Thin Slab Problems	35
5.2. Longitudinal and Lateral Distributions.....	37
5.3. 1-D and 2-D Dose Calculations.....	45
5.3.1. One-Dimensional Depth-Dose Profiles	46
5.3.2. Two-Dimensional Dose Deposition.....	49
5.4. Comparison with Experiment.....	55
5.4.1. Energy Deposition Profiles	55
5.4.2. Charge Deposition Profiles	63
5.5. CEASE Response Function Calculation.....	67

5.6. Detector Modeling and Simulation.....	68
6. CONCLUSIONS	69
REFERENCES	71
LIST OF SYMBOLS, ABBREVIATIONS, AND ACRONYMS	77

List of Figures

Figure 1: Electron interaction diagrams for elastic and inelastic scattering [24].	8
Figure 2: Partial-wave elastic differential cross-sections for various energy electrons scattering with aluminum (left) and gold (right) nuclei.	11
Figure 3: Thin slab problem setup.	26
Figure 4: Transmitted angular distributions for 10000-keV electrons on aluminum and gold. ...	27
Figure 5: Transmitted angular distributions for 1000-keV electrons on aluminum and gold.	28
Figure 6: Impact of slab thickness on transmitted angular distributions on 1000-keV electrons on gold.	29
Figure 7: Impact of slab thickness on reflected angular distributions for 10000-keV electrons on aluminum.	30
Figure 8: Impact of slab thickness on reflected angular distributions for 1000-keV electrons on gold.	31
Figure 9: Impact of slab thickness on transmitted energy-loss spectra for 10000-keV electrons on aluminum.	32
Figure 10: Impact of slab thickness on transmitted energy-loss spectra for 1000-keV electrons on gold.	33
Figure 11: Impact of slab thickness on reflected energy-loss spectra for 10000-keV electrons on aluminum.	34
Figure 12: Impact of slab thickness on reflected energy-loss spectra for 1000-keV electrons on gold.	35
Figure 13: Infinite medium problem setup.	38
Figure 14: Comparison of longitudinal distributions for 10000-keV electrons after traveling a distance of 100 (top left), 300 (top right), 1000 (bottom left), and 3000 (bottom right) analog elastic mfps.	40
Figure 15: Comparison of lateral distributions for 10000-keV electrons after traveling a distance of 100 (top left), 300 (top right), 1000 (bottom left), and 3000 (bottom right) analog elastic mfps.	41
Figure 16: Comparison of longitudinal distributions for 1000-keV electrons after traveling a distance of 100 (top left), 300 (top right), 1000 (bottom left), and 3000 (bottom right) analog elastic mfps.	42
Figure 17: Comparison of lateral distributions for 1000-keV electrons after traveling a distance of 100 (top left), 300 (top right), 1000 (bottom left), and 3000 (bottom right) analog elastic mfps.	43
Figure 18: Comparison of longitudinal distributions for 100-keV electrons after traveling a distance of 100 (top left), 300 (top right), 1000 (bottom left), and 3000 (bottom right) analog elastic mfps.	44
Figure 19: Comparison of lateral distributions for 100-keV electrons after traveling a distance of 100 (top left), 300 (top right), 1000 (bottom left), and 3000 (bottom right) analog elastic mfps.	45
Figure 20: Dose deposition profile (left) and relative error (right) for 250-keV electrons on a gold slab.	46
Figure 21: Dose deposition profile and relative error for 20000-keV e^- on H ₂ O.	47
Figure 22: Dose deposition profile (left) and relative error (right) for 150-keV electrons on a gold/aluminum slab.	48

Figure 23: Problem setup (left) and analog benchmark (right) for 150-keV electrons on a silicon cube with gold region.....	49
Figure 24: Relative error in discrete 1-Angle, 1-Energy model (top left), discrete 2-Angles, 1-Energy model (top left), discrete 4-Angles, 1-Energy model (top left), discrete 4-Angles, 4-Energies model (top left) for 150-keV electrons on silicon/gold cube.	50
Figure 25: Problem setup (left) and analog benchmark (right) for 10000-keV electrons on a water cube with bone region.	51
Figure 26: Relative error in discrete 4-Angles, 4-Energies model (left) and discrete 8-Angles, 4-Energies model (right) for 10000-keV electrons on water/bone cube.	51
Figure 27: Relative error in hybrid 1-Angle with cutoff of 0.9, discrete 4-Energies model (left) and hybrid 1-Angle with cutoff of 0.99, discrete 4-Energies model (right) for 10000-keV electrons on water/bone cube.	52
Figure 28: Schematic for region dependent ROP DCS (left) and the relative error in dose (right) for 10000-keV electrons on a water cube with bone region.	53
Figure 29: Schematic for region dependent ROP DCS (left) and the relative error in dose (right) for 10000-keV electrons on a water cube with bone region.	53
Figure 30: Problem setup (left) and analog benchmark (right) for an isotropic source of 2500-keV electrons in a gold cube.	54
Figure 31: Relative error in discrete 1-Angle, 1-Energy model (left), discrete 2-Angles, 1-Energy model (middle) and discrete 2-Angles, 2-Energies model (right) for 2500-keV electrons in gold cube.	55
Figure 32: Comparison with Lockwood data for 1000-keV electrons normally on carbon slab..	60
Figure 33: Comparison with Lockwood data for 500-keV (left) and 1000-keV (right) electrons normally on aluminum slab.	61
Figure 34: Comparison with Lockwood data for 500-keV (left) and 1000-keV (right) electrons normally on molybdenum slab.....	61
Figure 35: Comparison with Lockwood data for 500-keV (left) and 1000-keV (right) electrons normally on tantalum slab.....	61
Figure 36: Comparison with Lockwood data for 1000-keV electrons with 60 degrees off-normal incidence on aluminum slab.....	62
Figure 37: Comparison with Lockwood data for 500-keV (left) and 1000-keV (right) with 60 degrees off-normal incidence on molybdenum slab.	62
Figure 38: Comparison with Lockwood data for 500-keV (left) and 1000-keV (right) electrons with 60 degrees off-normal incidence on tantalum slab.	63
Figure 39: Charge deposition comparison with Tabata data (left) and dose comparison (right) for 5000-keV electrons normally incident on aluminum slab.	65
Figure 40: Charge deposition comparison with Tabata data (left) and dose comparison (right) for 10000-keV electrons normally incident on aluminum slab.	65
Figure 41: Charge deposition comparison with Tabata data (left) and dose comparison (right) for 20000-keV electrons normally incident on aluminum slab.	65
Figure 42: Charge deposition comparison with Tabata data (left) and dose comparison (right) for 5000-keV electrons normally incident on gold slab.	66
Figure 43: Charge deposition comparison with Tabata data (left) and dose comparison (right) for 10000-keV electrons normally incident on gold slab.	66
Figure 44: Charge deposition comparison with Tabata data (left) and dose comparison (right) for 20000-keV electrons normally incident on gold slab.	66

Figure 45: Comparison of response functions generated using the analog model, the discrete model, and the Geant4 multiple-scattering model.	67
Figure 46: Electrons traversing the CEASE telescope.	68

List of Tables

Table 1: Efficiency gains for various ROP DCSs when simulating 1000-keV and 10000-keV electrons incident on aluminum slabs 100, 300, 1000, and 3000 mfps thick.	36
Table 2: Efficiency gains for various ROP DCSs when simulating 1000-keV and 10000-keV electrons incident on gold slabs 100, 300, 1000, and 3000 mfps thick.	36
Table 3: Average longitudinal displacement for 100-keV, 1000-keV, and 10000-keV electrons in copper traveling a distance of 100, 300, 1000, and 3000 mfps.	39
Table 4: Average lateral displacement for 100-keV, 1000-keV, and 10000-keV electrons in copper traveling a distance of 100, 300, 1000, and 3000 mfps.	39
Table 5: Efficiency gains for various discrete DCSs when calculating dose due to 250-keV, 1000-keV, and 20000-keV electrons on gold slabs.....	47
Table 6: Efficiency gains for various hybrid DCSs when calculating dose due to 250-keV, 1000-keV, and 20000-keV electrons on gold slabs.....	47
Table 7: Efficiency gains for various discrete DCSs when calculating dose due to 250-keV, 1000-keV, and 20000-keV electrons on water slabs.....	48
Table 8: Efficiency gains for various hybrid DCSs when calculating dose due to 250-keV, 1000-keV, and 20000-keV electrons on water slabs.....	48
Table 9: Efficiency gains for various discrete DCSs when calculating dose due to 150-keV electrons on silicon/gold cube.....	50
Table 10: Efficiency gains for various discrete DCSs when calculating dose due to 10000-keV electrons on water/bone cube.....	52
Table 11: Total energy deposition comparison for 500-keV and 1000-keV electrons normally incident on aluminum, molybdenum, and tantalum semi-infinite slabs.	57
Table 12: Total energy deposition comparison for 500-keV and 1000-keV electrons with 60 degrees off-normal incidence on aluminum, molybdenum, and tantalum semi-infinite slabs.....	58
Table 13: Timing results for energy deposition calculations for 500-keV and 1000-keV electrons normally incident on carbon, aluminum, molybdenum, and tantalum semi-infinite slabs...	59
Table 14: Timing results for energy deposition calculations for 500-keV and 1000-keV electrons with 60 degrees off-normal incidence on aluminum, molybdenum, and tantalum semi-infinite slabs.	60
Table 15: Timing results for charge deposition calculations for 5000-keV, 10000-keV, and 20000-keV electrons with normally incident on aluminum and gold semi-infinite slabs.	64

1. SUMMARY

This report covers the work completed under the UNM/AFRL research grant FA9453-11-1-0276 including the theoretical development and implementation of a novel electron transport method in the Geant4 toolkit, and other related work including the generation of response functions for the CEASE telescope. It has long been of interest to develop an alternative to the standard Condensed History (CH) method that is free of its inherent limitations. The Moment-Preserving method, is such an alternative and within this report the accuracy and efficiency of this method is demonstrated and contrasted with the CH method. The Moment-Preserving (MP) Monte Carlo electron transport method was developed and implemented in the Geant4 toolkit as C++ classes for constructing the libraries that are required by the MP method physics models. Given the successful implementation of the physics models, the MP method was then tested on a wide variety of problems including a theoretical test suite, experimental validations, and the CEASE particle telescope.

2. INTRODUCTION

This report covers the work completed under the UNM/AFRL research grant FA9453-11-1-0276 during the period of April 2011 to March 2015 including the primary objective, or the theoretical development and implementation of a novel electron transport method in the Geant4 toolkit, and other related work including the modeling of detectors associated with the AFRL Demonstration and Science Experiment (DsX) detectors for use in response function determination. In efforts to complete the primary objective, the Moment-Preserving (MP) Monte Carlo electron transport method was developed and implemented in the Geant4 toolkit. Specifically, C++ classes were developed for constructing the reduced order physics (ROP) differential cross-section (DCS) libraries that are required by the MP method physics models developed for the Geant4 toolkit. Given the successful implementation of the physics models, the MP method was then tested on a wide variety of problems including a theoretical test suite, experimental validations, and generation of response functions for the CEASE telescope (i.e. a DsX instrument). The motivation for MP method and the key properties are now summarized.

Analog electron transport is computationally impractical; and therefore, methods such as condensed history were developed to alleviate the computational cost associated with analog Monte Carlo electron transport. However, the condensed history method suffers from limitations inherent to the method resulting from the formulation of the method. Therefore, it is of interest to develop an advanced method that is free of the limitations of condensed history, while remaining efficient and accurate with respect to the analog transport model. The analog description of transport can be mathematically expressed in terms of the linear Boltzmann or transport equation for the phase space particle distribution function, where interaction physics is represented through total cross sections and differential cross sections for energy transfer and angular deflection. In the so-called advanced method, a reduced order transport problem is posed, but with modified cross sections such that the resulting single-event Monte Carlo simulation is computationally efficient (minutes vs. days). Underlying the approach is a method of systematically preserving energy-loss and angular deflection moments of the analog differential

cross sections and using only a finite number of these moments to reconstruct a reduced order physics differential cross section. This method is characterized by the following properties:

1. The mean free path of the reduced order physics model will be longer than the true or analog mean free path and the differential cross sections less peaked, with accuracy depending on the number of moments preserved.
2. The moment-preserving methodology will enable accuracy to systematically approach analog by incorporating increasingly higher order moments with precision.
3. By retaining the “look and feel” of the analog transport process, i.e., using approximations based on Boltzmann or integral forms of the collision operators describing interactions, collisions are exactly treated as Markov events, thereby allowing material and vacuum interfaces to be handled without algorithmic modifications in condensed history methods.
4. In aggregate, the smoother cross section variation with energy and angle as well as the correct transport mechanics will result in considerable computational savings over using strictly analog Monte Carlo simulation. We expect the savings to be such that the moment-preserving method will be computationally competitive with condensed history, but it also has the potential to be more efficient than condensed history.
5. The methodology will be independent of charged particle species and will therefore apply to species of disparate masses, such as protons and electrons.
6. The methodologies proposed here can be directly incorporated into production Monte Carlo codes such as MCNPX and Geant4 without necessitating new logic because this approach will treat charged particles similar to neutral particles with regards to transport.

Given a summary of the advanced Monte Carlo method and its’ properties, the background information necessary to understand the motivation of developing such a method is provided.

3. BACKGROUND

The need for computational charged particle transport developed from early work in charged particle transport theory, which emerged as a flourishing sub-branch of mathematical physics when fast charged particles became available to the experimentalist [2]. As computer technology improved, the problems of interest to charged particle computational physicist expanded to areas including: space physics, accelerator physics, medical physics, health physics, and electromagnetic pulses. The advantage of computational charged particle transport over analytical transport is the possibility of simulating complicated geometries and sophisticated boundary conditions or source configurations, which are all characteristics of real world applications. In other words, it is possible to simulate real, physical phenomena using charged particle transport codes. An example of such a code is the Geant4 toolkit [3] which is used frequently on problems including: design of full-scale experiments such as the Large Hadron Collider [4, 5], design of radiation therapy machines [6] as well as treatment planning systems [7], estimation of detector geometric factors [8], shielding calculations [9], and EMP calculations [10]. It is undisputed that particle transport codes play an important role in the research and development of charged particle applications and reasonable to suggest that particle transport codes will continue to play an important role into future. Therefore,

algorithmic improvements to particle transport codes are critical to improving the field of computational charged particle transport.

To make clear the impact of this work and the importance of the remaining chapters, it is necessary to provide, at least, a cursory discussion on what is meant by charged particle transport codes and the associated challenges. First, the purpose of charged particle transport codes is to obtain solutions to the Boltzmann transport equation [11] using stochastic methods like Monte Carlo [12] or deterministic methods like S_N [13]. The Boltzmann transport equation is a balance equation for particles in a six-dimensional phase-space including space, angle, and energy. The solution to this equation describes the particle population and is referred to as the angular flux. For a given analog DCS model, the corresponding transport equation is referred to as the analog model and the angular flux is assumed to be exact. Analog, (detailed, step by step), simulation is feasible under strict circumstances (relatively low energies, thin targets, ...), but for high-energy electrons (above a few hundred keV), the number of interactions suffered by an electron along its trajectory is too large for detailed simulations [14]. For this reason, numerous computationally efficient approximate methods have emerged over the past 60 years. The most notable and prolific approximate method is Condensed History (CH). Berger describes CH as an artificially constructed random walk, each step of which takes into account the combined effects of many collisions [2]. The distances between collisions or the steps are significantly longer than those associated with the analog problem, making CH efficient. However, the theoretical basis and practical implementation of the CH algorithm introduces inherent and irreducible limitations that are unique to the method.

It is of interest to develop a method free of such limitations. To better understand benefits of such a method, the remaining sections provide a qualitative discussion of the literature relevant to the analog problem and the associated analog differential cross-sections (DCS), the Condensed History (CH) method, and Reduced Order Physics (ROP) models including the Moment-Preserving (MP) method. The analog problem is the point of departure for both CH and ROP models, so we begin with a discussion of the analog problem.

3.1. The Analog Problem

The analog description of transport can be mathematically expressed in terms of the linear Boltzmann or transport equation for the angular flux, where the interaction physics are represented through total cross sections (inverse mfp) and the DCSs for angular deflection and energy loss. The total cross sections and DCSs appear in the elastic and inelastic collision operators, which are integral operators or Boltzmann-type operators. Though electrons can undergo several different electromagnetic interactions, the dominant interactions are elastic collisions with nuclei and inelastic collisions with atomic electrons. Typical DCSs for elastic nuclear scattering include relativistic screened Rutherford, Wentzel, or the partial-wave expansion [15, 16, 17], while typical DCSs for inelastic electronic scattering include Rutherford, Moller, or the Evaluated Electron Data Library [18, 19]. These DCSs are highly peaked about small changes in direction and small energy losses and the associated total cross sections are very large resulting in extremely short mfps. Interaction physics of this nature present a difficult computational task.

Boundary conditions for the transport equation depend on the application, but typically include vacuum, pencil beams, or sources distributed in space, energy, and angle. However, mono-energetic pencil beams are very common in electron transport and further complicate the computational challenges because pencil beams are singular in space, energy, and angle.

The problem of computational inefficiencies associated with the analog physics was recognized immediately by early charged particle computational physicists. In fact, Berger [2] acknowledged that a direct analog Monte Carlo procedure would be quite costly, because of the enormous number of collisions that must be sampled. For example, it takes on the order of tens of thousands of collisions for an electron with energy of roughly 1-MeV to slow down to 1-keV, while only 20 to 30 Compton scatterings will reduce the energy of a photon from several MeV down to 1-keV or 18 elastic collisions in hydrogen will reduce a neutron from 2-MeV to thermal energies [2]. In 1963, only one calculation by direct analog Monte Carlo was reported [20]. Since then, several analog Monte Carlo electron transport codes have been developed [14, 21] and a few production codes have included analog physics options [22, 23, 24]. Solutions to the analog problem are exact for a given DCS; therefore, it is understandable that analog physics options were implemented, despite the fact that analog Monte Carlo is computationally inefficient. Moreover, it is feasible to use analog Monte Carlo for occasional calculations if significant computing resources are available. However, analog Monte Carlo remains impractical for routine calculations with exception of very restrictive problems like transport through optically thin materials. For this reason, approximate methods remain a critical component of most Monte Carlo electron transport codes.

3.2. Condensed History

Condensed history has been the prevailing approximate method in computational charged particle transport since the emergence of the field. The usual practice is to use "condensed" (class I) simulation methods, in which the global effect of multiple interactions is described by means of approximate multiple scattering theories. Alternatively, one can use "mixed" (class II) schemes in which hard (catastrophic) interactions, with energy loss or angular deflection above given thresholds, are simulated individually. For a given set of DCSs, class II schemes are intrinsically more accurate than class I simulations [14]. Some examples of codes containing class I schemes are ETRAN, ITS, MCNP, while examples of production codes containing class II CH schemes are Geant4, PENELOPE, and EGS4 [3, 24, 25]. Both class I and class II schemes utilize various results from multiple scattering theory, which is a subbranch of mathematical physics developed around the solution of the transport equation with limited applicability resulting from severe restrictions required to obtain analytical solutions [26, 27, 28, 29]. The analytical solutions or multiple scattering distributions describe the angular or energy distributions of electrons after traveling some distance s or a step, that are on the order of hundreds of analog mfps.

The major distinction between class I and class II schemes is how the grouping of collisions is handled. That is, class I schemes utilize precomputed multiple-scattering (MS) distributions

[30, 31, 32, 33] determined for fixed step-sizes on a fixed energy grid. For this reason, energy straggling is sampled from a MS distribution [32, 33] and secondaries are accounted for on an average basis. Therefore, it is not possible to distinguish between inelastic collisions resulting in secondary production (hard) and those that do not (soft). In contrast, a class II scheme like EGS allows all physical processes and boundaries to affect the choice of step size [34]. Thus, distance to hard collision is exponentially distributed, while secondary production is treated exactly by sampling energy-loss from the inelastic DCS above the secondary production threshold.

Regardless of the choice in the scheme, substantial efficiency gains over analog Monte Carlo can be realized with CH. However, the accuracy of early forms of CH was strongly dependent on step-size and while it was found that reducing the electron step-size causes the results to converge to the correct values, the computing time increases rapidly in proportion to the inverse of the step-size [35, 36, 37]. Therefore, special algorithms like PRESTA [38] were developed to select the optimal step-size during the process of a Monte Carlo simulation. Without an algorithm like PRESTA, one must resort to a tedious study to determine the optimal step-size such that acceptable accuracy and efficiency is achieved. However, this optimization may not be universal. The various production codes currently available differ in this optimization issue. Some codes, like ITS, have pre-determined step-size parameters, while codes like EGS utilize the PRESTA algorithm [38] or random hinging combined with lateral corrections found in PENELOPE. In addition to step-size limitations, condensed history suffers from inconsistent handling of the material and free surface boundaries. Material interfaces are a fundamental challenge for condensed history because the MS distributions are infinite medium solutions and are not valid for heterogeneous regions. Therefore, if a material interface is encountered, a special algorithm like the Jordan-Mack algorithm [39] or PRESTA is required. Another issue specific to class I schemes that utilize the Goudsmit-Saunderson distribution [30, 31] for sampling angular deflection is that the numerical methods required to generate the Goudsmit-Saunderson distribution are sensitive to small step-sizes. The backwards recurrence used to generate the Goudsmit-Saunderson is unstable for small steps. Even if the step-size is sufficiently long that the backwards recurrence is stable, it is possible that more than the pre-scribed number of recurrence coefficients are required to accurately resolve the Goudsmit-Saunderson distribution [40].

3.3. Reduced Order Physics Models

For the reasons stated above, various alternatives to the CH method were developed. Of particular interest are alternatives referred to as Reduced Order Physics (ROP) models, which are a family of transport-based approximations. ROP models include various approximate representations of the analog collision operators that are of both integral and differential forms. ROP models are obtained through some type of regularization procedure that removes reduce the nearly-singular behavior of the analog DCS, while systematically capturing the key physics through preservation of angular and energy-loss moments of the analog DCSs. Moreover, the zeroth or the total cross section is not preserved, rather it is determined self-consistently by the method. The resulting ROP model is then characterized by less peaked scattering with mfp's longer than the analog mfp. Efficiency is achieved by not preserving the total cross section, while accuracy is achieved by preserving the necessary number of moments beyond the zeroth.

There are numerous approximations that qualify as ROP models including Fokker-Planck, Boltzmann Fokker-Planck, Generalized Fokker-Planck, and Generalized Boltzmann Fokker-Planck. The remainder of this chapter is devoted to introducing each of these approximations and indicating how these methods contributed to the development of the MP method.

The classical Fokker-Planck operator is obtained by Taylor expanding the scattering kernels. This is a reasonable approach, assuming the angular flux is sufficiently smooth, because the DCSs fall off rapidly away from small deflection cosines and energy-losses. The resulting operator is differential in angle and energy and models elastic and inelastic scattering as diffusive processes. As a result, the Fokker-Planck operator does not capture large-angle scatter and can lead to energy gains. Pomraning confirmed these inconsistencies by showing that the Fokker-Planck operator is an asymptotic limit of the Boltzmann collision operator and only valid for unrealistically peaked scattering [41]. That is, the FP approximation is strictly valid in the limit that the total scattering cross section goes to infinity and the mean deflection cosine goes to unity such that the transport cross section remains bounded [42]. Under these conditions, large angle scattering is negligible and the FP operator is equivalent to the Boltzmann integral collision operator. Clearly, there is a limitation on the type of physics for which the classical FP operator is valid. Regardless, various implementations of Fokker-Planck operator were studied for in deterministic settings [43, 44, 45, 46].

In efforts to incorporate large-angle scattering, a kernel decomposition approach was introduced by Ligou and is referred to as the Boltzmann-Fokker-Planck (BFP) equation [47, 48, 49]. Ligou recognized that it is easier to numerically treat forward-peaked elastic scattering and small energy losses associated with such scattering using Fokker-Planck (FP) differential operators [45] rather than Boltzmann integral operators. However, the FP operator does not accurately capture large angle scattering. Therefore, it is necessary to decompose the scattering cross section into its singular and smooth components and apply the FP approximation to the singular component while leaving the smooth operator intact [50]. One important feature of the decomposition process is that there is no rigorous definition of the components so there are infinite decompositions. The key, as indicated by Landesman and Morel [50], is to select a decomposition that is not only accurate and efficient, but also easily integrated into existing transport codes. The early methods for solving the BFP equation were deterministic, but Morel and Sloan [51, 52] developed a hybrid multigroup/continuous-energy Monte Carlo method for solving the BFP equation or the MGBFP method. Morel described the MGBFP method as a new form of condensed history with the major distinction being that path lengths between collision sites are exponentially distributed.

In retrospect, application of kernel decomposition serves to stabilize the divergent behavior of the Fokker-Planck expansion [53] by effectively renormalizing the expansion coefficients. This renormalization process is central to the Generalized Fokker-Planck (GFP) method [54, 55] and resulted after attempting to generalize the FP operator to a broad class of physics with higher order FP operators [53]. In principle, the FP approximation can be improved by retaining higher order terms in the Taylor expansion of the collision operators. Thus, leading to a more accurate description of large angle scattering, but this is only true for specific kernels. For example, it is known that there are no valid FP operators for the Henyey-Greenstein kernel [41]

and that the standard FP operator is only marginally valid for screened Rutherford or screened Mott [42]. However, Pomraning [53] completed the same kernel analysis for the exponential and delta function and showed that higher order FP operators are valid for kernels such as these, but they are unphysical. In addition to characterizing the stability of higher order FP operators with respect to specific scattering kernels, this analysis revealed the explicit role of the analog DCS moments to developing approximations. That is, higher order FP expansions suggest that the accuracy of the approximation is improved by incorporating higher order moments. GFP approaches provide a means to stabilize higher-order FP operators through renormalization of the various terms that appear in the operator. The renormalization process, in essence, allows for an arbitrary ordered FP operator; hence, the approach referred to as generalized FP. Lastly, work on GFP showed that the key to a stable ROP model is preserving the integral form of the collision operator and retaining an arbitrary number of low order moments while approximating all of the higher order moments.

Insight gained from the foregoing approximations - FP, BFP, and GFP - combined with Lewis theory [56, 57] and practical experience from implementing and testing CH led to the development of the Generalized Boltzmann Fokker-Planck (GBFP) method [58]. Like the other ROP models, the GBFP method is a transport-based approximation. However, the GBFP method is more appropriate for Monte Carlo calculations like CH. The emphasis of GBFP method is the development of stable, moment-preserving representations of the collision operators. This is achieved by constructing ROP DCSs that are moment-preserving, per Lewis theory, while leaving the collision operators intact by simply replacing the analog DCSs with the ROP DCSs. Another key feature of the GBFP approach is that angular deflection and energy-loss interactions depend only on Legendre moments and energy-loss moments, not the detailed form of the analog DCSs. Therefore, the GBFP method is applicable to both continuous DCSs [59] and tabulated DCS data [60] and code modifications are not required for physics refinements because this is accomplished by providing moments of the desirable analog model through input data. The bulk of the work on the GBFP method to date emphasizes the most simple, but also the most effective ROP DCSs referred to as the discrete and hybrid models. The discrete model [61] is a superposition of discrete points and weights over the full range of the DCS, while the hybrid model [62] is a superposition of discrete points and weights over the peaked portion of the DCS and the tail is represented exactly by the analog DCS. Recently, the name Moment-Preserving method was adopted in place of the GBFP method to distinguish the method from Fokker-Planck and to emphasize the concept most fundamental to the method - moment preservation.

4. METHODS, ASSUMPTIONS, AND PROCEDURES

In this section, the Moment-Preserving method is presented along with a discussion of the analog DCSs and the analog transport model.

4.1. Analog Differential Cross-Sections and the Analog Transport Model

In the following sections, the analog physics are presented along with the analog transport model. The analog electron physics render application of the Monte Carlo method to analog transport model computationally inefficient. Specific features associated with the analog physics that attribute to the extreme computational cost are discussed. Herein, solutions to the analog transport model are referred to as the analog benchmark and accuracy and efficiency of the Moment-Preserving method are measured with respect to the analog benchmark. Therefore, the analog transport model is presented along with boundary conditions and applicable assumptions.

4.1.1. Elastic and Inelastic Analog Differential Cross-Sections

In this paper, we are concerned with the interactions that render analog Monte Carlo electron transport computationally inefficient. That is, elastic collisions with atomic nuclei (primary source of deflection) and inelastic collisions with atomic electrons (primary source of energy-loss). These interactions are characterized by highly peaked DCSs about small changes in direction and small energy transfers or energy losses resulting in extremely large total cross-sections or short mfps on the order of microns.

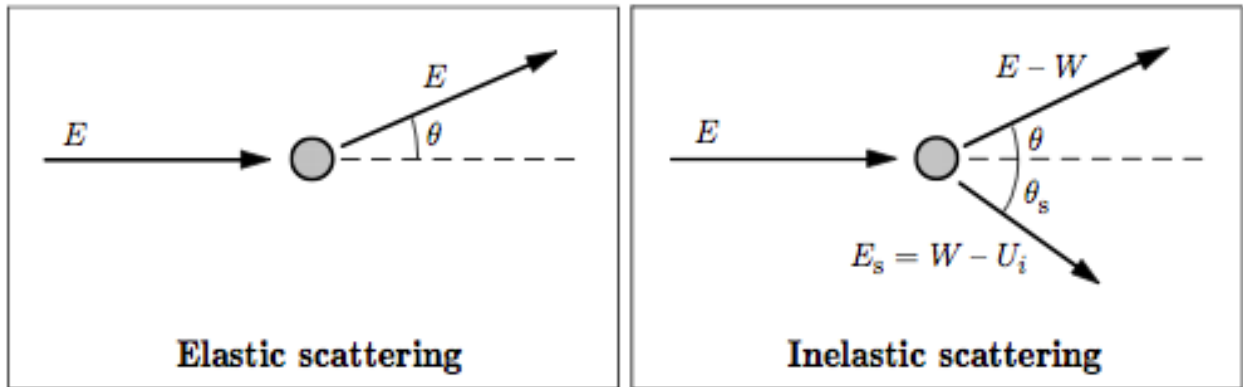


Figure 1: Electron interaction diagrams for elastic and inelastic scattering [24].

The analog DCSs used in this work are referred to as the partial-wave elastic DCS and the Moller inelastic DCS. However, the nature of electronic interactions is understood through simple forms of the elastic and inelastic DCSs such as screened Rutherford and the Rutherford energy-loss DCS. These DCSs describe Coulombic interactions between incident and target particles and are therefore dominated by distant collisions. As such, the DCSs are highly peaked and near-singular about forward directions and zero energy-losses resulting in extremely short collision mean free paths. For instance, nuclear scattering of high energy electrons is well described by the screened Rutherford DCS, or

$$\Sigma_{el}(E, \mu_0) = 2\pi r_e^2 Z^2 N \frac{1 - \beta^2}{\beta^4} \frac{1}{[1 + 2\eta - \mu_0]^2}, \quad (1)$$

where, aside from physical parameters, $\beta = v/c$, v being the speed of the ion and c the speed of light in vacuum, and η is the screening parameter typically in the range of 10^{-7} to 10^{-4} with smaller numbers corresponding to higher energies and lighter target nuclei. From this it follows that the total scattering cross section

$$\Sigma_{el}(E) \sim \frac{1}{\eta(E)} \gg 1, \quad (2)$$

demonstrating that the mean free path is very small, while

$$\frac{\Sigma_{el}(E, \mu_0 = 1)}{\Sigma_{el}(E, \mu_0 < 0.95)} \sim \frac{1}{\eta^2(E)} \gg 1, \quad (3)$$

Demonstrating that scattering is highly forward peaked. Thus, the picture of charged particle interactions is one of infinitely frequent collisions with infinitesimally small changes of state. Clearly then, except in rare cases of large angle scattering, a single collision is not representative of the transport process. Noticeable, indeed physically interesting, changes in the particle state occur on the average only after a large number of collisions. A more useful measure of the rate of change of the particle state is then provided by the momentum transfer or transport cross section defined by

$$\Sigma_{tr}(E) = 2\pi \int_{-1}^1 (1 - \mu_0) \Sigma_{el}(E, \mu_0) d\mu_0, \quad (4)$$

from which it readily follows that

$$\frac{\Sigma_{tr}(E)}{\Sigma_{el}(E)} \sim \eta(E) \ln \left[\frac{1}{\eta(E)} \right] \ll 1. \quad (5)$$

The physical significance of this result is that it is on the scale of a transport mean free path that an initially collimated angular distribution will have broadened considerably. Key to any approximate treatment of charged particle transport is then to recognize that it is not necessary to resolve the solution with respect to the true mean free path. More realistic cross sections such as the PW DCSs differ from the screened Rutherford cross section at larger scattering angles, but the singular behavior at forward scattering angles is given precisely by screened Rutherford. Likewise, proton and heavier ion scattering is described by the screened Rutherford DCS near forward scattering angles and all of the above considerations apply.

Inelastic energy losses are similarly singular about zero energy transfers. For instance, the energy-loss DCS for an ion colliding with a target electron is accurately described by the relativistic Rutherford cross section given by

$$\Sigma_{in}(E, Q) = 0.1536 \frac{Z_1^2 Z_2 \rho}{A_2} \frac{1}{\beta^2 Q^2} \left(1 - \beta^2 \frac{Q}{Q_{max}} \right), Q_{min} \leq Q \leq Q_{max}(\beta), \quad (6)$$

where Q is the single collision energy loss variable. We see from this that the total cross section is

$$\Sigma_{in}(E) = \int_{Q_{min}}^{Q_{max}} \Sigma_{in}(E, Q) dQ \sim \frac{1}{\beta^2 Q_{min}}, \quad (7)$$

while mean energy loss per unit pathlength travelled, or the stopping power, is given by

$$S(E) = \int_{Q_{min}}^{Q_{max}} Q \Sigma_{in}(E, Q) dQ \sim \frac{1}{\beta^2} \ln \left[\frac{Q_{max}(\beta)}{Q_{min}} \right]. \quad (8)$$

Thus, because $Q_{min} \ll Q_{max}$, we find for fixed β that $\Sigma_{in}(E) \gg S(E)$ and hence the mean energy loss per collision $\langle \Delta E \rangle \equiv \frac{S(E)}{\Sigma_{in}(E)} \ll 1$. As an example, for protons incident on tungsten, the total interaction cross section ranges from about $2 \times 10^3 \text{ cm}^{-1}$ at an energy of 2 GeV to about $8 \times 10^4 \text{ cm}^{-1}$ at 10 MeV, while the mean energy loss varies over the same energy range from $6 \times 10^{-3} \text{ MeV}$ to $2.5 \times 10^{-3} \text{ MeV}$. Given that the range of the proton is about 30 cm, the difficulty of resolving energy spectra or dose distributions using an analog description of the physics can be readily appreciated. Electron and positron inelastic electronic collisions are similarly described by DCSs that are singular about zero energy transfers, specifically given by Moller and Bhabha cross sections respectively for electrons and positrons.

That is to say, the physical interactions that dominate scattering and energy-loss of all charged particles are mediated by long range Coulomb forces which strongly weight small deflections and small energy-losses per collision. As a consequence, solving the analog problem by Monte Carlo or deterministic methods is completely impractical. Significant changes to the particle distribution function in space, angle, and energy can arise only from the cumulative effect of a large number of collisions and any approximate transport description must recognize and exploit this fact.

In this work, elastic and inelastic scattering are given by the partial-wave DCS and the Moller DCS respectively. The PW DCSs are numerically evaluated using the ELSEPA code [17] and are considered accurate representations of the elastic scattering of electrons by atomic nuclei at energies above roughly 1-keV. The PW DCSs utilized in this work are similar to those included in the ICRU-ELSEP database [63] with an exception being that the PW DCSs were evaluated on an energy grid with 16 logarithmically spaced points between 10-MeV and 20-MeV and 107 logarithmically spaced points between 1-keV and 10-MeV. A log-log linear interpolation scheme [64] was used to obtain both the total cross section and the DCS for a given energy between grid points.

The elastic collisions with nuclei considered herein deflect the incident electron through some scattering angle. While some energy is transferred to the nucleus during an elastic collision, the mass of the nucleus is so large in comparison to the electron mass that the energy transferred to the nucleus is assumed negligible. As mentioned, elastic scattering DCSs are extremely peaked about very small deflection angles and in some cases vary up to 28 orders of magnitude resulting

in extremely short mfps as small as fractions of a micron. This behavior is seen in **Figure 2** where PW DCSs are presented for aluminum and gold at various energies.

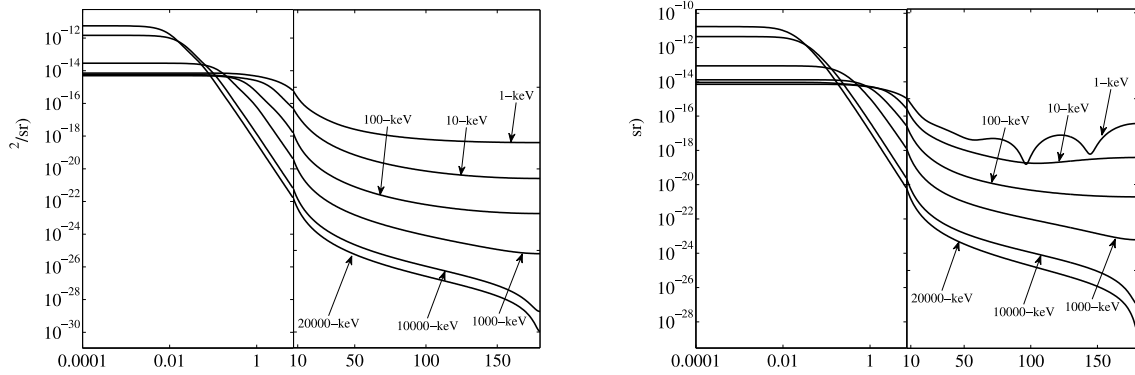


Figure 2: Partial-wave elastic differential cross-sections for various energy electrons scattering with aluminum (left) and gold (right) nuclei.

The Moller inelastic DCS [18] accounts for energy transferred to atomic electrons resulting in ionization or excitation of the target atom. In the Moller DCS, binding energies for the electrons shells are neglected; therefore, Moller is an approximation over all of the shells where the minimum energy transfer Q_{min} is assumed to be the mean ionization potential I_{MeV} [65]. The resulting inelastic DCS in which the incident electron with rest mass of and kinetic energy E transfers energy Q to the slower electron is given by

$$\Sigma_{in}(E, Q) = \frac{2\pi r_e^2 Z m_0 c^2}{\beta^2} \left[\frac{1}{Q^2} + \frac{1}{(E - Q)^2} + \frac{1}{(E + m_0 c^2)} - \frac{m_0 c^2 (2E + m_0 c^2)}{Q(E - Q)(E + m_0 c^2)} \right], \quad (9)$$

where $Q \in [Q_{min}, Q_{max}]$ and the upper bound is $Q_{max} = E/2$. Like the elastic scattering DCS, the inelastic DCS is peaked about small energy transfers or Q_{min} . The Moller DCS is not considered an accurate representation of inelastic collisions except for large energy transfers. In fact, the first moment of the Moller DCS, that is the stopping power, fails to reproduce the stopping powers given by the ICR Report 37 [66]. Here, we renormalize the Moller DCS such that the first moment is in agreement with the stopping powers in ICRU Report 37.

4.1.2. Analog Transport Model

Given a description of the electron interaction physics under consideration, we turn our attention to the corresponding transport equation. The linear Boltzmann equation for the angular flux of electrons $\psi(\vec{r}, E, \vec{\Omega})$ with position $\vec{r}(x, y, z)$, energy E , and direction $\vec{\Omega}$ is expressed by

$$\vec{\Omega} \cdot \nabla \psi(\vec{r}, E, \vec{\Omega}) = H^B \psi(\vec{r}, E, \vec{\Omega}), \quad (10)$$

where the Boltzmann collision operator is defined as

$$H^B\psi(\vec{r}, E, \vec{\Omega}) = \int_0^\infty dE' \int_{4\pi} d\Omega' [\Sigma_{el}(\vec{r}, E' \rightarrow E, \vec{\Omega}' \cdot \vec{\Omega}) + \Sigma_{in}(\vec{r}, E' \rightarrow E, \vec{\Omega}' \cdot \vec{\Omega})] \psi(\vec{r}, E', \vec{\Omega}') - \Sigma_t(\vec{r}, E)\psi(\vec{r}, E, \vec{\Omega}), \quad (11)$$

and the total interaction cross section is the sum of the elastic and inelastic total cross-sections, or $\Sigma_t(\vec{r}, E) = \Sigma_{el,0}(\vec{r}, E) + \Sigma_{in,0}(\vec{r}, E)$, which are denoted by the subscript zero. Eq. (10) is subject to the following boundary condition

$$\psi(\vec{r}, E, \varphi, \mu) = \psi^b(\vec{r}, E, \varphi, \mu), \quad \vec{r} \in \partial V, \quad \vec{\Omega} \cdot \vec{n} < 0, \quad 0 < E < \infty. \quad (12)$$

For electrons, elastic and inelastic scattering are treated separately as indicated in Eq. (11). Furthermore, it is assumed that elastic scattering occurs without energy loss and angular deflection from inelastic scattering is given by kinematics, so the collision operator can be expressed as

$$H^B\psi(\vec{r}, E, \vec{\Omega}) = H_{el}^B\psi(\vec{r}, E, \vec{\Omega}) + H_{in}^B\psi(\vec{r}, E, \vec{\Omega}), \quad (13)$$

where

$$H_{el}^B\psi(\vec{r}, E, \vec{\Omega}) = \int_{4\pi} d\Omega' \Sigma_{el}(\vec{r}, E, \vec{\Omega}' \cdot \vec{\Omega}) \psi(\vec{r}, E, \vec{\Omega}') - \Sigma_{el,0}(\vec{r}, E)\psi(\vec{r}, E, \vec{\Omega}), \quad (14)$$

and

$$H_{in}^B\psi(\vec{r}, E, \vec{\Omega}) = \int_0^\infty dE' \Sigma_{in}(\vec{r}, E' \rightarrow E) \delta[\vec{\Omega}' - f(E', Q)] \psi(\vec{r}, E', \vec{\Omega}') - \Sigma_{in,0}(\vec{r}, E)\psi(\vec{r}, E, \vec{\Omega}). \quad (15)$$

Here the angle of the primary is

$$f(E', Q) = \sqrt{\frac{E - Q}{E} \frac{E + 2m_0c^2}{E - Q + 2m_0c^2}}, \quad (16)$$

and the angle of the secondary is

$$f(E', Q) = \sqrt{\frac{E - Q}{E} \frac{E + 2m_0c^2}{E - Q + 2m_0c^2}}. \quad (17)$$

In the event that secondary production is neglected, deflection of the primary from inelastic scattering is also neglected and Eq. (15) reduces to

$$H_{in}^B \psi(\vec{r}, E, \vec{\Omega}) = \int_0^\infty dE' \Sigma_{in}(\vec{r}, E' \rightarrow E) \psi(\vec{r}, E', \vec{\Omega}) - \Sigma_{in,0}(\vec{r}, E) \psi(\vec{r}, E, \vec{\Omega}). \quad (18)$$

As previously mentioned, direct numerical solution of Eq. (10) is not realistic for most applications of interest because of the large total cross sections, $\Sigma_{el,0}$ and $\Sigma_{in,0}$, and DCSs, Σ_{el} and Σ_{in} , that are highly peaked about small deflections and energy losses. Because the computational effort is related to the number of collisions simulated per particle history and the outcome of the collision, simulation of Coulomb collisions are far more computationally intensive than the interactions characterizing neutral particles.

4.2. Moment-Preserving Method

In the MP method, a reduced order physics (ROP) transport equation is formed by replacing the analog DCSs in Eqs. (14) and (18) with ROP DCSs, . That is,

$$H_{el}^B \psi(\vec{r}, E, \vec{\Omega}) = \int_{4\pi} d\Omega' \hat{\Sigma}_{el}(\vec{r}, E, \vec{\Omega}' \cdot \vec{\Omega}) \psi(\vec{r}, E, \vec{\Omega}') - \hat{\Sigma}_{el,0}(\vec{r}, E) \psi(\vec{r}, E, \vec{\Omega}), \quad (19)$$

and

$$H_{in}^B \psi(\vec{r}, E, \vec{\Omega}) = \int_0^\infty dE' \hat{\Sigma}_{in}(\vec{r}, E' \rightarrow E) \psi(\vec{r}, E', \vec{\Omega}) - \hat{\Sigma}_{in,0}(\vec{r}, E) \psi(\vec{r}, E, \vec{\Omega}). \quad (20)$$

Although simply replacing the analog DCS with an ROP DCS may seem trivial or even arbitrary, there is no absence of rigor in this method. Particularly, much consideration is given to the form and properties of the ROP DCSs. The ROP DCSs are constructed such that they are smoother or less-peaked functions of deflection angle and energy loss and have significantly longer mfps than the analog DCSs. Thus, the ROP collision operators in Eqs. (11) and (12) have better properties than the analog collision operators, especially, from an efficiency standpoint.

Beyond efficiency, there are additional properties of the ROP collision operators that set this method apart from other approximate methods. For example, one of the unique characteristics of this method is that the integral form of the Boltzmann collision operators are maintained. Therefore, the description of the underlying transport mechanics is not lost, specifically, the correct Markovian feature of exponentially distributed collision sites [58]. Therefore, special algorithms for handling material and vacuum interfaces are not required. Moreover, exact treatment of collisions as Markov processes and less-peaked DCSs with longer mfps make it practical to simulate transport with a single-event method. Implementation of single-event methods is very straightforward compared to other methods like CH that is considerably more complicated. In fact, Monte Carlo codes with pre-existing single-event algorithms do not require any retrofitting when implementing the MP method, because this method treats electrons like neutral particles.

The MP method is efficient and implementation is straightforward, but there has been no mention of accuracy. This method must not only be competitive with, and potentially superior to CH with regard to efficiency and simplicity, but accuracy as well, and in many cases it is. Unlike CH, which introduces inherent and irreducible limits on accuracy as a result of the underlying theory, accuracy is systematically controllable. This is largely a result of the moment-preserving strategies that are central to this approach. The moment-preserving strategy is motivated by Lewis theory [56, 57], where Lewis proved that one can relate space-angle moments of the angular flux to momentum-transfer moments of the elastic scattering DCS. In addition, the eigenvalues of the elastic collision operator are directly dependent on the momentum-transfer moments. For these reasons, it is prudent to construct an ROP DCS that preserves moments of the analog DCS.

Given the relationship between the ROP DCS and the analog DCS moments, the following moment-preservation constraints are a natural choice when constructing an ROP DCS. If the analog elastic scattering moments are given by

$$\Sigma_{el,l}(E) = 2\pi \int_{-1}^1 d\mu P_l(\mu) \Sigma_{el}(E, \mu), \quad (21)$$

the moment preserving constraint is

$$\Sigma_{el,l}(E) = \hat{\Sigma}_{el,l}(E), l = 1, 2, \dots, L, \quad (22)$$

and the higher order moments are functions of the lower order moments

$$\hat{\Sigma}_{el,l}(E) = f(\Sigma_{el,1}, \Sigma_{el,2}, \dots, \Sigma_{el,L}), l > L. \quad (23)$$

For inelastic scattering the moments are given by

$$\Sigma_{in,j}(E) = \int_{Q_{min}}^{Q_{max}} dQ Q^j \Sigma_{in}(E, Q), \quad (24)$$

and the moment preserving constraint is similar and given by

$$\Sigma_{in,j}(E) = \hat{\Sigma}_{in,j}(E), j = 1, 2, \dots, J. \quad (25)$$

Again, the higher order moments are functions of the lower order moments

$$\hat{\Sigma}_{in,j}(E) = f(\Sigma_{in,1}, \Sigma_{in,2}, \dots, \Sigma_{in,L}), j > J. \quad (26)$$

By constructing an ROP DCS that preserves moments of the analog DCS, one can systematically control the accuracy of the ROP DCS models. That is, improvements in accuracy are achieved by simply preserving more moments of the analog DCS. In addition, the higher order moments

are functions of the exact lower order moments, so the higher order moments are good approximations rather than being neglected, as is the case for other ROP models like Fokker-Planck. The following sections present the two ROP DCS models that are used in this paper. Given the discrete ROP DCS model, we present a corresponding derivation of the ROP transport model for a discrete elastic and inelastic ROP DCS to emphasize the difference in the ROP transport model and the analog model. Lastly, the details of the ROP DCS construction process for each model are presented.

4.2.1. Reduced Order Physics Differential Cross-Sections

In this section, we present two forms of the elastic and inelastic ROP DCSs that are demonstrated herein: the discrete DCS and the hybrid DCS. The discrete DCS is a superposition of discrete points and weights. One of the benefits of the discrete DCS is the simple form of the DCS. The discrete DCS is simple to sample and requires significantly less memory requirements than DCS data because only a few points and weights are required for most problems of interest. The accuracy and efficiency of the discrete DCS are especially promising when calculating integral quantities like dose [58]. We define the discrete DCS for elastic scattering as

$$\hat{\Sigma}_{el}(\vec{r}, E, \mu_0) = \sum_{n=1}^N \frac{\alpha_n(E)}{2\pi} \delta[\mu_0 - \zeta_n], \quad (27)$$

and for inelastic scattering as

$$\hat{\Sigma}_{in}(\vec{r}, E, Q) = \sum_{n=1}^N \beta_n(E) \delta[Q - \gamma_n]. \quad (28)$$

The one drawback of the discrete DCS is the presence of discrete artifacts [61, 62], especially, if the discrete DCS is used when calculating differential quantities in thin slabs. However, discrete artifacts can be mitigated by use of the hybrid DCS, while still achieving efficiency gains. The hybrid DCS is a superposition of both discrete points and weights and a smooth function represented by an analog DCS. In previous work [61], the smooth component was represented by the SR DCS over $[-1, 1]$. The screening parameter was artificially selected such that the smooth component was less peaked near one. Moments of the smooth component are then subtracted from the analog DCS moments and this difference is then used to generate the discrete scattering angles. In this work, a slightly different representation was chosen where the tail is represented exactly by the analog model up to some cutoff point, μ_0^* . Beyond the cutoff point, or for $\mu_0 \in [\mu_0^*, 1]$, a discrete representation is used. The resulting hybrid DCS is

$$\hat{\Sigma}_{el}(\vec{r}, E, \mu_0) = \Sigma_e^S(E, \mu_0) + \sum_{n=1}^N \frac{\alpha_n(E)}{2\pi} \delta[\mu_0 - \zeta_n], \quad (29)$$

where $\Sigma_e^S(E, \mu_0)$ is an analog DCS for $\mu_0 \in [-1, \mu_0^*)$ and otherwise zero. The cutoff, μ_0^* , is typically chosen to be near the peak or unity to gain the benefit of the properties of the discrete DCS, while capturing the large-angle scattering exactly by the analog DCS. For inelastic scattering, the cutoff, Q , is selected near the peak, or near Q_{min} , for the aforementioned reasons.

From an implementation standpoint, there is little difference between the discrete and hybrid DCS. It requires the ability to sample hard collisions from the analog DCS and soft collisions from the discrete DCS. The only difference in generating the discrete DCS versus the hybrid DCS is that the moments are now defined over a partial interval corresponding to the peak.

Given the form of the ROP DCSs, a derivation of the ROP collision operators that comprise the ROP transport equation is presented.

4.2.2. Derivation of the Reduced Order Physics Collision Operators

The ROP DCS is constructed such that the singular contribution to inscatter and outscatter cancel (similar to the FP operator [45]). Ultimately, the purpose of constructing such a DCS is that the resulting ROP transport equation can be solved accurately and efficiently using single-scatter models. To be clear, a derivation of the elastic and inelastic ROP collision operators is presented. A derivation of both operators is presented because there is a subtle difference between the two that deserves some attention. For the sake of simplicity, the discrete DCS is used, but the same ideas carry over to any ROP DCS.

The starting point is the elastic collision operator. Substitution of Eq. (27) into Eq. (19) gives

$$H_{el}^B \psi(\vec{r}, E, \vec{\Omega}) = \int_{4\pi} d\Omega' \sum_{n=1}^{N+1} \frac{\alpha_n(E)}{2\pi} \delta[\mu_0 - \zeta_n] \psi(\vec{r}, E, \vec{\Omega}') - \left[\sum_{n=1}^{N+1} \alpha_n(E) \right] \psi(\vec{r}, E, \vec{\Omega}). \quad (30)$$

It is required that the discrete point $\zeta_{N+1} = 1$. Now, this point is intentionally separated from the remaining N points and weights in the inscatter and outscatter terms. That is,

$$\begin{aligned} H_{el}^B \psi(\vec{r}, E, \vec{\Omega}) &= \int_{4\pi} d\Omega' \sum_{n=1}^N \frac{\alpha_n(E)}{2\pi} \delta[\mu_0 - \zeta_n] \psi(\vec{r}, E, \vec{\Omega}') - \left[\sum_{n=1}^N \alpha_n(E) \right] \psi(\vec{r}, E, \vec{\Omega}) \\ &\quad + \int_{4\pi} d\Omega' \frac{\alpha_{N+1}(E)}{2\pi} \delta[\mu_0 - \zeta_N] \psi(\vec{r}, E, \vec{\Omega}') - \alpha_{N+1}(E) \psi(\vec{r}, E, \vec{\Omega}). \end{aligned} \quad (31)$$

If it can be shown that the last two terms in Eq. (31) indeed cancel, the resulting ROP transport equation will have an elastic scattering kernel that is significantly less peaked with reduced total cross section because α_{N+1} no longer contributes to the total cross section. It is not difficult to show that the last two terms cancel because $\mu_0 = \vec{\Omega}' \cdot \vec{\Omega} = 1$, if and only if $\vec{\Omega}' = \vec{\Omega}$ (see ref. [67] for details). Therefore, the following is true

$$\int_{4\pi} d\Omega' \frac{\alpha_{N+1}(E)}{2\pi} \delta[\mu_0 - 1] \psi(\vec{r}, E, \vec{\Omega}') = \int_{4\pi} d\Omega' \frac{\alpha_{N+1}(E)}{2\pi} \delta[\vec{\Omega}' \cdot \vec{\Omega} - 1] \psi(\vec{r}, E, \vec{\Omega}') \quad (32)$$

$$= \alpha_{N+1}(E) \psi(\vec{r}, E, \vec{\Omega}).$$

This term clearly cancels with the last term in Eq. (31). However, the same is not true for the inelastic collision operator, which is now shown.

The derivation of the inelastic ROP collision operator is easier to follow after a change of variables change variables from Q to $(E' - E)$. This gives

$$\hat{\Sigma}_{in}(\vec{r}, E, Q) = \sum_{n=1}^N \beta_n(E) \delta[(E' - E) - \gamma_n]. \quad (33)$$

Again, Eq. (33) is substituted into Eq. (20) and the argument of the delta function is rewritten as $E' - (E + \gamma_n)$ which gives

$$H_{in}^B \psi(\vec{r}, E, \vec{\Omega}) = \int_0^\infty dE' \sum_{n=1}^{N+1} \beta_n(E) \delta[E' - (E + \gamma_n)] \psi(\vec{r}, E', \vec{\Omega})$$

$$- \left[\sum_{n=1}^{N+1} \beta_n(E) \right] \psi(\vec{r}, E, \vec{\Omega}). \quad (34)$$

Now, the singular component or the $N + 1$ term is separated from the inscatter and the outscatter, the inelastic ROP collision operator becomes

$$H_{in}^B \psi(\vec{r}, E, \vec{\Omega}) = \int_0^\infty dE' \sum_{n=1}^N \beta_n(E) \delta[E' - (E + \gamma_n)] \psi(\vec{r}, E', \vec{\Omega})$$

$$- \left[\sum_{n=1}^N \beta_n(E) \right] \psi(\vec{r}, E, \vec{\Omega}) \quad (35)$$

$$+ \int_0^\infty dE' \beta_{N+1}(E) \delta[E' - (E + \gamma_{N+1})] \psi(\vec{r}, E', \vec{\Omega})$$

$$- \beta_{N+1}(E) \psi(\vec{r}, E, \vec{\Omega}).$$

Carrying out the integration over the $N + 1$ term results in the following singular contributions to inscatter and outscatter

$$\beta_{N+1}(E) \psi(\vec{r}, E + \gamma_{N+1}, \vec{\Omega}) - \beta_{N+1}(E) \psi(\vec{r}, E, \vec{\Omega}). \quad (36)$$

The terms in Eq. (36) do not cancel, unless $\gamma_{N+1} = 0$. Typically, the singular component of the inelastic DCS and the lower bound of the inscatter or energy-loss moments is chosen as the mean

ionization potential. Therefore, $\gamma_{N+1} = I_{MeV}$, where I_{MeV} is the mean ionization potential in MeV. So, if $\psi(\vec{r}, E + \gamma_{N+1}, \vec{\Omega})$ is expanded as a Taylor series about E, one can get a sense of the error introduced by choosing $\gamma_{N+1} = I_{MeV}$. That is,

$$\begin{aligned} & \beta_{N+1}(E)\psi(\vec{r}, E + \gamma_{N+1}, \vec{\Omega}) - \beta_{N+1}(E)\psi(\vec{r}, E, \vec{\Omega}) \\ &= \left[\sum_{j=1}^{\infty} \frac{\gamma_{N+1}^j}{j!} \frac{\partial^j}{\partial E^j} [\beta_{N+1}(E)\psi(\vec{r}, E, \vec{\Omega})] \right] + \beta_{N+1}(E)\psi(\vec{r}, E, \vec{\Omega}) - \beta_{N+1}(E)\psi(\vec{r}, E, \vec{\Omega}) \\ &= \sum_{j=1}^{\infty} \frac{\gamma_{N+1}^j}{j!} \frac{\partial^j}{\partial E^j} [\beta_{N+1}(E)\psi(\vec{r}, E, \vec{\Omega})] \end{aligned} \quad (37)$$

So, to first order, the error introduced by assuming that $\gamma_{N+1} = 0$ is proportional to I_{MeV} which is $\ll 1$. Therefore, this assumption introduces manageable error.

4.2.3. Generation of the Discrete and Hybrid Differential Cross-Sections

The procedure for constructing both the discrete and hybrid DCS from analog DCS moments is described. The form of the moment preservation constraints in Eqs. (22) and (25) is unstable to direct numerical inversion, so another approach similar to generation of Radau quadrature is taken [68]. Initially, attention is given to the discrete elastic DCS and then the discussion is extended to the discrete inelastic DCS and the hybrid DCS.

It is of interest to obtain a DCS that satisfies the moment constraint in Eq. (22). Given the discrete elastic DCS in Eq. (27), a system of equations for N points and weights (in total 2N unknowns) is formed. Substitution of Eq. (27) into the right-hand-side of Eq. (22) results in the following system of equations

$$\begin{aligned} \Sigma_{el,l}(E) &= \hat{\Sigma}_{el,l}(E) \\ &= 2\pi \int_{-1}^1 d\mu_0 P_l(\mu_0) \hat{\Sigma}_{el}(E, \mu_0) \\ &= \sum_{n=1}^N \alpha_n(E) \int_{-1}^1 d\mu_0 P_l(\mu_0) \delta[\mu_0 - \zeta_n] \\ &= \sum_{n=1}^N \alpha_n(E) P_l(\zeta_n) \end{aligned} \quad (38)$$

A total of $L = 2N$ equations are necessary because there are 2N unknowns. That is,

$$\begin{aligned} \Sigma_{el,1}(E) &= \alpha_1(E)P_1(\zeta_1) + \alpha_2(E)P_1(\zeta_2) + \cdots + \alpha_{2N}(E)P_1(\zeta_{2N}) \\ \Sigma_{el,2}(E) &= \alpha_1(E)P_2(\zeta_1) + \alpha_2(E)P_2(\zeta_2) + \cdots + \alpha_{2N}(E)P_2(\zeta_{2N}) \\ &\vdots \end{aligned} \quad (39)$$

$$\Sigma_{el,2N}(E) = \alpha_1(E)P_{2N}(\zeta_1) + \alpha_1(E)P_{2N}(\zeta_2) + \cdots + \alpha_{2N}(E)P_{2N}(\zeta_{2N})$$

The system formed in Eq. (39) emphasizes the requirement that α_n and ζ_n are obtained such that Legendre moments of the analog DCS are preserved. The system is then recast into one encountered when generating Gauss-Radau Quadrature for a non-classical weight function [69, 70]. That is,

$$\Sigma_{el,l} = \sum_{n=1}^N \alpha_n(E)P_l(\zeta_n) + \alpha_{N+1}(E)P_l(\zeta_{N+1} = 1), \quad (40)$$

which is a Gauss-Radau Quadrature system for a non-classical weight function, where in this case, the weight function is the analog DCS. Note that an additional unknown, $\alpha_{N+1}(E)$, is added in Eq. (40) and multiplied by $P_l(\zeta_{N+1} = 1)$. This is indicative of Radau quadrature and an expression for determining $\alpha_{N+1}(E)$ is given below. A Radau approach is selected rather than standard Gauss quadrature because Radau ensures that one point will correspond to the peaked component of the DCS (that is, $\zeta_{N+1} = 1$). Once the discrete points and weights are obtained, the peaked component is eliminated, thus, reducing the total cross section after renormalizing the discrete DCS. This is equivalent to satisfying the moment preservation constraints given in Eqs. (22) and (25).

To obtain the points and weights, coefficients of monic Legendre polynomials (α_j and β_j) are mapped to the coefficients of polynomials orthogonal to the analog DCS (a_j and b_j). The algorithm for this mapping is referred to as the modified Chebyshev algorithm (MCA) [70] and requires $2N+1$ moments of the analog DCS and $2N+2$ coefficients of monic Legendre polynomials. Given a successful mapping and the resulting coefficients, a_j and b_j , the Golub and Welsch algorithm [71] is used to obtain the eigenvalues of the Jacobi matrix. The Jacobi matrix is a tridiagonal matrix where the diagonal is set to a_j and the off-diagonals are set to $\sqrt{b_j}$. The eigenvalues of the Jacobi matrix are the points and the first entry of each corresponding eigenvector squared are the weights. That is, $\zeta_n = \lambda_n(J)$ and $\alpha_n = (V_{n,1})^2$, where V is a eigenvector matrix. The application of the Golub and Welsch algorithm to the aforementioned Jacobi matrix will result in Gauss Quadrature and must be modified according to Golub [69] for Radau quadrature. Therefore, the Jacobi matrix is modified such that

$$J_{N+1} = \begin{bmatrix} J_N & b_N \vec{e}_N \\ b_N \vec{e}_N^T & a_{N+1} \end{bmatrix}, \quad (41)$$

where

$$\alpha_{N+1} = 1 - b_N \frac{p_{N-1}(1)}{p_N(1)}. \quad (42)$$

Application of the Golub and Welsch algorithm to Eq. (41) will result in $N + 1$ points and $N + 1$ weights normalized to unity. To obtain the final discrete DCS, the $N + 1$ point and weight is eliminated and the remaining weights are then scaled by the analog total cross section or $\Sigma_{el,0}$. The total cross section for the discrete DCS is then

$$\hat{\Sigma}_{el,0} = \sum_{n=1}^N \alpha_n(E) \quad (43)$$

which does not include the $N + 1$ weight. The total cross section in Eq. (43) is significantly reduced depending on the order of the discrete DCS, the particle energy, and the target material, thus, extending the mfp. This completes the process of generating a discrete elastic DCS.

The process of generating a discrete inelastic DCS is similar. To use the same quadrature tools, the inelastic DCS must be mapped to an elastic DCS because the bounds on the elastic DCS are ideal for these tools (that is, $[-1, 1]$). Given a mapping, the moments of the inelastic DCS are related to Legendre moments of an ROP elastic DCS. Points on $(-1, 1]$ are generated with corresponding weights and then mapped back to $(0, Q_{max}]$. The mapping is

$$Q(\mu) = \frac{Q_{max}}{2} (1 - \mu), \quad (44)$$

and the resulting relationship between the moments is

$$\tilde{\Sigma}_{el,l} = \sum_{j=0}^l c_j^l \frac{(-1)^j}{j!} \left(\frac{2}{Q_{max}} \right)^j \Sigma_{in,j}, \quad (45)$$

where

$$c_j^l = \frac{1}{2^j j!} \prod_{i=0}^{j-1} [l(l-1) - i(i-1)]. \quad (46)$$

This summarizes the process of generating the discrete elastic and inelastic DCS. Many of the same ideas carry over to generation of the discrete component of the hybrid DCS.

To generate the discrete points and weights for the hybrid DCS a cutoff value is selected. It should be selected such that additional accuracy is gained while still maintaining efficiency. That said, selection of the cutoff is problem dependent and mostly a heuristic exercise.

Given a cutoff, the following moments are used to generate the discrete points and weights

$$\Sigma_{el,l}^D = 2\pi \int_{\mu_0^*}^1 d\mu P_l(\mu) \Sigma_{el}(\mu). \quad (47)$$

and

$$\Sigma_{in,j}^D = \int_{Q_{min}}^{Q^*} dQ Q^j \Sigma_{in}(Q). \quad (48)$$

In both cases, to use the DCS generation tools, the moments must be mapped to the appropriate domain $[-1, 1]$ just as for the discrete inelastic DCS. For the inelastic hybrid DCS the mapping does not change significantly from Eqs. (44) and (45) and is

$$Q(\mu) = \frac{Q^*}{2} (1 - \mu), \quad (49)$$

where μ is on $[-1, 1]$ and Q is on $[0, Q_{cut}]$. Given this mapping, the moments are related by

$$\tilde{\Sigma}_{el,l} = \sum_{j=0}^l c_j^l \frac{(-1)^j}{j!} \left(\frac{2}{Q^* - Q_{min}} \right)^j \sum_{k=0}^j \binom{j}{k} (-Q_{min})^{j-k} \Sigma_{in,k}^D, \quad (50)$$

where c_j^l is given by Eq. (46).

The map for the hybrid elastic DCS is given by

$$\mu'(\mu) = \frac{\mu_0^* - 1}{2} (1 - \mu) + 1, \quad (51)$$

where μ is on $[-1, 1]$ and μ' is on $[\mu_0^*, 1]$. Given this mapping, the moments are related by

$$\tilde{\Sigma}_{el,l} = \sum_{j=0}^l c_j^l \frac{(-1)^j}{j!} \left(\frac{2}{1 - \mu_0^*} \right)^j \sum_{k=0}^j b_k^j \Sigma_{el,k}^D, \quad (52)$$

where b_k^j

$$b_k^j = \int_{-1}^1 d\mu P_k(\mu) (1 - \mu)^j = \sum_{m=0}^k c_m^k \frac{(-1)^m}{m!} \frac{2^{j+m+1}}{j + m + 1}, \quad (53)$$

and the coefficient c_m^k is given in Eq. (46).

4.3. Development of the Geant4 Toolkit Moment-Preserving Method Classes

Reduced order physics DCS models are central to the Moment-Preserving method and therefore, the majority of the development effort is in generating, storing, and accessing the ROP DCSs. Geant4 considers all physical interactions as processes, requiring implementation of the G4VEmProcess class, and the details of each process is captured by the model. This is accomplished through implementation of the G4VEmModel class, which is the primary source of development for the MP method (assuming the ROP DCS are available in the form of a DCS data library). The reason that the majority of the development occurs when implementing the G4VEmModel class is because it is at this level where the ROP DCSs are stored in Geant4 data classes, and also it is at this level where the ROP DCSs are accessed.

It should be noted that if one were to use the total number of lines of code required to implement an electron transport algorithm as a metric for quantifying development and maintenance effort, the effort associated with MP method is about ten times less than the effort required by the Geant4 default multiple-scattering model used to transport electrons. That is, the G4UrbanMscModel requires roughly 2000 lines of code, while the comparable MP elastic model, G4DiscreteElasticModel, only requires 300 lines of code.

The remaining sections provide detail on the associated physics process and model classes, the cross-section construction classes, and the cross-section library and data processing tools.

4.3.1. Physics Processes

Physics processes for discrete and hybrid DCSs were implemented and include: G4DiscreteElasticProcess, G4HybridSoftElasticProcess, G4HybridHardElasticProcess, G4DiscreteInelasticProcess, G4HybridSoftInelasticProcess, and G4HybridHardInelasticProcess. The physics process is relatively simple because use is made of many of the virtual methods in G4VEmProcess. The only methods that required implementation include a method to initialize the process class (this consists of constructing the associated physics model and setting a few data members) and a method that determines the applicable particles.

4.3.2. Physics Models

Physics models for discrete and hybrid DCSs were implemented and include: G4DiscreteElasticModel, G4HybridSoftElasticModel, G4HybridHardElasticModel, G4DiscreteInelasticModel, G4HybridSoftInelasticModel, and G4HybridHardInelasticModel. Three important methods are included in the physics model class: an initialization method where the cross-section data is read in; a method for obtaining the total cross-section; and a method for sampling the DCS. Use of the ROP DCS data reduces runtime and pre-existing Geant4 data tools were utilized that reduced development overhead and eased integration of the models into the toolkit. The code required to utilize the Geant4 data classes is left to section 6.3, which describes the use of the Geant4 data classes in greater detail.

There are two methods remaining for the physics model discussion, a method for obtaining the ROP total cross-section and a method for sampling the ROP DCS. Obtaining the total cross-section is trivial and requires a table look-up as a function of energy (some minor modifications to the Geant4 data classes were required). The method for sampling the DCS requires two steps. First, the energy index of the data is determined using the previously discussed binary search; however, the linear interpolation is accomplished through random sampling using the weights from a linear interpolation on log-log scale [64]. Given an ROP DCS evaluated at some energy grid point, the scattering angle is determined through inverting a discrete CDF, which is a very simple process.

At this point, no mention was made of the hybrid cross-section. As seen in the list of models, the hybrid cross-section is composed of two models: one for soft collisions and one for hard collisions. The soft collisions are given by the discrete cross section and all of the previous discussion carries over. The hard collisions are given by the analog DCS. For the partial-wave elastic DCS much of the previous discussion also carries over. However, for the Moller inelastic DCS, an analytical expression is used to obtain the total cross-section and a rejection technique is used to sample the DCS.

4.3.3. Cross-Section Library and Data Processing

A ROP cross-section library was generated for the partial-wave and Moller DCS for 1, 2, 4, and 8 points and weights. The libraries are formatted such that the Geant4 data classes could be used. For each material and number of points and weights, there are two data files: one for the total cross-section and one for the CDF. The files are named accordingly. For example, for a 2-angle discrete DCS based on the partial-wave DCS for aluminum the two files are named `gbfp_pwe_tcs_13_2.dat` and `gbfp_pwe_cdf_13_2.dat`, where the first number is the atomic number and the second number is the number of points and weights.

There are two primary Geant4 data classes utilized in processing and storing the ROP DCS data: `G4ElementData` and `G4PhysicsVector`. `G4ElementData` is a very powerful class that stores data for a particular element and then only requires the atomic number to retrieve the data. Upon construction, the `G4ElementData` object requires the atomic number and the data in the form of a pointer to a `G4PhysicsVector` object, so the `G4ElementData` class is really a container of `G4PhysicsVector` objects. The data is stored in the `G4PhysicsVector` object, which is also a very powerful class because as long as the data is properly formatted, one must simply pass the `G4PhysicsVector` object a stream of the data.

Given a brief description of the implementation of the MP method within the Geant4 toolkit, we now present results.

5. RESULTS AND DISCUSSION

In this section, a wide array of results that capture the key features of the Moment-Preserving (MP) method is presented. In particular, the key features of this method demonstrated are: systematic accuracy, efficient, mathematically robust, versatile and simple.

The results section begins by demonstrating the first feature of the MP method through calculation of highly differential quantities like angular distributions and energy spectra. In these calculations, the MP method is tested under the strictest possible conditions (that is, high-energy mono-energetic pencil beams normally incident on thin slabs). Under these conditions, analog or single-scatter models are typically required. However, it is shown that both transmitted and reflected angular distributions and energy-loss spectra can be resolved through use of the hybrid DCS. Though the emphasis of this section is the demonstration of the systematic nature of the MP method, efficiency gains of at least five times analog efficiencies were demonstrated while maintaining analog level accuracy in very thin slabs. Under these extreme conditions where the hybrid model is successful, the discrete model tends to result in artifacts. However, it is possible to utilize the discrete model in thicker slabs where the benefit of efficiency gains is significantly improved. Following the angular distribution and energy spectrum results, longitudinal and lateral distributions are presented where the first two features of the method are again demonstrated on this different, but important quantity.

Given a clear understanding of the systematic feature of this method, results for less extreme problem conditions are presented to show that for more practical applications the MP method is not just accurate, but also very efficient. That is, we show that for 1-D and 2-D dose calculations the MP method achieves analog level accuracy while improving efficiency up to three orders of magnitude over analog efficiencies. We show that this is true for low-Z and high-Z materials, for molecules like water or bone, and multi-region problems. Furthermore, it is shown that material interfaces in multi-region problems do not introduce additional error at interfaces as does the condensed history method. This is because the MP method is a transport- based approximation and the benefit of this type of approach is that no additional algorithm is required to handle material interfaces.

Prior to this work, no effort had been made to validate the MP method through comparison with experimental benchmarks. Therefore, several results are presented in efforts to begin this validation process. Specifically, results from the MP method are compared to the experimentally determined energy deposition profiles (that is, the Lockwood data [72]). Similar calculations are made with the Geant4 default electromagnetic physics option 3, so that accuracy and efficiencies for the MP method can be compared to the Geant4 physics. In addition, we compare charge deposition results generated using MP method with experimentally determined charge depositions (that is, the Tabata data [73]). A key concept to point out in comparing with experimental results is that if an analog model exists that is in acceptable agreement with an experimental benchmark and moments of this analog model are readily available, one can generate reduced order physics DCSs based on the aforementioned analog model and show similar levels of agreement while significantly improving efficient. In this sense, the versatility and simplicity of the method is demonstrated. That is, to improve agreement through use of a

different analog model algorithmic changes are not required; one must simply obtain moments of some preferable analog model, generate an ROP DCS library for this analog model, and run the calculation.

Finally, for completeness the MP method is applied to a space weather application to show that this method is not just effective for theoretical calculations. In particular, the total response function is generated for the CEASE detector telescope using an analog model, a discrete model, and the default Geant4 electromagnetic physics with option 3.

In all comparisons, the analog benchmark is obtained by using an analog elastic DCS and an analog inelastic DCS (with exception of the validation section). The analog benchmark is numerical rather than experimental, so to some degree it is idealized. This type of benchmarking is required to illustrate how accuracy is achieved through preservation of the analog DCS moments. In the following sections, accuracy and efficiency is measured with respect to the analog benchmark.

5.1. Angular Distributions and Energy Spectra

In this section, the accuracy of the MP method is tested under conditions that are often times impractical to simulate without the use of an analog model. That is, the transport of a mono-energetic pencil beam of electrons with energies above several hundred keV in thin slabs. Of particular interest is the calculation of reflected and transmitted angular distributions and energy spectra in slabs with varying thicknesses down to 100 analog elastic mfps (~ 1 to $100\ \mu\text{m}$). It is shown that under these conditions the MP method is effective at resolving angular distributions and energy spectra through the use of suitable reduced order physics (ROP) DCSs. Under these extreme conditions, a hybrid DCS is, in most cases, required to resolve these distributions. While it is possible to resolve highly peaked distributions with analog level accuracy using the MP method, this is typically accompanied by losses in efficiency. Nonetheless, the ability to systematically control accuracy such that one can predict angular distributions and energy spectra for highly-peaked scattering in thin slabs is a strong feature of this method.

While it is true that one cannot expect to realize significant efficiency gains with analog level accuracy under the aforementioned conditions, in more realistic settings (that is, thicker regions) it is possible to relax the ROP models such that both analog level accuracy and significant efficiency gains are achieved. Relaxation of the ROP models is possible in thicker slabs because the initial pencil beam experiences more spreading in space, angle, and energy in thicker slabs. This is simply an effect of the number of collisions sustained by an electron while traversing a medium. In thicker slabs, electrons suffer more collisions; thus, causing additional spreading of the initial state of the beam. With additional spreading of the beam, less information in the form of analog DCS moments is required to resolve angular distributions and energy spectra. Therefore, the ROP DCS can be relaxed or models preserving fewer moments can be utilized.

In the following two sections, the impact of the size of the slab on the accuracy of the MP method is demonstrated. Both discrete and hybrid models are tested for angular distribution and energy spectrum calculations in low-Z and high-Z slabs with varying thicknesses. The thickness

of the slab is measured with respect to the analog elastic mfp corresponding to the source particle energy and the target material. Results for slabs with thicknesses of 100, 300, 1000, and 3000 analog elastic mfps are presented (in the remaining discussion mfp implies analog elastic mfp). In **Figure 3**, problem setup is described.

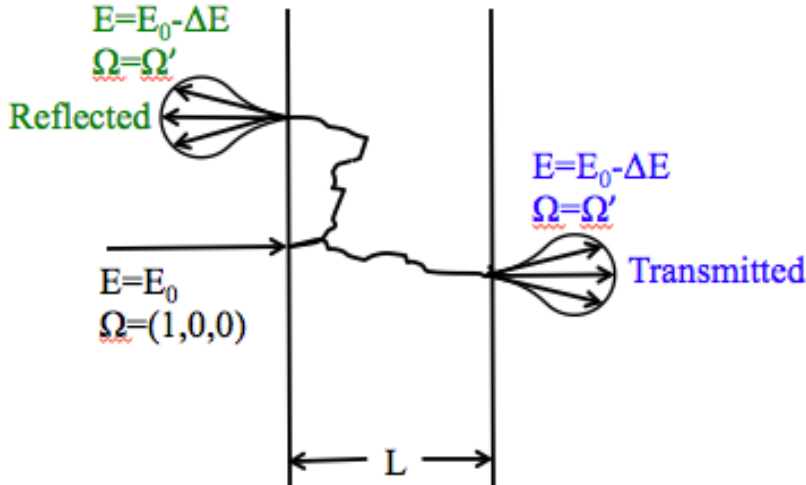


Figure 3: Thin slab problem setup.

5.1.1. Angular Distributions

Reflected and transmitted angular distributions are presented below for one-dimensional slabs composed of aluminum or gold with thicknesses of 100, 300, 1000, and 3000 mfps. The source is positioned at $x = 0$ with a direction of $\Omega = (1, 0, 0)$. A total of $4E+07$ source particles are simulated when calculating the angular distributions. The analog benchmark is a solution to the aforementioned problem using analog Monte Carlo, where elastic scattering is given by the partial-wave DCS and inelastic scattering is given by the Moller DCS. Uncertainties associated with these results are within 1% in most bins, such that one can state conclusively that good agreement exists between the ROP models and the analog benchmark.

First, the most challenging problem is presented. That is, calculation of transmitted angular distributions for 10000-keV electrons incident on an aluminum or gold slab 100 mfps thick. In **Figure 4**, transmitted angular distributions in aluminum and gold computed using the discrete and hybrid DCSs are compared to the analog benchmark. There are a few features to note in **Figure 4**. The peakedness of this distribution is extreme and varies about three orders of magnitude over only 10 degrees. This level of peakedness is difficult to resolve with a discrete elastic DCS and results in the discrete artifacts seen clearly in **Figure 4**. The difficulty in resolving highly peaked distributions using the discrete DCS results from the form of the DCS. That is, electrons can only scatter through N discrete angles determined by the order of the DCS. Therefore, the N discrete angles are favored in the angular distribution because in thin slabs

electrons do not suffer enough collisions such that various combinations of scattering events smooth out the artifacts. However, through use of the hybrid model the discrete artifacts are mitigated and the only noticeable differences in the hybrid model solution and the analog benchmark are in the tail where the differences in the solutions are statistically insignificant. In **Figure 4**, the impact of target atomic number is shown, where for increasing Z the distribution is less peaked. However, the impact of the atomic number on the peakedness of the scattering is not significant enough to dramatically improve the discrete results in thin slabs for 10000-keV electrons.

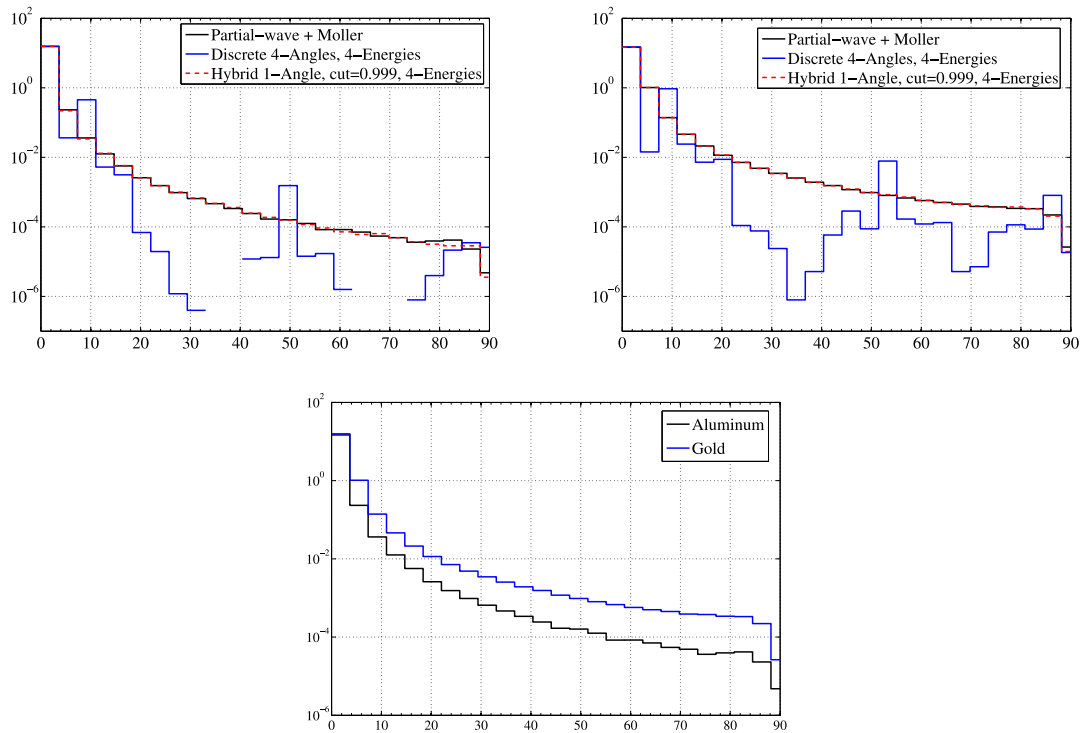


Figure 4: Transmitted angular distributions for 10000-keV electrons on aluminum and gold.

Even in aluminum slabs with thicknesses of 3000 mfps for 10000-keV electrons, the discrete DCS results in artifacts as seen in **Figure 5**. This is an indication of the extreme peakedness of the scattering at higher energies and in this regime a hybrid DCS is required to resolve the transmitted angular distribution unless additional angles are used. However, it is clear by **Figure 5** that in thicker slabs where particles undergo thousands of collisions that the discrete artifacts are greatly reduced. Furthermore, the impact of the atomic number is seen in **Figure 5**, where the discrete artifacts are less pronounced in the gold slab because scattering of electrons by high- Z

materials is less peaked. Nonetheless, it is always possible to utilize a hybrid model to resolve angular distributions overwhelmed by discrete artifacts.

In thicker slabs, it is possible to relax the cutoff to $\mu^* = 0.99$ for the hybrid model improving the efficiency of the calculation while remaining accurate. The results in **Figure 4** and **Figure 5** indicate that it is possible to resolve angular distributions in highly-peaked scattering regimes by systematically increasing the accuracy of the ROP DCS through preservation of additional moments. Of course, increasing accuracy will reduce the efficiency of the calculation, but under these conditions (highly-peaked scattering in thin slabs) analog Monte Carlo efficiencies are typically manageable, so efficiency gains of two to five times faster than analog Monte Carlo is considered a significant improvement. As was pointed out, the emphasis of this section was not to necessarily demonstrate orders of magnitude efficiency gains, but rather to show that the ROP models limit to analog level accuracy even under extreme conditions. That said, it is of interest to maximize efficiency gains whenever possible. Therefore, the following results provide a sense of the accuracies associated with a less-extreme scattering regime. Efficiency results are presented later in section 5.1.3 and indicate that it is possible to resolve angular distributions efficiently (up to two orders of magnitude more efficient than analog) and accurately, especially, in less-extreme scattering regimes.

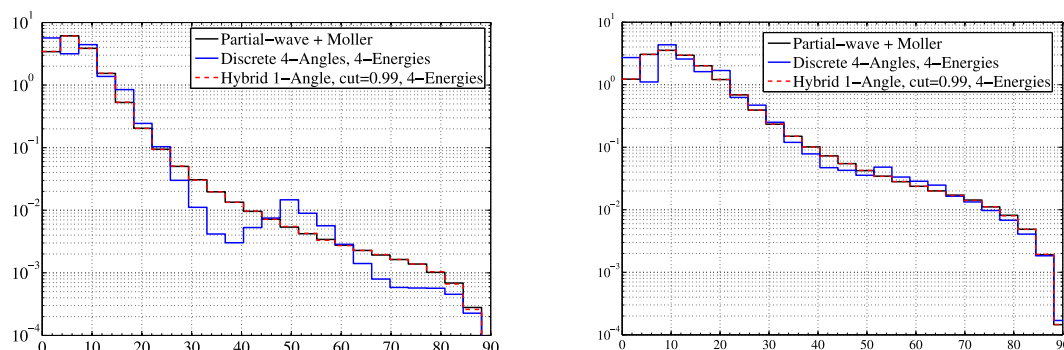


Figure 5: Transmitted angular distributions for 1000-keV electrons on aluminum and gold.

The following figures present transmitted angular distributions in a less-peaked scattering regime. That is, 1000-keV electrons incident on gold slabs with varying thicknesses. As noted, the peakedness of the scattering is a function of particle energy and the target atomic number. With decreased particle energy and increased atomic number, the peakedness is reduced. Nonetheless, even for 1000-keV electrons on gold the problem is still extremely anisotropic with respect to neutral particle scattering. In **Figure 6**, the impact of slab thickness and in turn, the effectiveness of the discrete model is demonstrated. In **Figure 6** discrete artifacts are present for slabs 100 and 300 mfps thick, but the hybrid model is in good agreement in these cases. However, in **Figure 6**, discrete models with at most 4-angles are sufficient when resolving the transmitted angular distribution. In fact, in **Figure 6** the discrete artifacts resulting from a single-angle discrete model are almost negligible and though there is not perfect agreement the general behavior of the transmitted angular distribution is captured.

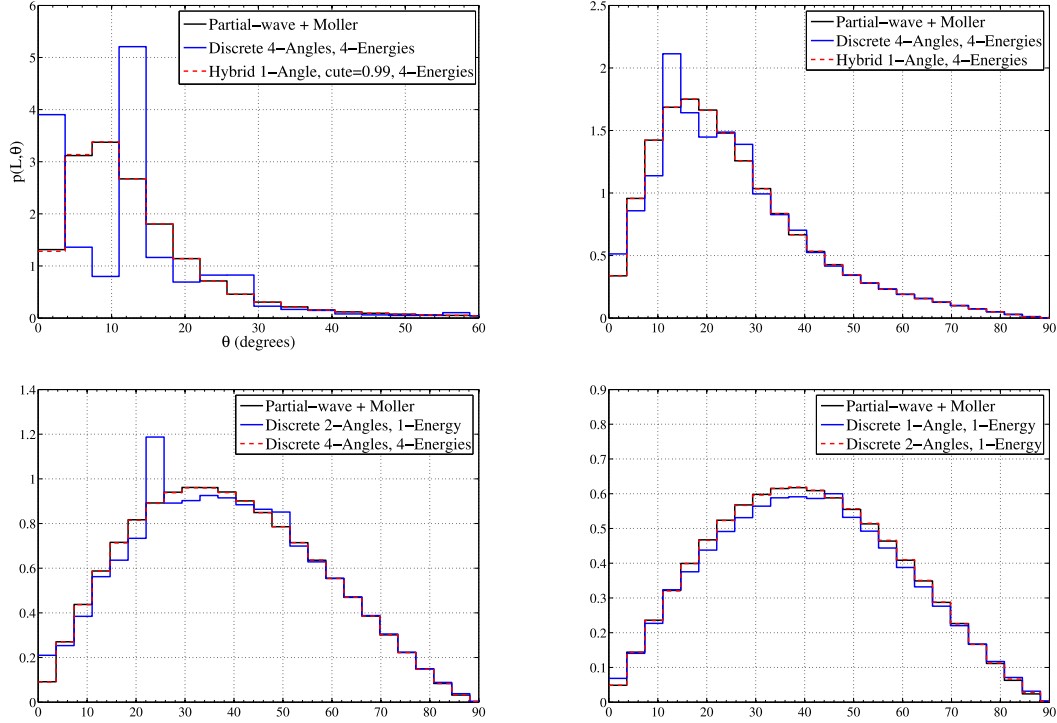


Figure 6: Impact of slab thickness on transmitted angular distributions on 1000-keV electrons on gold.

We now present reflected angular distributions for 1000-keV and 10000-keV electrons on aluminum or gold slabs with thicknesses of 100, 300, 1000, and 3000 mfps. In **Figure 7** reflected angular distributions for 10000-keV electrons on gold are presented. First, note the distributions in **Figure 7** are significantly reduced in magnitude relative to the transmitted angular distributions for 10000-keV electrons. For highly-peaked scattering, a very small fraction of particles are reflected. Slab thickness has a similar impact on reflected distributions as for transmitted distributions. That is, with increasing slab thickness electrons suffer more collisions before being reflected, spreading the distributions in angle. In general, the discrete model tends to have the correct behavior; however, the distribution is roughly two to five times greater in magnitude. Once again, the hybrid model can be used in all cases. The disagreement between the analog benchmark and the hybrid models is statistical because very few particles are reflected.

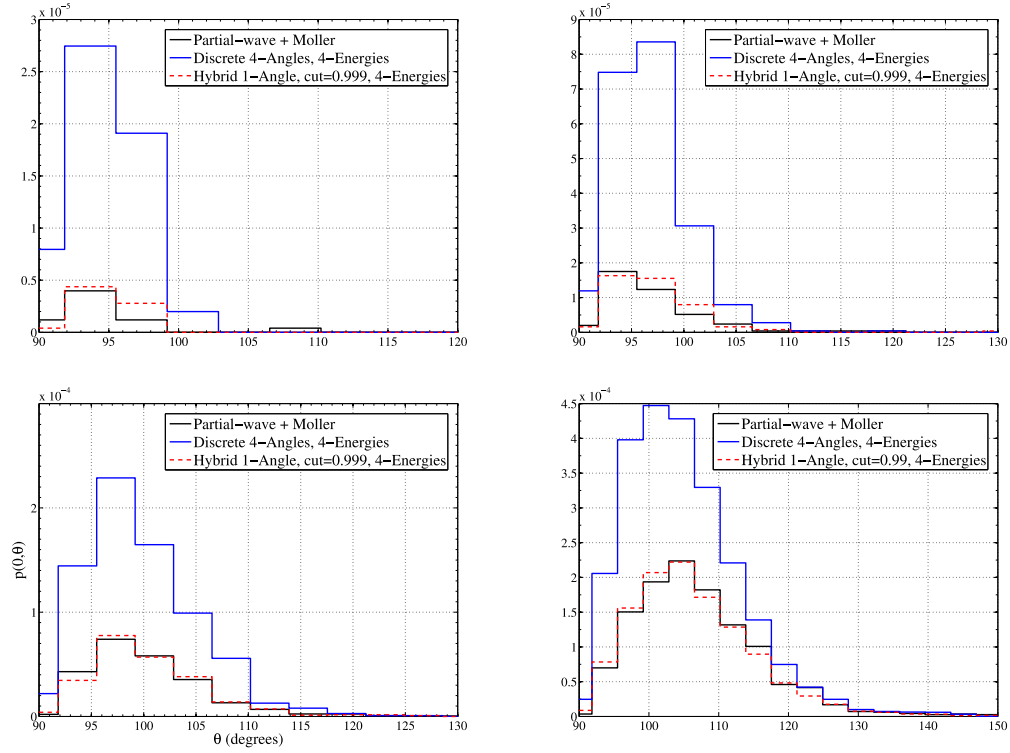


Figure 7: Impact of slab thickness on reflected angular distributions for 10000-keV electrons on aluminum.

In **Figure 8** angular distributions for 1000-keV electrons incident on gold slabs with thicknesses of 100, 300, 1000, and 3000 mfps are presented. For lower energies in high-Z materials the scattering is less peaked and the ROP model can be relaxed under these conditions. Specifically, reflected angular distributions generated using the discrete model are not overwhelmed by artifacts as seen in **Figure 8**. For slabs of sufficient thickness, a hybrid model is not required and the more efficient discrete model can be utilized. For slabs that are 3000 mfps thick (**Figure 8**), a single-angle, single-energy discrete model provides noteworthy agreement.

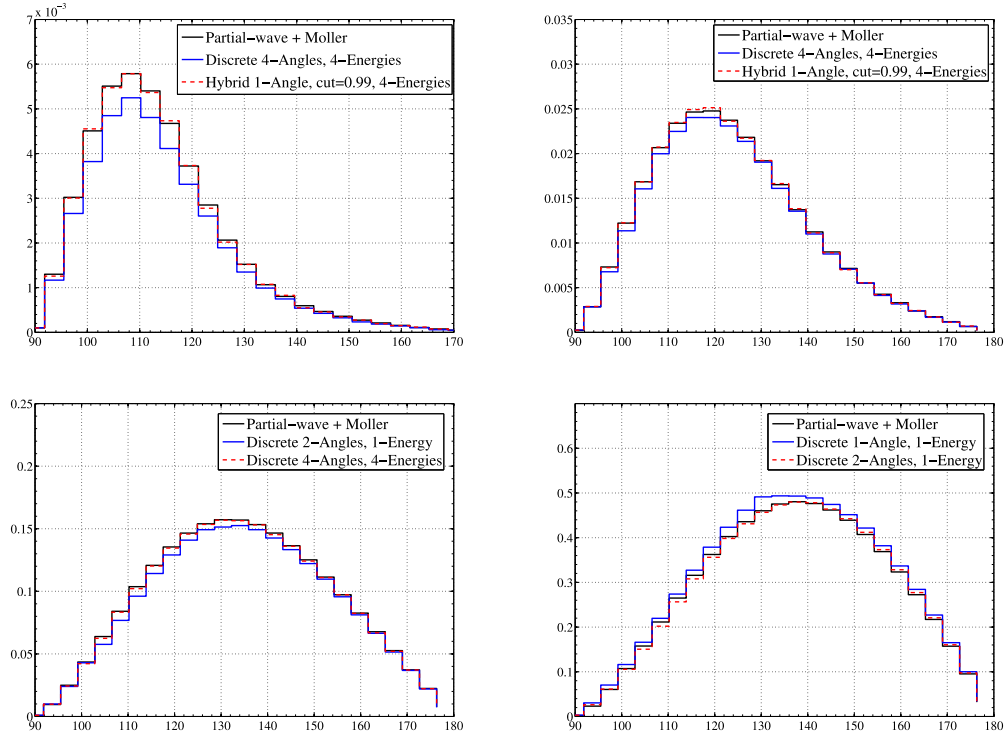


Figure 8: Impact of slab thickness on reflected angular distributions for 1000-keV electrons on gold.

5.1.2. Energy Spectra

Next, reflected and transmitted energy spectra are examined. The simulation characteristics, including slab thickness, material types, and the number of source particles, are the same as described in the previous section. Discrete inelastic DCS models are not presented because a sufficient number of inelastic collisions do not occur in thin slabs overwhelming the spectra with discrete artifacts. Therefore, the focus is on two different hybrid inelastic DCS models. The hybrid models include DCSs with $Q^* = 10$ -keV and one or two discrete energies. In each of the following results, elastic scattering is modeled by a discrete four-angle DCS. Again, the most challenging problem, 10000-keV electrons on aluminum slabs, is considered first. In **Figure 9**, transmitted energy-loss spectra are presented for aluminum slabs with thicknesses of 100, 300, 1000, and 3000 mfps. As seen in **Figure 9**, it is possible to resolve the transmitted energy-loss spectra with a sufficiently accurate hybrid inelastic model. For 10000-keV electrons on aluminum, a two-energy hybrid model is required. However, for 1000-keV electrons on gold, it is possible to relax the inelastic model to a single energy with the same cutoff. In **Figure 10**, results for 1000-keV electrons on gold are presented. Under these conditions, inelastic scattering is also less peaked and the hybrid model can be relaxed. However, a discrete representation is still not sufficient.

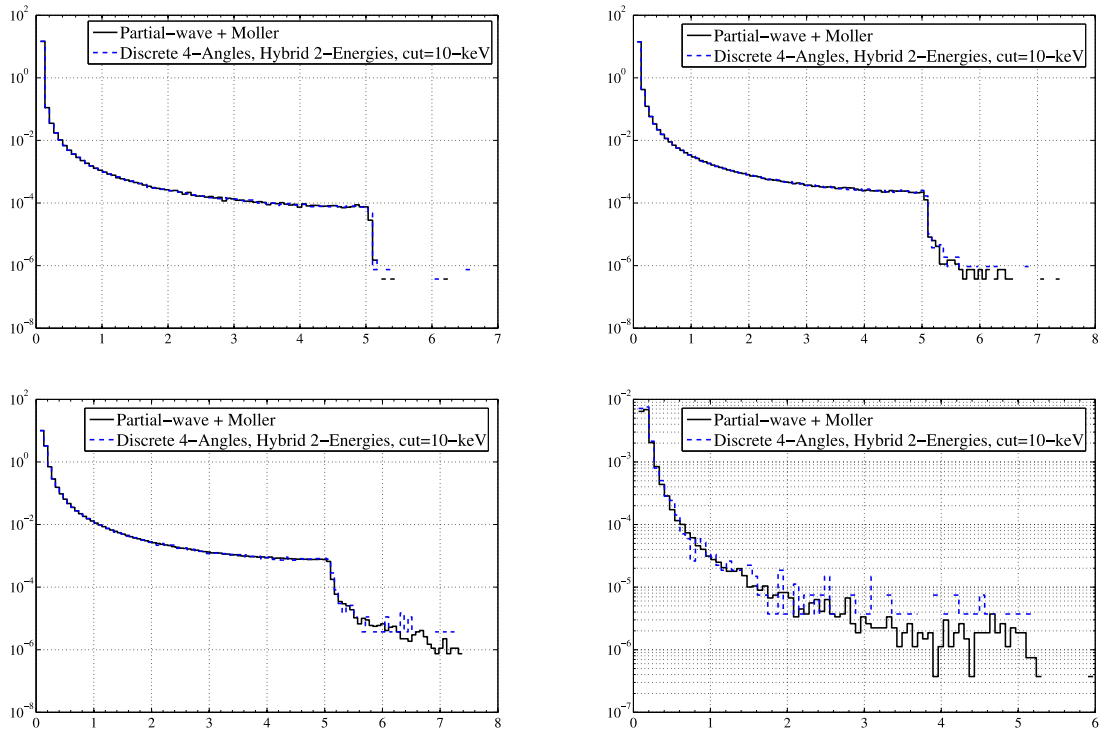


Figure 9: Impact of slab thickness on transmitted energy-loss spectra for 10000-keV electrons on aluminum.

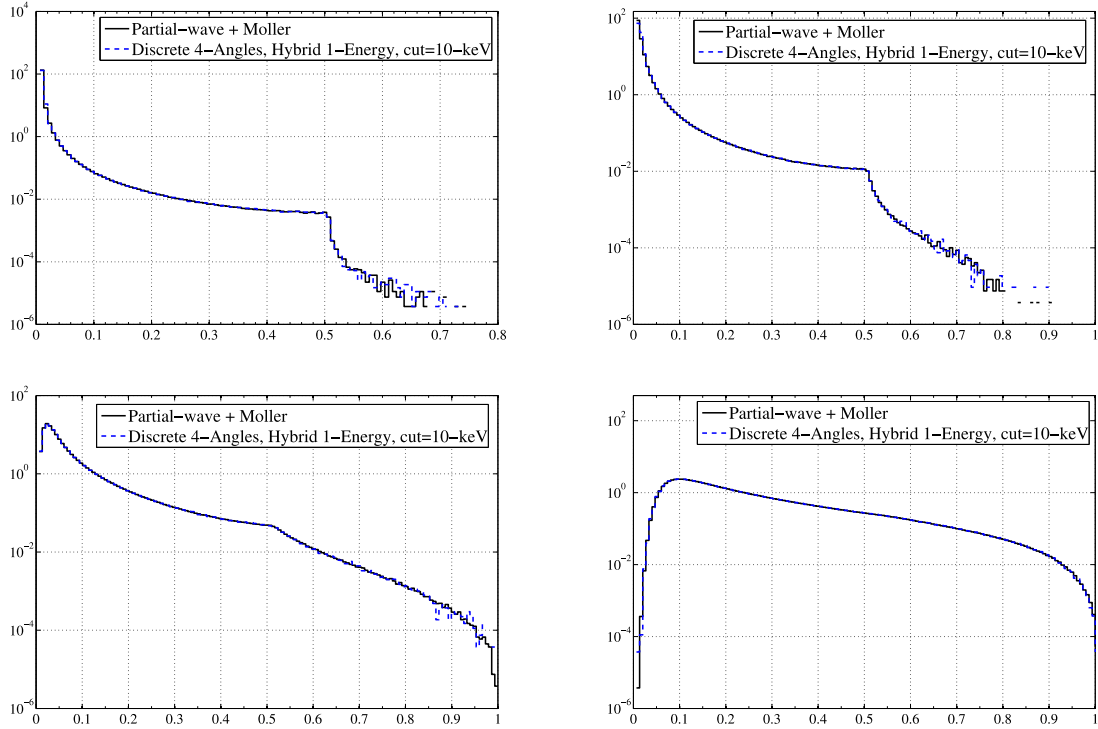


Figure 10: Impact of slab thickness on transmitted energy-loss spectra for 1000-keV electrons on gold.

Reflected energy-loss spectra for 10000-keV and 1000-keV electrons on gold are presented next. Reflected energy-loss spectra for 10000-keV electrons on aluminum are not presented because the reflected electrons experience almost no inelastic collisions. This is true even for gold as seen in **Figure 11** for slabs that are 100 and 300 analog mfps thick, where the distributions are nearly singular about zero energy-loss. That said, the hybrid model also predicts this nearly singular behavior. For thicker slabs, 1000 and 3000 analog mfps, the reflected energy-loss spectra spreads out more. Here, the hybrid model is in good agreement in the statistically significant regions of the spectra (that is, the peaked region of the spectra).

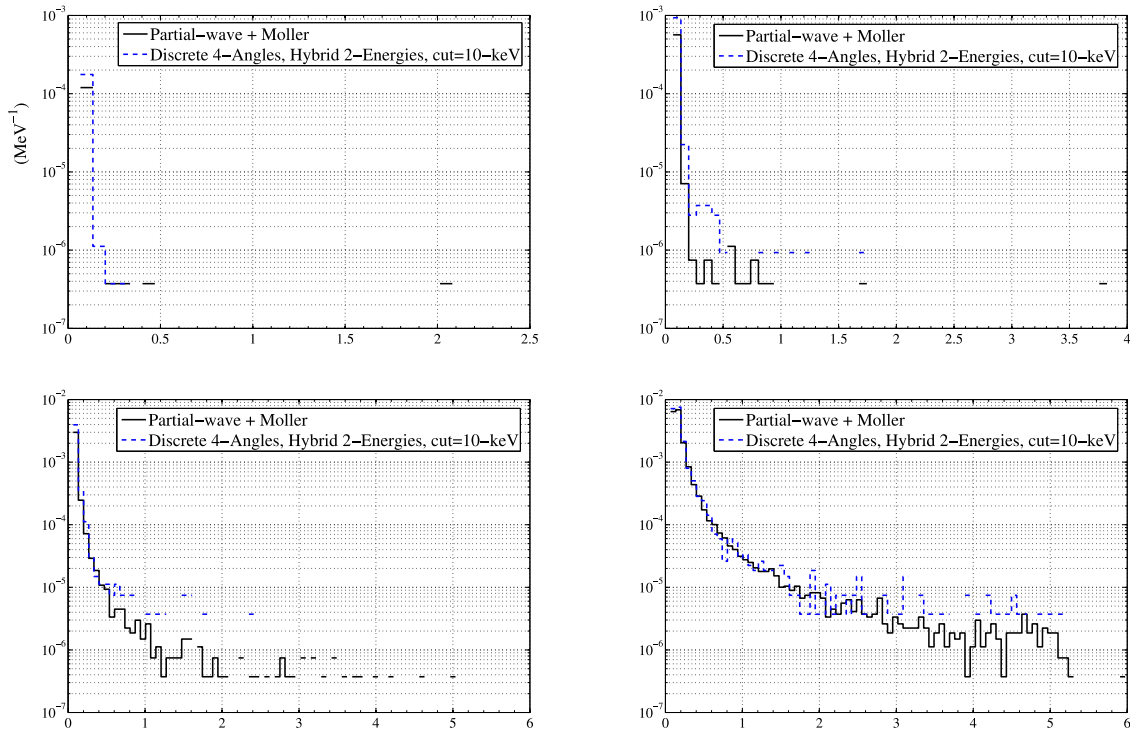


Figure 11: Impact of slab thickness on reflected energy-loss spectra for 10000-keV electrons on aluminum.

In **Figure 12**, reflected energy-loss spectra are presented for 1000-keV electrons on gold. Once again, in this less-peaked regime the spectra are not nearly as singular and a relaxed, single-energy hybrid model can be utilized.

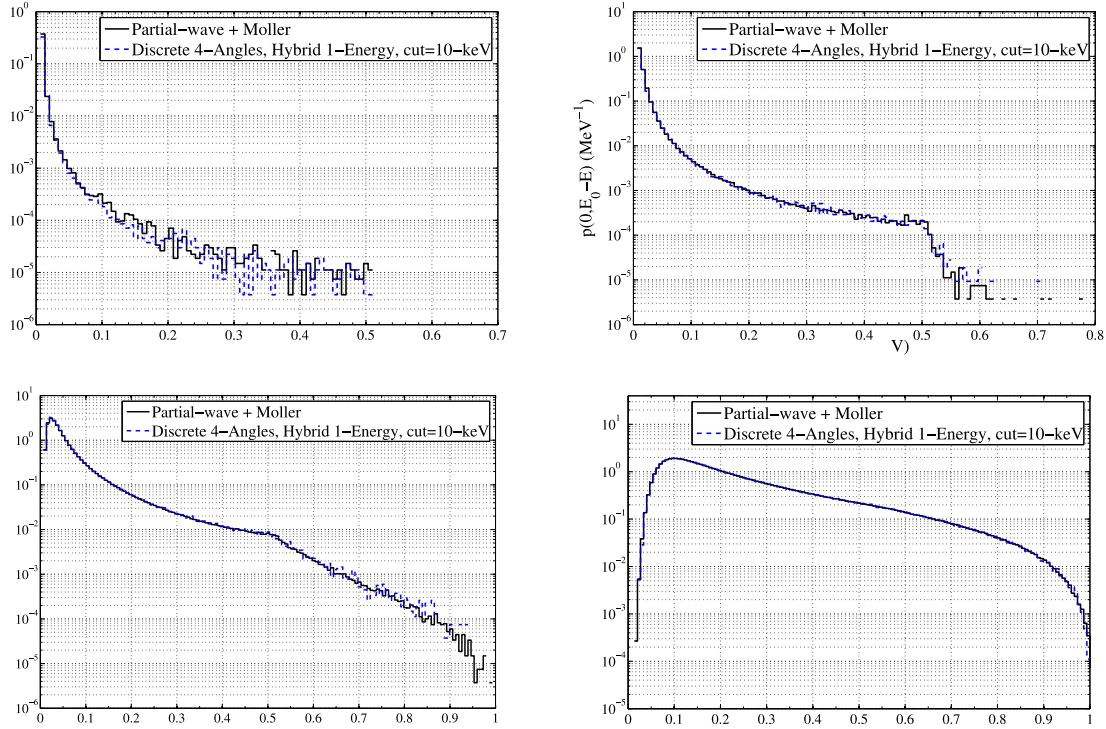


Figure 12: Impact of slab thickness on reflected energy-loss spectra for 1000-keV electrons on gold.

5.1.3. Efficiencies for Thin Slab Problems

In this section, efficiency results for the previously discussed thin slab problems are presented in **Table 1** and **Table 2** for 1000-keV and 10000-keV on aluminum or gold slabs of various thicknesses respectively. In general, efficiency gains depend on the slab thickness, the target atomic number, and the energy of the particle. The dependence on the problem geometry, or the slab thickness in particular, is captured in the following tables. The greatest efficiencies are realized in thicker slabs where particles undergo more collisions. In thin slabs (100 and 300 analog mfps), efficiency gains range from 5 to 60 times faster than analog Monte Carlo. Whereas for thicker slabs, efficiency gains range from one to three orders of magnitude faster than analog Monte Carlo.

In previous sections, it was mentioned that there is a trade-of between accuracy and efficiency. This will be clarified in remainder of this discussion. First, remember that under the most extreme conditions (10000-keV electrons on 100 to 300 mfps of aluminum) hybrid models were required to resolve angular distributions and energy spectra. The efficiency gains associated with these models, under these conditions range from 15-47 times the efficiency of an analog Monte

Carlo calculation. What would take a day now requires only an hour without sacrificing accuracy. Now, note that it was possible to resolve angular distributions for 1000-keV electrons on gold slabs with thicknesses of 1000 and 3000 mfps using various discrete models. Under these conditions, efficiency gains of 150-500 times the efficiency of an analog Monte Carlo calculation are realized without sacrificing accuracy. In this case, what would take a day takes less than ten minutes.

Table 1: Efficiency gains for various ROP DCSs when simulating 1000-keV and 10000-keV electrons incident on aluminum slabs 100, 300, 1000, and 3000 mfps thick.

Slab Width (mfps)	Particle Energy	Reduced Order Physics Model				
		1-Angle 1-Energy	4-Angles 1-Energy	4-Angles 4-Energies	1-Angle $\mu_0^* = 0.99$ 4-Energies	4-Angles 1-Energy $Q^* = 10 \text{ keV}$
100	1000-keV	21	18	15	5	10
	10000-kev	22	22	21	16	13
300	1000-keV	56	43	33	16	22
	10000-kev	60	62	55	48	27
1000	1000-keV	174	63	56	11	41
	10000-kev	200	170	145	86	85
3000	1000-keV	475	178	109	21	76
	10000-kev	610	556	360	114	71

Table 2: Efficiency gains for various ROP DCSs when simulating 1000-keV and 10000-keV electrons incident on gold slabs 100, 300, 1000, and 3000 mfps thick.

Slab Width (mfps)	Particle Energy	Reduced Order Physics Model				
		1-Angle 1-Energy	4-Angles 1-Energy	4-Angles 4-Energies	1-Angle $\mu_0^* = 0.99$ 4-Energies	4-Angles 1-Energy $Q^* = 10 \text{ keV}$
100	1000-keV	20	16	15	8	12
	10000-kev	19	20	19	17	20
300	1000-keV	61	37	33	10	26
	10000-kev	62	57	54	86	45
1000	1000-keV	174	63	56	18	30
	10000-kev	200	170	145	89	39
3000	1000-keV	565	134	122	23	91
	10000-kev	1174	861	591	255	254

In section 5.1.1 and 5.1.2, it was shown that for a given ROP DCS model, the accuracy of the result depends on the peakedness of the distribution being resolved. The peakedness of the distribution, in turn, depends on the slab thickness and the regime of scattering, which is a function of particle energy and target atomic number. Regardless, an ROP DCS can be made to

preserve additional moments of the analog DCS; thus, refining the model and achieving analog level accuracy under very extreme simulation conditions. While it is not possible to achieve several orders of magnitude efficiency gains under these conditions, the ROP models were at least five times faster than analog Monte Carlo and up to 45 times faster in some cases. Under more relaxed conditions, up to three orders of magnitude efficiency gains were achieved. Regardless, accuracy and efficiency suitable for a wide variety of problems can be realized by adjusting the ROP DCSs.

5.2. Longitudinal and Lateral Distributions

At this point, it is clear that accuracy and efficiency is problem dependent. Nonetheless, it is possible to refine the ROP DCS such that sufficient levels of accuracy and efficiency are realized. In this section, a few additional results are presented that overlap with the previous section in the sense that problems corresponding to scattering regimes ranging from extreme peakedness to less-extreme peakedness are tested. Here, results in connection with Lewis theory are presented to demonstrate the moment-preserving property of this method, while again demonstrating the accuracy of this method is systematically controllable.

In particular, longitudinal and lateral distributions for 100-keV, 1000-keV, and 10000-keV electrons after traveling a distance of 100, 300, 1000, and 3000 mfps in an infinite medium of copper are presented (similar to Benedito et al. [64]). In these problems, energy-loss is not considered. The longitudinal and lateral distributions are generated using the analog Monte Carlo method where elastic scattering is given by the partial-wave DCS. These distributions are referred to as the analog benchmark and are compared with several solutions generated using discrete and hybrid models. In all of the results presented in this section, $4\text{E}+07$ electrons were simulated for each model and uncertainties associated with the majority of the results are within 1%; especially, in the highly probable regions. However, in regions where the distribution is small with respect to the maximum value (for example, in the tails of the distributions), the results are statistically insignificant.

In **Figure 13**, a diagram of the problem simulated is presented. The electron starts at $s = 0$ with an initial direction and travels until reaching a distance of $s = s_{max}$. At this point, the electrons longitudinal displacement, or the projection of the path traveled onto the initial trajectory, and lateral displacement, or the orthogonal projection of the pathlength, is tallied. Although it is not clear from **Figure 13**, it is possible for an electron to turn around and travel in directions opposite to the initial direction. In these cases, it is possible for the electron to have a negative longitudinal displacement. The same is not true for lateral displacement because the lateral displacement is a measure of radius and therefore, non-negative.

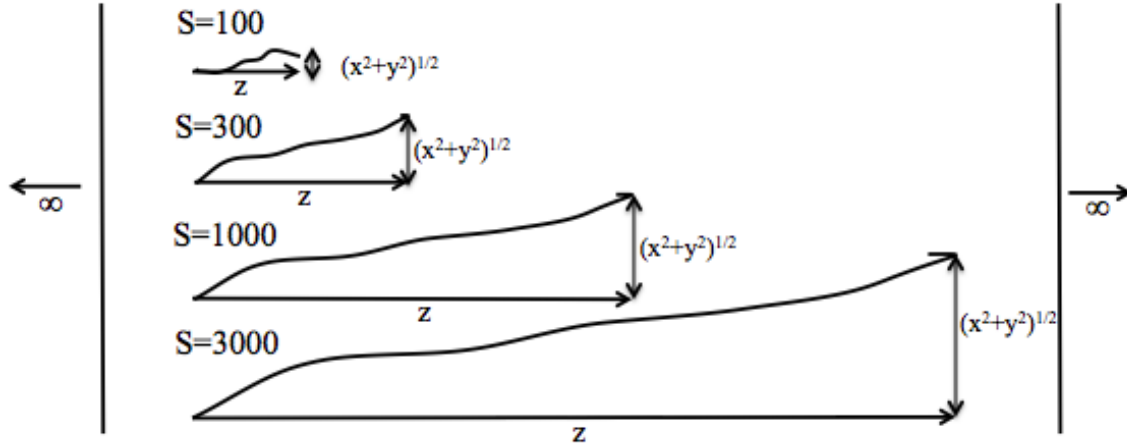


Figure 13: Infinite medium problem setup.

In addition to the longitudinal and lateral distributions, a few Lewis moments are compared including $\langle z \rangle$ and $\langle x^2 + y^2 \rangle$ or

$$\langle z \rangle = \int_{4\pi} d\Omega \int_{-\infty}^{\infty} dx \int_{-\infty}^{\infty} dy \int_{-\infty}^{\infty} dz z \psi(x, y, z, s, \vec{\Omega}). \quad (54)$$

and

$$\langle x^2 + y^2 \rangle = \int_{4\pi} d\Omega \int_{-\infty}^{\infty} dx \int_{-\infty}^{\infty} dy \int_{-\infty}^{\infty} dz (x^2 + y^2) \psi(x, y, z, s, \vec{\Omega}). \quad (55)$$

Here, the Monte Carlo method is used to carry out the integrals in Eqs. (54) and (55), by simulating the particle transport and tallying the longitudinal and lateral displacement after traveling 100, 300, 1000, or 3000 analog mfps. These results are presented in the following tables for each energy. As predicted by Lewis theory and seen in

Table 3, models preserving at least $\Sigma_{el,1}$ will preserve $\langle z \rangle$. Therefore, even the very efficient single-angle model will have the correct average longitudinal displacement. Once again as predicted by Lewis theory and seen in **Table 4**, models preserving at least $\Sigma_{el,1}$ and $\Sigma_{el,2}$ will preserve $\langle x^2 + y^2 \rangle$. Therefore, the single-angle model that preserves $\Sigma_{el,1}$ and $\Sigma_{el,2}$ will have the correct average lateral displacement as well. Models preserving additional moments are not presented in

Table 3 and **Table 4** because these results are redundant. Preservation of average longitudinal and lateral displacement are important to electron transport methods and in many cases these methods seek to preserve at least average longitudinal and lateral displacement. One of the major distinctions between condensed history and the MP method is that typically in condensed history the underlying multiple scattering theory is only setup to preserve $\Sigma_{el,1}$ and $\Sigma_{el,2}$, while the MP method can preserve an arbitrary number of Legendre moments guaranteeing preservation of

higher-order Lewis moments. Not to mention, the most simple, efficient ROP model associated with the MP method preserves at least the average longitudinal and lateral distances.

Table 3: Average longitudinal displacement for 100-keV, 1000-keV, and 10000-keV electrons in copper traveling a distance of 100, 300, 1000, and 3000 mfps.

Pathlength (mfps)	Particle Energy (keV)	$\langle z \rangle$		
		Analog	1-Angle	Rel. Unc.
100	100	0.8432	0.8433	0.00006
	1000	0.986667	0.98667	0.00001
	10000	0.999644	0.999644	0.000001
300	100	0.61815	0.61820	0.0002
	1000	0.96069	0.96070	0.00004
	10000	0.998931	0.998932	0.000005
1000	100	0.2761	0.2763	0.001
	1000	0.87673	0.87680	0.0001
	10000	0.996449	0.996448	0.00001
3000	100	0.09493	0.09497	0.006
	1000	0.6861	0.6863	0.0007
	10000	0.989399	0.989387	0.00005

Table 4: Average lateral displacement for 100-keV, 1000-keV, and 10000-keV electrons in copper traveling a distance of 100, 300, 1000, and 3000 mfps.

Pathlength (mfps)	Particle Energy (keV)	$\langle x^2 + y^2 \rangle$		
		Analog	1-Angle	Rel. Unc.
100	100	0.154457	0.154456	0.0003
	1000	0.016420	0.016415	0.0008
	10000	0.000455	0.000454	0.003
300	100	0.26942	0.26944	0.0004
	1000	0.04683	0.04682	0.0009
	10000	0.001365	0.001364	0.004
1000	100	0.2365	0.2366	0.0007
	1000	0.1315	0.1314	0.001
	10000	0.004524	0.004525	0.0009
3000	100	0.11012	0.11016	0.002
	1000	0.2532	0.2531	0.001
	10000	0.01338	0.01339	0.004

Although preservation of $\Sigma_{el,1}$ and $\Sigma_{el,2}$ guarantees preservation of $\langle z \rangle$ and $\langle x^2 + y^2 \rangle$, resolving the longitudinal and lateral distributions requires preservation of additional moments. Similar to

results from the previous section, discrete artifacts impact the shape of the longitudinal and lateral distributions. The impact of the artifacts is again dependent on the peakedness of the scattering and the number of collisions suffered by the electrons before tallying their displacement.

In **Figure 14** through **Figure 19**, longitudinal and lateral distributions for 10000-keV down to 100-keV electrons in an infinite copper medium are presented. Each figure contains four results corresponding to gradually increasing pathlengths of 100, 300, 1000, and 3000 mfps. Again, the most challenging problem, or longitudinal and lateral distributions for 10000-keV electrons in copper, is presented first in **Figure 14** and **Figure 15**. In all cases, the hybrid DCS utilized is in excellent agreement with the analog benchmark. For shorter pathlengths, both discrete models oscillate about the analog benchmark. The oscillations are an effect resulting from the discreteness of the DCS model where electrons tend to travel in preferential directions. Even for pathlengths of 1000 analog mfps, the 16-angle discrete model still oscillates subtly about the analog benchmark, but does not for pathlengths of 3000 analog mfps.

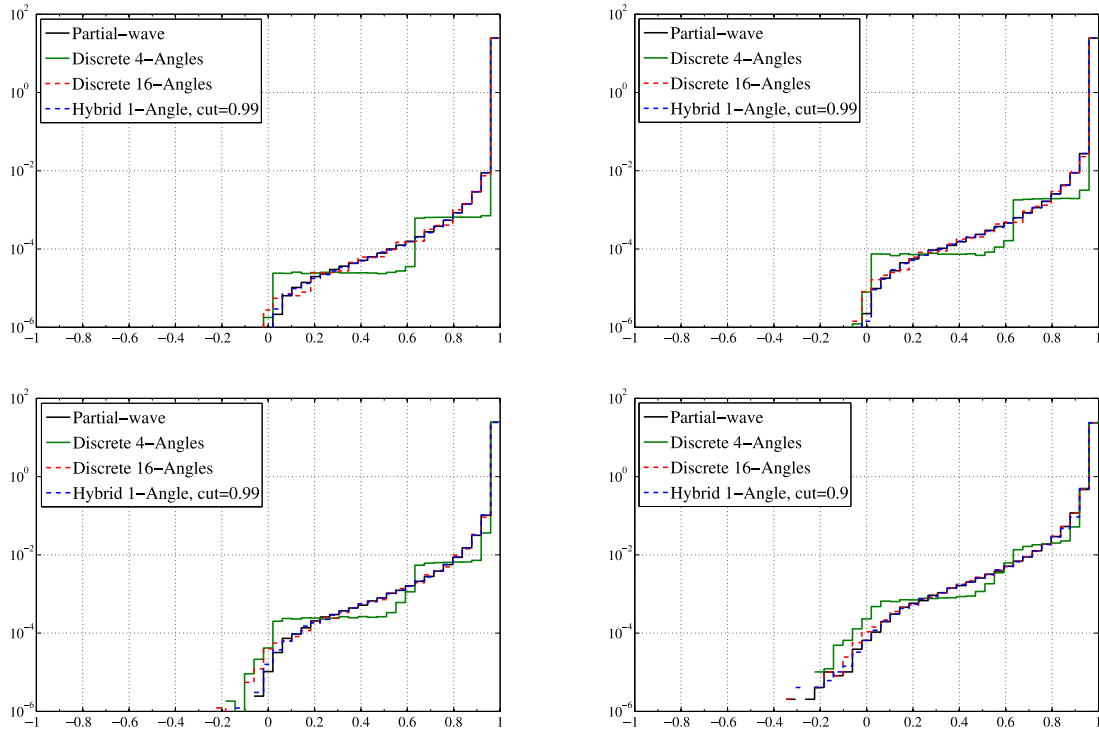


Figure 14: Comparison of longitudinal distributions for 10000-keV electrons after traveling a distance of 100 (top left), 300 (top right), 1000 (bottom left), and 3000 (bottom right) analog elastic mfps.

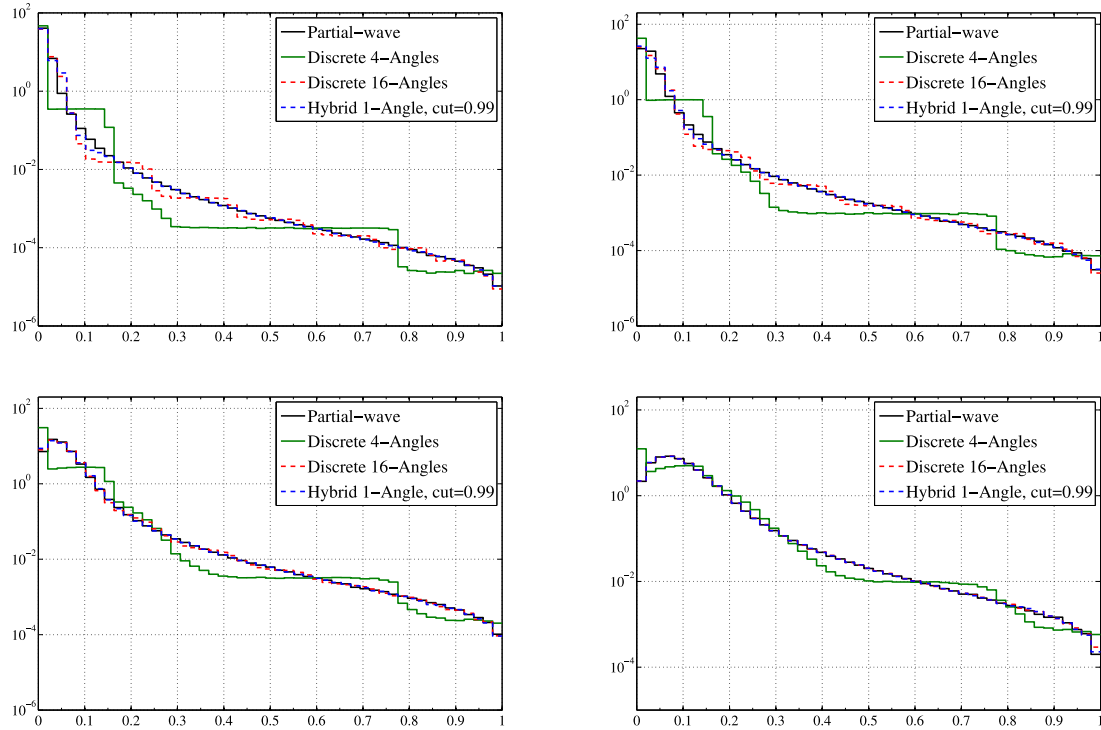


Figure 15: Comparison of lateral distributions for 10000-keV electrons after traveling a distance of 100 (top left), 300 (top right), 1000 (bottom left), and 3000 (bottom right) analog elastic mfps.

As the energy of the particle decreases, the effectiveness of relaxed models (that is, models preserving fewer moments) is improved. For example, longitudinal and lateral distributions for 1000-keV electrons in copper are presented first in **Figure 16** and **Figure 17**. In all cases, the hybrid DCS utilized is in excellent agreement with the analog benchmark and was relaxed from a cutoff of 0.99 down to a cutoff of 0.9 for pathlengths of 100 and 300 analog mfps and down to a cutoff of 0.5 for pathlengths of 1000 and 3000 analog mfps. Moreover, discrete artifacts are not nearly as significant for 1000-keV electrons with exception of longitudinal and lateral distributions for pathlengths of 100 and 300 analog mfps. In fact, a 4-angle discrete model is sufficient for resolving longitudinal and lateral distributions for pathlengths of 1000 and 3000 analog mfps.

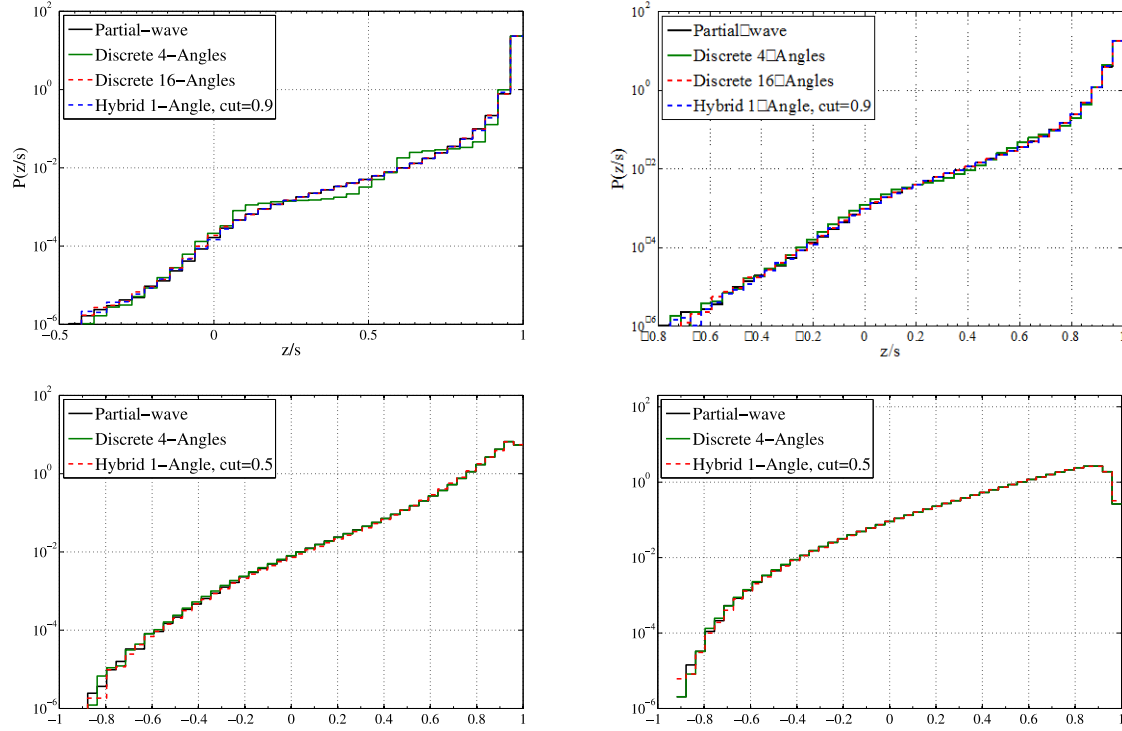


Figure 16: Comparison of longitudinal distributions for 1000-keV electrons after traveling a distance of 100 (top left), 300 (top right), 1000 (bottom left), and 3000 (bottom right) analog elastic mfps.

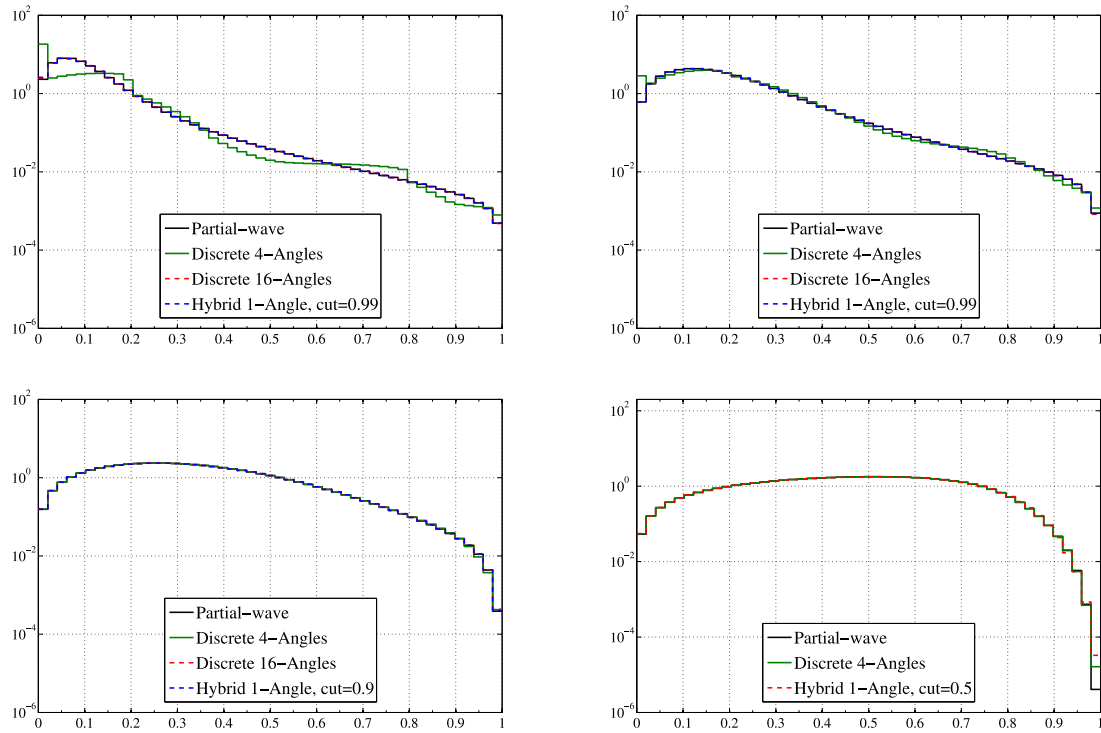


Figure 17: Comparison of lateral distributions for 1000-keV electrons after traveling a distance of 100 (top left), 300 (top right), 1000 (bottom left), and 3000 (bottom right) analog elastic mfps.

Finally for 100-keV electrons, the most relaxed models tested are sufficient for pathlengths down to 100 analog mfps as seen in **Figure 18** and **Figure 19**. Although single-angle results were not presented, a single-angle model is reasonably accurate for 100-keV electrons for pathlengths of 100 analog mfps and greater.

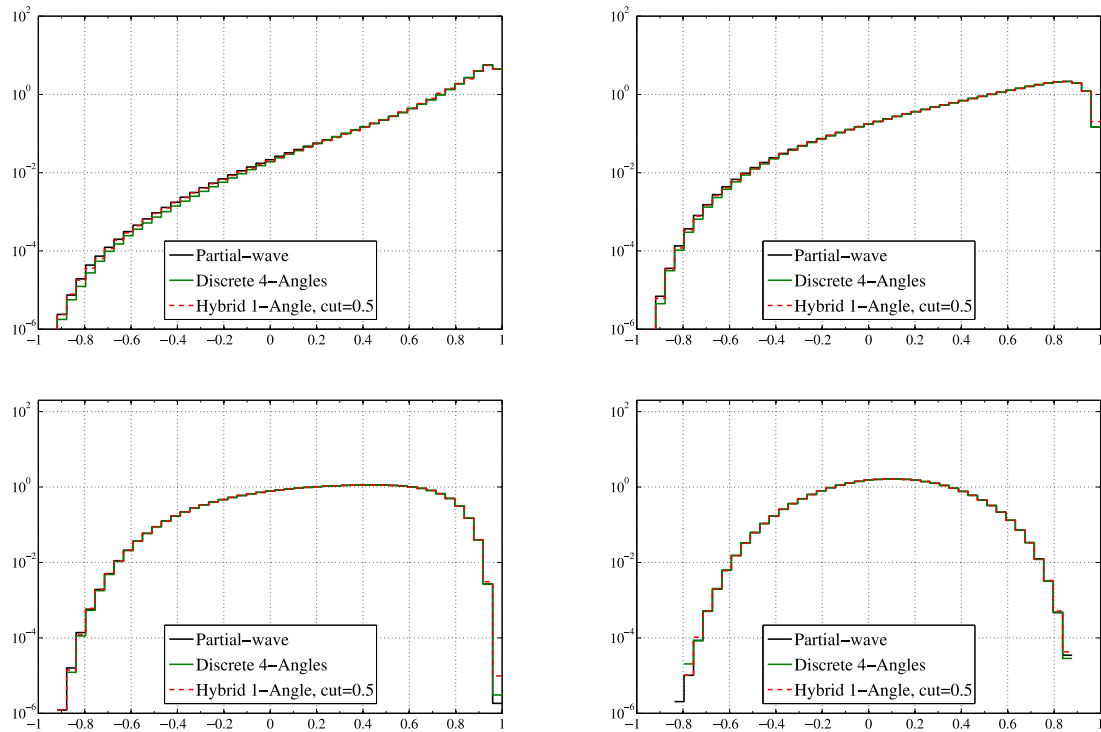


Figure 18: Comparison of longitudinal distributions for 100-keV electrons after traveling a distance of 100 (top left), 300 (top right), 1000 (bottom left), and 3000 (bottom right) analog elastic mfps.

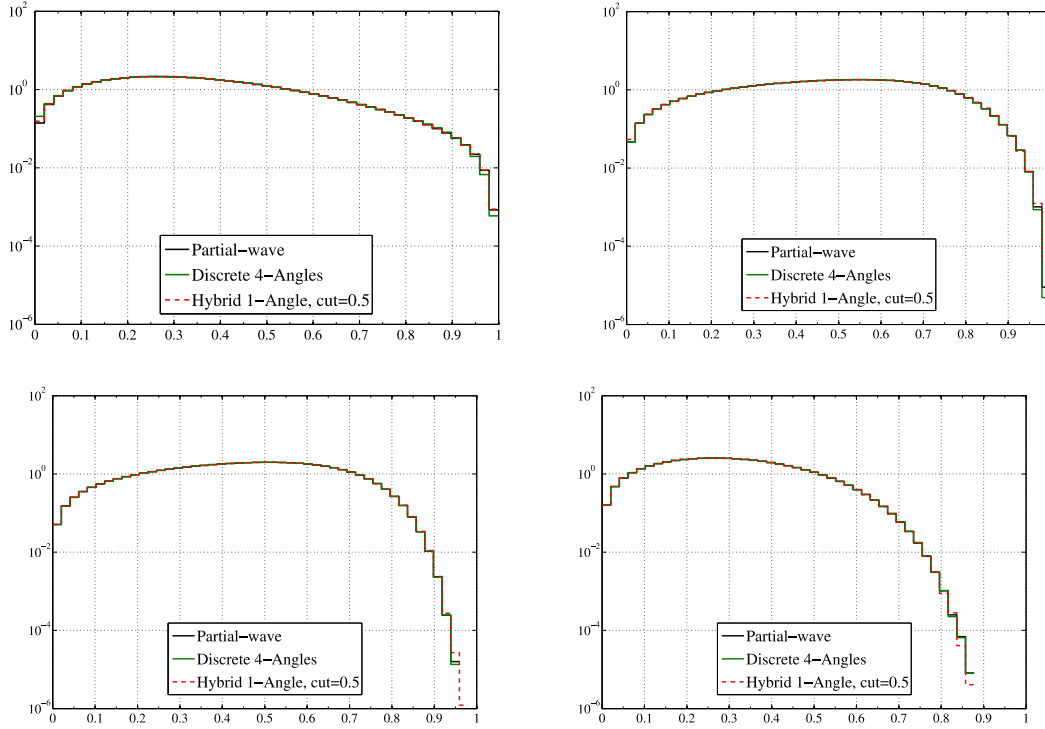


Figure 19: Comparison of lateral distributions for 100-keV electrons after traveling a distance of 100 (top left), 300 (top right), 1000 (bottom left), and 3000 (bottom right) analog elastic mfps.

In this section, longitudinal and lateral results were presented to demonstrate the effectiveness of the MP method when calculating quantities that are critical to most CH methods and electron transport methods in general. It was shown that the average longitudinal and lateral displacement (typically used in CH pathlength correction algorithms) is in exact agreement with analog results for a single-angle (two moment-preserving) model. In other words, no additional pathlength correction algorithm is required in the MP method because the ROP DCS are constructed such that the Lewis moments are inherently preserved. In addition, longitudinal and lateral distributions for 100-keV (less-peaked scattering) to 10000-keV (highly-peaked scattering) were generated using various ROP models. Depending on the problem at hand, ROP models requiring preservation of only a few moments were required for agreement with the analog benchmark. When necessary, additional moments were preserved to achieve analog level accuracy, but there was never a problem too extreme that the MP method failed to resolve the longitudinal or lateral distributions.

5.3. 1-D and 2-D Dose Calculations

In this section, 1-D and 2-D dose results are presented. The dose results were generated using the partial-wave elastic scattering DCS and the Moller inelastic scattering model for the analog benchmark and the ROP DCSs were, in turn, constructed from these DCSs. Secondary

production was not considered for this section. The following results show that the MP method can be used to calculate dose accurately in both relatively isotropic and highly peaked regimes regardless of the form of the analog model used to construct the ROP DCS. That is, accurate models can be constructed from both analytical DCS and tabulated DCS data. In this report the emphasis is on tabulated elastic DCS data, as applications of the MP method to analytical DCSs has been demonstrated in the past [58, 59]. Efficiency gains improve significantly with increasing source energies without sacrificing accuracy. The trade-off between accuracy and efficiency, where it exists, ultimately depends on the application and the level of accuracy required by the user.

5.3.1. One-Dimensional Depth-Dose Profiles

Transversely integrated depth-dose profiles and relative differences are presented for 250-keV electrons in gold and 20000-keV electrons in water. In **Figure 20**, the results are nearly indistinguishable from the benchmark. However, the relative error plot in **Figure 20** shows disagreements that would otherwise be indistinguishable. In this simulation, disagreement is attributed to both the elastic and inelastic scattering models. Additional angles or use of the hybrid DCS smooths out the overestimation in the first cell. Adding another energy point to the discrete inelastic model smooths out the oscillation that begins near the peak dose. Though some refinement was necessary, only small adjustments were required to reduce the relative differences to within 1%.

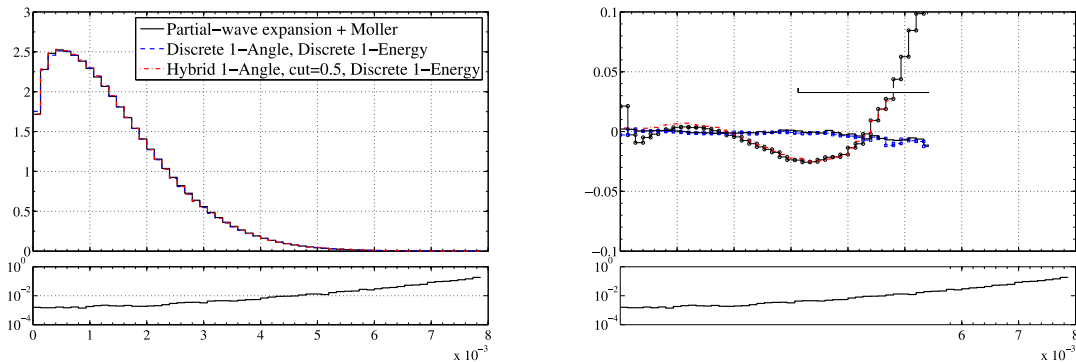


Figure 20: Dose deposition profile (left) and relative error (right) for 250-keV electrons on a gold slab.

Efficiency gains are presented in Tables 9.5 and 9.6. For 250-keV electrons in gold efficiencies range from about 3 to 50 times faster than analog depending on the accuracy of the ROP DCS used. For 20000-keV electrons, in gold efficiencies range from about 70 to 1800 times faster than analog, while achieving accuracies nearly the same as those presented in Fig. 9.18b.

Table 5: Efficiency gains for various discrete DCSs when calculating dose due to 250-keV, 1000-keV, and 20000-keV electrons on gold slabs.

Particle Energy	Reduced Order Physics Model				
	1-Angle 1-Energy	2-Angles 1-Energy	2-Angles 2-Energies	4-Angles 1-Energy	4-Angles 4-Energies
250-keV	51	23	23	11	11
1000-keV	164	72	71	31	31
20000-keV	1794	967	883	416	379

Table 6: Efficiency gains for various hybrid DCSs when calculating dose due to 250-keV, 1000-keV, and 20000-keV electrons on gold slabs.

Particle Energy	Reduced Order Physics Model		
	$\mu_0^* = 0.5$	$\mu_0^* = 0.9$	$\mu_0^* = 0.99$
	1-Angle 2-Energies	1-Angle 2-Energies	1-Angle 2-Energies
250-keV	18	7	3
1000-keV	60	22	6
20000-keV	844	302	68

In **Figure 21**, the results are distinguishable from the benchmark at 20000-keV because the relaxed approximations do not capture large angle scatter or large energy losses. Once again, small refinements to the elastic and inelastic ROP scattering models improve the accuracy of the results. As seen in **Figure 21**, model refinement through preservation of additional moments reduces the relative differences to <1%. Efficiency gains for the 20000-keV water simulation range from about 110 to 1600. However, accuracies within 1% were achieved with models that were 650 to 700 times more efficient than analog. Additional efficiency gains are presented in Tables 9.7 and 9.8.

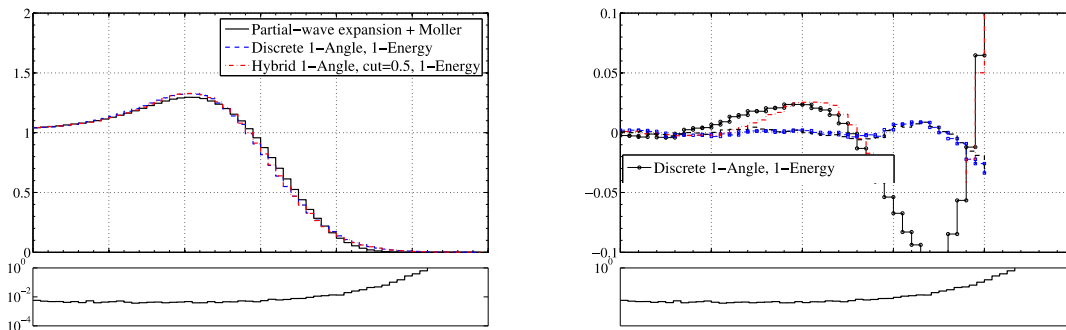


Figure 21: Dose deposition profile and relative error for 20000-keV e^- on H₂O.

Table 7: Efficiency gains for various discrete DCSs when calculating dose due to 250-keV, 1000-keV, and 20000-keV electrons on water slabs.

Particle Energy	Reduced Order Physics Model				
	1-Angle 1-Energy	2-Angles 1-Energy	2-Angles 2-Energies	4-Angles 1-Energy	4-Angles 4-Energies
250-keV	54	30	24	15	11
1000-keV	147	83	61	39	27
20000-keV	1607	1122	709	612	293

Table 8: Efficiency gains for various hybrid DCSs when calculating dose due to 250-keV, 1000-keV, and 20000-keV electrons on water slabs.

Particle Energy	Reduced Order Physics Model		
	$\mu_0^* = 0.5$	$\mu_0^* = 0.9$	$\mu_0^* = 0.99$
	1-Angle 2-Energies	1-Angle 2-Energies	1-Angle 2-Energies
250-keV	20	9	3
1000-keV	52	25	7
20000-keV	647	380	109

In addition to the single-material depth-dose profiles, an interface problem is presented. In this problem a 150-keV pencil beam of electrons is normally incident on a gold-aluminum slab. The first 0.0004 cm of the slab is gold and the remainder of the slab is aluminum. In **Figure 22**, the depth-dose profiles for the analog benchmark and a single-angle, single-energy discrete model are presented along with the relative error in several discrete models. The interface occurs between the 4th and 5th cells; however, there is no distinguishable error in **Figure 22** resulting from the interface. As previously noted, the MP method preserves transport mechanics allowing for exponentially distributed collision sites. Clearly, boundary crossings are a non-issue for this method and no additional algorithms are required to handle boundary crossings.

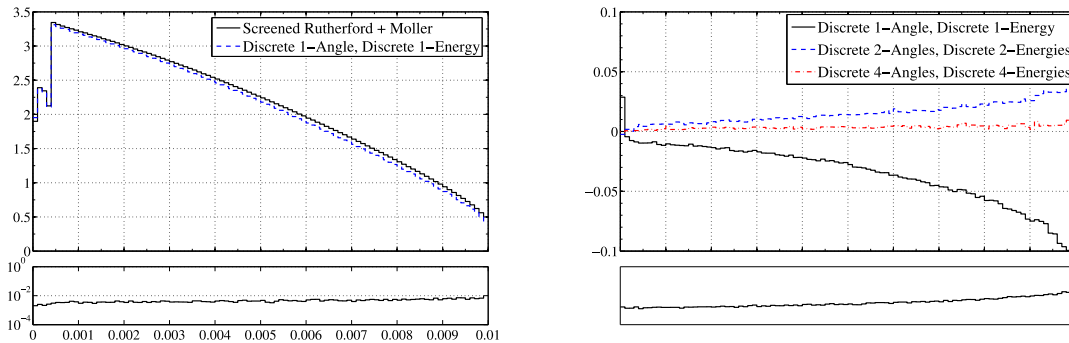


Figure 22: Dose deposition profile (left) and relative error (right) for 150-keV electrons on a gold/aluminum slab.

5.3.2. Two-Dimensional Dose Deposition

As indicated by the transversely integrated dose results in the previous section, this method provides excellent accuracy and efficiency when radial spreading is not considered. However, in this section we present two-dimensional dose deposition results that include the impact of radially spreading. At lower energies this method is more effective at capturing radial spreading. We begin the two-dimensional dose deposition results by presenting the low energy simulation. The geometry setup for this simulation is presented in **Figure 23**. For the 150-keV simulation 109 histories were completed. In **Figure 23**, the analog benchmark for the 150-keV simulation is presented. A significant portion of the dose is deposited along the beamline close to the source. In the gold region the dose is deposited more rapidly than in the silicon region where it is apparent that the dose diffuses slower.

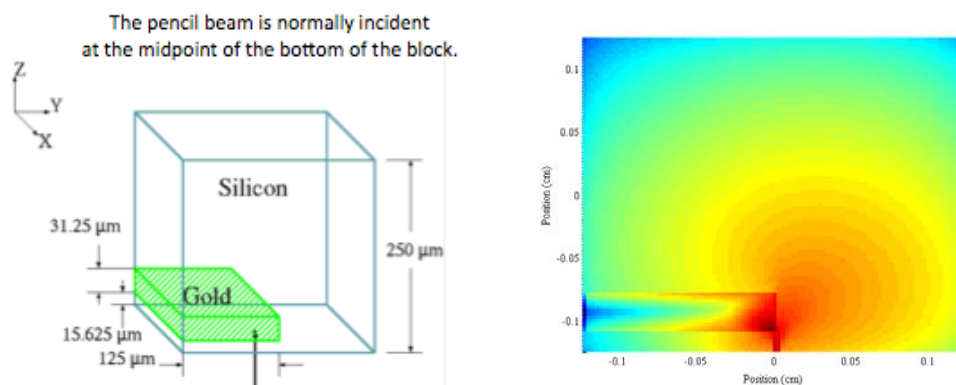


Figure 23: Problem setup (left) and analog benchmark (right) for 150-keV electrons on a silicon cube with gold region.

In **Figure 24**, relative differences for discrete models are presented to demonstrate the impact of adjusting the number of discrete angles and energies, and in turn, the number of moments preserved. In **Figure 24** (top), low-order moment-preserving models are presented. Discrete artifacts are very distinct in **Figure 24** (top left) for the single-angle, single-energy model. By increasing the number of discrete angles in **Figure 24** (bottom), the discrete artifacts are mitigated without requiring the hybrid model. However, there are still some significant differences in the dose in some regions resulting from the single-energy model seen in **Figure 24** (top right and bottom left). By including additional energies, the relative error in all regions is significantly reduced as seen in **Figure 24** (bottom right). Notice that along the gold-silicon interface near the beam, the agreement is within 1%, with exception of the single-angle model where the solution is overwhelmed with discrete artifacts.

Another artifact to point out is the over/under estimation of the dose in the first two cells next to the source. This error persists as the models are refined, but it is actually an artifact of the source type and source location. That is, the source is a pencil beam that is singular in space and it is directed at the tally cell boundary between. In the next 2-D result, the source is no longer singular in space and the artifact is no longer present.

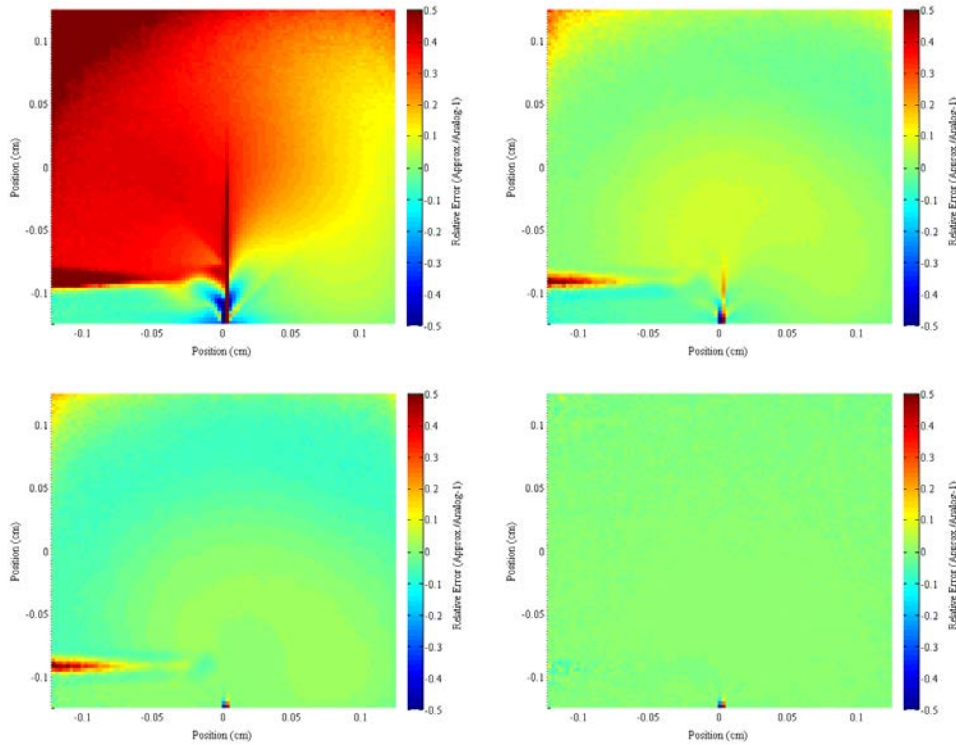


Figure 24: Relative error in discrete 1-Angle, 1-Energy model (top left), discrete 2-Angles, 1-Energy model (top right), discrete 4-Angles, 1-Energy model (bottom left), discrete 4-Angles, 4-Energies model (bottom right) for 150-keV electrons on silicon/gold cube.

Table 9: Efficiency gains for various discrete DCSs when calculating dose due to 150-keV electrons on silicon/gold cube.

Particle Energy	Reduced Order Physics Model				
	1-Angle 1-Energy	2-Angles 1-Energy	2-Angles 2-Energies	4-Angles 1-Energy	4-Angles 4-Energies
250-keV	51	29	29	16	16

In **Figure 25** (left), the two-dimensional problem setup is given along with the analog benchmark in **Figure 25** (right). In this simulation, a beam of 10000-keV electrons are transported with radius of 0.02 cm is normally incident on a water cube with a small bone region. The analog benchmark is in logscale and provides a sense of where most of the dose is deposited. That is, a significant portion of the dose is deposited along the beamline within fractions of a cm to the left and right of the origin. The electrons with these energies penetrate deeply into the medium as seen in **Figure 25** (right).

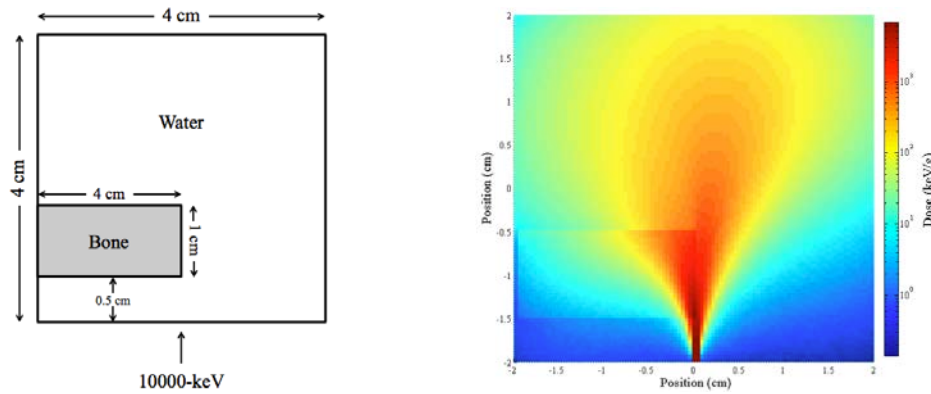


Figure 25: Problem setup (left) and analog benchmark (right) for 10000-keV electrons on a water cube with bone region.

The following figure presents relative error results corresponding two discrete ROP DCS models. In **Figure 26** (left), the relative error in the four-angle, four-energy discrete DCS models with respect to the analog benchmark is presented. Discrete artifacts can be seen clearly in **Figure 26** (left). However, by refining the model through preservation of additional moments with the addition of four more discrete angles, discrete artifacts are mitigated and backscatter is captured more accurately as seen in the relative error result in **Figure 26** (right). In both the four-angle and eight-angle results, no interface effects are present. It should be noted that in the backscatter is not significant at 10000-keV and some of the error in the lower left and right corners is statistical in nature.

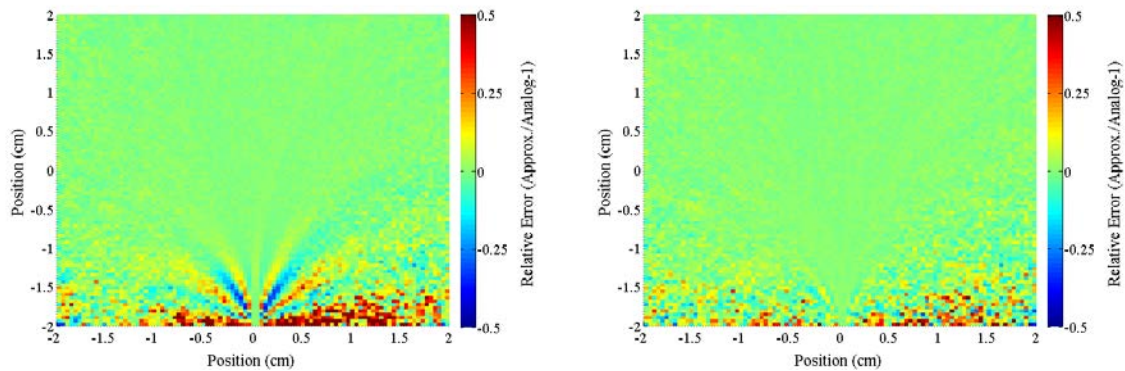


Figure 26: Relative error in discrete 4-Angles, 4-Energies model (left) and discrete 8-Angles, 4-Energies model (right) for 10000-keV electrons on water/bone cube.

In **Figure 27**, the relative error between the analog benchmark and two hybrid models are presented. In **Figure 27** (left), a hybrid model with $\mu^* = 0.9$ shows very subtle discrete artifacts, but otherwise is in good agreement. In **Figure 27** (right), a hybrid model with $\mu^* = 0.99$ does not suffer from any discrete artifacts and the only disagreement is in the lower left and right corners where again the error is statistical in nature.

In adding more discrete angles, or through use of the hybrid model, we demonstrated an approach to mitigate discrete artifacts through controlling the accuracy of the ROP DCS models. The only drawback to applying a more accurate ROP DCS model is the loss of efficiency as presented in Table 9.10. Here, the 4-angle model is the most efficient as expected. Inclusion of additional discrete angles or use of the hybrid model reduces the efficiency gain from roughly 120 to between 47 and 94.

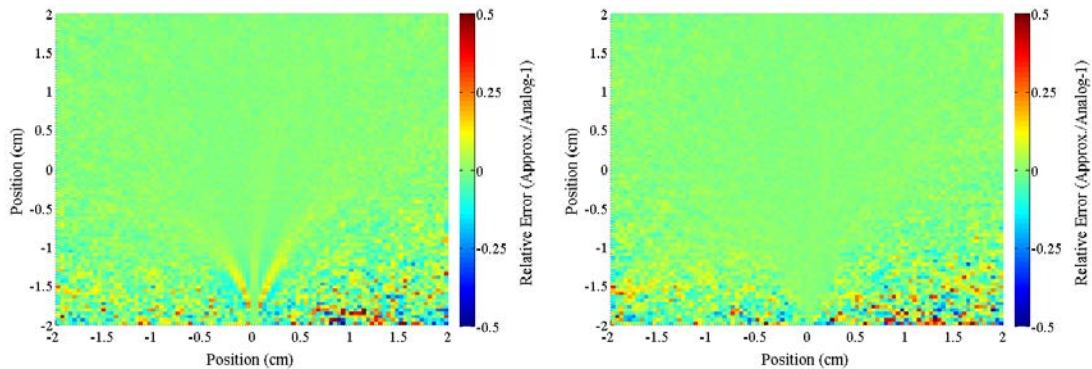


Figure 27: Relative error in hybrid 1-Angle with cutoff of 0.9, discrete 4-Energies model (left) and hybrid 1-Angle with cutoff of 0.99, discrete 4-Energies model (right) for 10000-keV electrons on water/bone cube.

Table 10: Efficiency gains for various discrete DCSs when calculating dose due to 10000-keV electrons on water/bone cube.

Particle Energy	Reduced Order Physics Model				As previously noted, it is possible to optimize
	4-Angles	8-Angles	1-Angle	1-Angle	
	4-Energies	4-Energies	$\mu_0^* = 0.9$ 4-Energies	$\mu_0^* = 0.99$ 4-Energies	
10000-keV	121	86	94	47	

such that significant reduction in efficiency is not incurred by applying higher-order models in regions nearby the source where the solution remains highly peaked and splaying lower-order models in regions where the solution is less-peaked. The following results present region dependent elastic ROP DCSs.

In **Figure 28**, the schematic for a region dependent discrete elastic model is presented along with the associated relative error from such an approach. As seen in **Figure 28** (left), default 4-angle, 4-energy discrete model is applied to all regions. The default is then deactivated in the region bounded by the red dashed line and an 8-angle, 4-energy discrete model is applied in this region. The associated relative error is given in **Figure 28** (right). The relative error in **Figure 28** (right) is nearly indistinguishable from the relative error in **Figure 28** (right) where an 8-angle discrete model is applied everywhere. The resulting gain in efficiency is 106 times faster than the analog simulation as opposed to 86 when applying an 8-angle model to all regions.

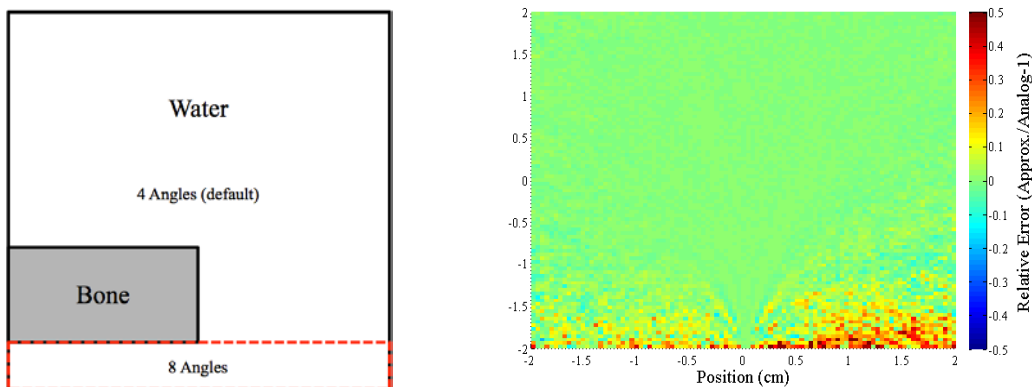


Figure 28: Schematic for region dependent ROP DCS (left) and the relative error in dose (right) for 10000-keV electrons on a water cube with bone region.

In **Figure 29**, the schematic for another region dependent discrete elastic model is presented along with the associated relative error from such an approach. Again, in this problem a 4-energy discrete inelastic model is used in all regions. As seen in **Figure 29** (left), an 8-angle model is applied in the region where the peak dose occurs and a single-angle model is applied in all other regions. The associated relative error is given in **Figure 29** (right) and is a modest improvement over the relative error in **Figure 29** (right) as the backscatter is captured more accurately. Again, the relative error in **Figure 29** (right) is nearly indistinguishable from the relative error in **Figure 29** (right) where an 8-angle discrete model is applied everywhere. The resulting gain in efficiency is 97 times faster than the analog simulation and is reduced slightly from 106, which was efficiency gain associated with the previous region dependent models, but accuracy was improved.

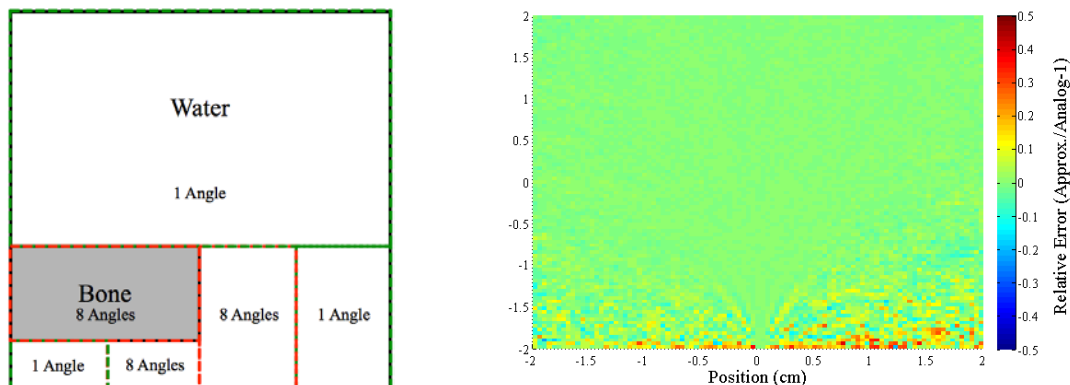


Figure 29: Schematic for region dependent ROP DCS (left) and the relative error in dose (right) for 10000-keV electrons on a water cube with bone region.

Ultimately, a region dependent application of the ROP DCS models is simply an exercise in demonstrating that accuracy and efficiency can be optimized. In practice, a more suitable approach would be to develop an algorithm that determines the optimal DCS model as the electron is transported. At this point, it is unclear what metric should be ideal for determining the

optimal ROP DCS model because the parameter space is large. The following problem is illustrates this point.

For problems with singular boundary conditions like the previous problem, it is clear that high-order models are necessary nearby the source and low-order models can be used away from the source as the solution becomes less peaked. However, the same is not necessarily true for distributed sources. For example, in the following problem an isotropic point source of 2500-keV electrons in a gold cube 1 cm on each face is simulated. The problem setup and analog benchmark is given in **Figure 30** (left). As seen in **Figure 30** (right), the dose is deposited uniformly about the point source located at the origin. It is also of interest to point out that most of the dose is deposited nearby the source.

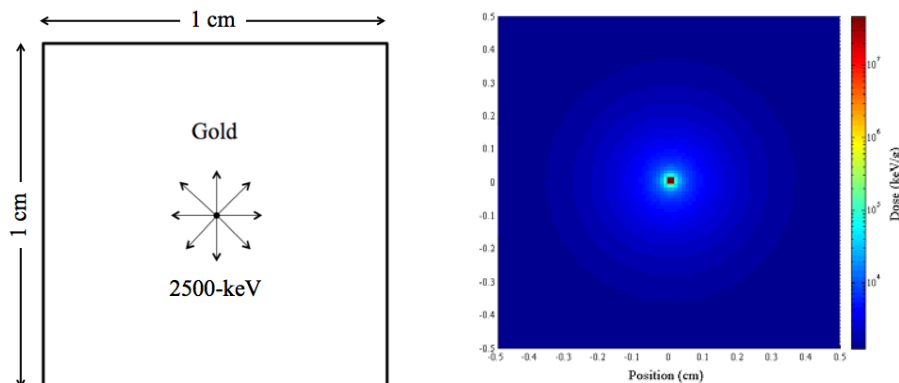


Figure 30: Problem setup (left) and analog benchmark (right) for an isotropic source of 2500-keV electrons in a gold cube.

As seen in **Figure 31**, relatively low-order models can be used to estimate the dose due to distributed sources. The most efficient model tested, single-angle, single-energy, is about 400 times more efficient than the analog simulation and the associated relative error is presented in **Figure 31** (left). By adding another discrete energy the relative error improves as seen in **Figure 31** (middle), but the efficiency decreases to about 300 times faster than the analog simulation. Finally, the most accurate model tested, 2-angles, 2-energies, is presented in **Figure 31** (right). This model provides good agreement, while remaining roughly 180 times more efficient than the analog simulation. Here we showed that accuracy and efficiency is impacted by the source configuration. Again, region dependent models could be applied in this setting for optimization, but more importantly an adaptive cross-section algorithm that incorporates source information and solution information for given problem would improve the MP method.

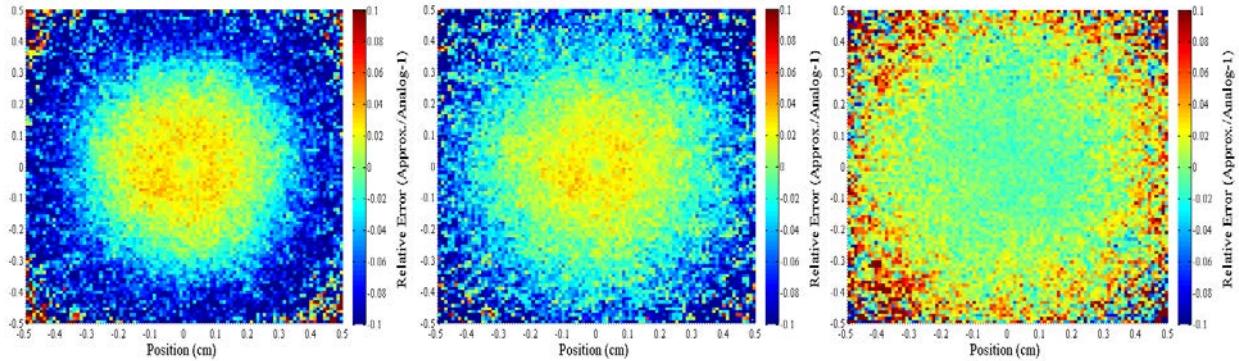


Figure 31: Relative error in discrete 1-Angle, 1-Energy model (left), discrete 2-Angles, 1-Energy model (middle) and discrete 2-Angles, 2-Energies model (right) for 2500-keV electrons in gold cube.

5.4. Comparison with Experiment

In this section, an initial validation of the Moment-Preservation method is presented. Given the nature of the method, the key is to first obtain analog elastic and inelastic DCSs that are in good agreement with the experimental benchmarks of interest. Therefore, the following results are really a validation of the analog DCS models used herein. Initial validation results indicate that the renormalized Moller DCS (see Chapter 3) does not give good agreement with the Lockwood energy deposition data [72]. Use of the Geant4 G4eIonization class in place of the renormalized Moller DCS improved agreement. However, when comparing with the Tabata charge deposition data [73], differences between the renormalized Moller DCS and the G4eIonization class were negligible. Until further development of the analog in-elastic model is completed, use is made of the G4eIonization class (see Chapter 8) for the validation test under consideration in this section to be consistent. Once again, the analog elastic DCS models used are the partial-wave elastic DCSs generated using the ELSEPA code. The first validation test includes comparisons to depth-dose profiles referred to as the Lockwood data [72]. Next, comparisons to charge deposition experiments due to Tabata [73] are presented. In addition to the Lockwood and Tabata data, numerous experimental benchmarks are available for validation test [74, 75, 76, 77, 78, 79, 80, 81]. However, further validation of the MP method remains as future work.

5.4.1. Energy Deposition Profiles

One of the most common electron transport results in basic research is energy deposition, where an accurate description of particle transport is required for different energies in various materials. Below, energy deposition profiles and total energy deposition calculations are compared with experimental results from Lockwood et al. [71]. The Lockwood data was produced by Sandia National Laboratories using a sophisticated calorimetric technique for measuring absolute, high-resolution electron energy deposition profiles in a wide range of materials. The uncertainty of the data is estimated to be from 1.0% to 2.0%.

The comparisons cover low-Z and high-Z materials including carbon, aluminum, molybdenum, and tantalum for pencil beam sources with energies of 500-keV and 1000-keV and angles of incidence of 0° and 60°. In each simulation, 10^5 source particles were transported and the energy deposition profiles are normalized to the mean CSDA range and the depth variable is in terms of a fraction of the mean CSDA range. The primary objective of this comparison is to validate the ROP models that are the subject of this report, but also to demonstrate how well these models perform with respect to the current state-of-art physics models available to Geant4 users. Both accuracy and efficiency results are presented, contrasting the MP method and the default Geant4 electromagnetic physics.

Simulations were completed for three different models where the treatment of elastic scattering varies between each model. These models include an analog elastic scattering model given by the partial-wave DCS, a discrete single-angle DCS, and the geant4 elastic multiple scattering model referred to as the Urban model or the G4UrbanMscModel96 class. Each of the models tested used the same inelastic scattering model and bremsstrahlung model along with the same physics for transporting photons and positrons. The settings associated with the aforementioned physics are in accordance with the Geant4 standard electromagnetic physics list option 3, which was found to give the best agreement with the Lockwood data [82] and enforces the strictest multiple scattering step limitation [83] (this is only relevant to the Urban model). In addition, the maximum step-size was set to 0.01 mm for carbon and aluminum and 0.001 mm for molybdenum and tantalum when using the Urban model (step limits are not required for the analog model or the discrete model).

In general, the energy deposition profiles calculated using the analog model, the ROP model, and the geant4 CH model exhibit behavior similar to the experimental results. The Geant4 physics tends to estimate values higher than the discrete model in the peak energy deposition region, while the discrete model tends to estimate higher values in the tails of the energy deposition profile (see **Figure 32** through **Figure 38**). This is true for both normal incidence and 60° of-normal incidence. The total energy deposition tends to be nearly the same for both the MP method and the Geant4 physics models. For normally incident electrons, the agreement between all models and the experimentally determined total energy deposition is roughly 1-3% relative difference for all materials and energies with exception of 1000-keV electrons on tantalum, which is between roughly 4-5% (see **Table 11**). For of-normal incidence, the agreement between all models and the experimentally determined total energy deposition is roughly 2-4% relative difference (see **Table 12**) for all materials and energies with exception of 1000-keV electrons on molybdenum, which is between roughly 6-7%. While this level of agreement is generally acceptable, it is of interest to develop an analog inelastic model that improves overall agreement to within a few percent relative error.

The timing results are presented in **Table 13** and **Table 14**. For normal incidence, efficiency gains are roughly the same for the MP method and the Geant4 physics. However, for of-normal incidence, the MP method is in all cases a factor of two times faster than the Geant4 physics.

For energy deposition calculations, neither the MP method nor the Geant4 physics overwhelmingly outperform the other. However, the MP method was more efficient for the of-normal incidence simulations. In addition, if an analog model were developed that provides better agreement with experiment, the same level of agreement would be anticipated for the MP method. Therefore, it is important to identify an ideal analog inelastic model as the partial-wave

DCSs are assumed to be most accurate representation of elastic scattering and do not contribute to any disagreement found herein.

Furthermore, no multi-region problems were validated in this section. It is known that material interfaces are problematic for condensed history methods and there are reported discrepancies between the Geant4 physics and the Lockwood data for material interfaces [82]. Validation of the MP method for energy deposition in slabs with material interfaces remains as future work, but it has been shown in the past that the MP method does not suffer from boundary crossing limitations [58, 59, 60]. Therefore, no significant interface discrepancies are anticipated.

Table 11: Total energy deposition comparison for 500-keV and 1000-keV electrons normally incident on aluminum, molybdenum, and tantalum semi-infinite slabs.

Energy (keV)	Material Type	Model Type	Total Energy (keV)	Relative Error
500	aluminum	Analog	472.921	-0.013
		Discrete 1-Angle	471.169	-0.016
		G4EmStandard	468.550	-0.022
1000	aluminum	Analog	958.381	-0.012
		Discrete 1-Angle	954.665	-0.016
		G4EmStandard	953.089	-0.017
500	molybdenum	Analog	383.612	0.028
		Discrete 1-Angle	381.167	0.022
		G4EmStandard	376.032	0.008
1000	molybdenum	Analog	801.527	0.029
		Discrete 1-Angle	795.534	0.021
		G4EmStandard	791.940	0.017
500	tantalum	Analog	323.144	0.023
		Discrete 1-Angle	316.823	0.003
		G4EmStandard	321.674	0.018
1000	tantalum	Analog	681.921	0.052
		Discrete 1-Angle	675.622	0.043
		G4EmStandard	678.301	0.047

Table 12: Total energy deposition comparison for 500-keV and 1000-keV electrons with 60 degrees off-normal incidence on aluminum, molybdenum, and tantalum semi-infinite slabs.

Energy (keV)	Material Type	Model Type	Total Energy (keV)	Relative Error
500	aluminum	Analog	380.501	-0.027
		Discrete 1-Angle	379.573	-0.029
		G4EmStandard	375.752	-0.038
500	molybdenum	Analog	282.940	0.040
		Discrete 1-Angle	279.703	0.028
		G4EmStandard	277.925	0.022
1000	molybdenum	Analog	597.557	0.073
		Discrete 1-Angle	593.249	0.065
		G4EmStandard	591.644	0.062
500	tantalum	Analog	230.202	0.014
		Discrete 1-Angle	226.327	-0.003
		G4EmStandard	232.331	0.023
1000	tantalum	Analog	493.342	0.045
		Discrete 1-Angle	489.207	0.036
		G4EmStandard	495.368	0.050

Table 13: Timing results for energy deposition calculations for 500-keV and 1000-keV electrons normally incident on carbon, aluminum, molybdenum, and tantalum semi-infinite slabs.

Energy (keV)	Material Type	Model Type	CPU time (mins)	Efficiency Gains
1000	carbon	Analog	75	1
		Discrete 1-Angle	3	25
		G4EmStandard	3	25
500	aluminum	Analog	41	1
		Discrete 1-Angle	3	14
		G4EmStandard	2	21
1000	aluminum	Analog	74	1
		Discrete 1-Angle	4	19
		G4EmStandard	3	25
500	molybdenum	Analog	100	1
		Discrete 1-Angle	2	50
		G4EmStandard	2	50
1000	molybdenum	Analog	151	1
		Discrete 1-Angle	3	50
		G4EmStandard	5	30
500	tantalum	Analog	90	1
		Discrete 1-Angle	2	45
		G4EmStandard	1	90
1000	tantalum	Analog	134	1
		Discrete 1-Angle	3	45
		G4EmStandard	3	45

Table 14: Timing results for energy deposition calculations for 500-keV and 1000-keV electrons with 60 degrees off-normal incidence on aluminum, molybdenum, and tantalum semi-infinite slabs.

Energy (keV)	Material Type	Model Type	CPU time (mins)	Efficiency Gains
500	aluminum	Analog	60	1
		Discrete 1-Angle	2	30
		G4EmStandard	5	12
500	molybdenum	Analog	71	1
		Discrete 1-Angle	1	71
		G4EmStandard	2	35
1000	molybdenum	Analog	115	1
		Discrete 1-Angle	2	58
		G4EmStandard	4	29
500	tantalum	Analog	61	1
		Discrete 1-Angle	1	61
		G4EmStandard	2	30
1000	tantalum	Analog	103	1
		Discrete 1-Angle	1	103
		G4EmStandard	2	52

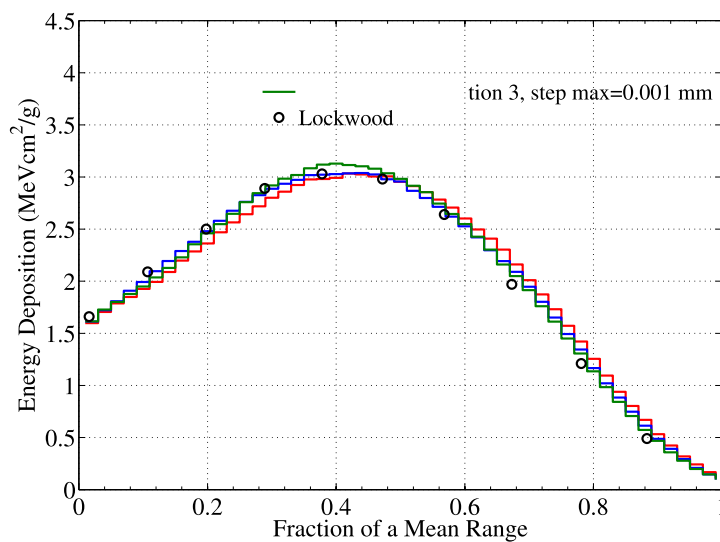


Figure 32: Comparison with Lockwood data for 1000-keV electrons normally on carbon slab.

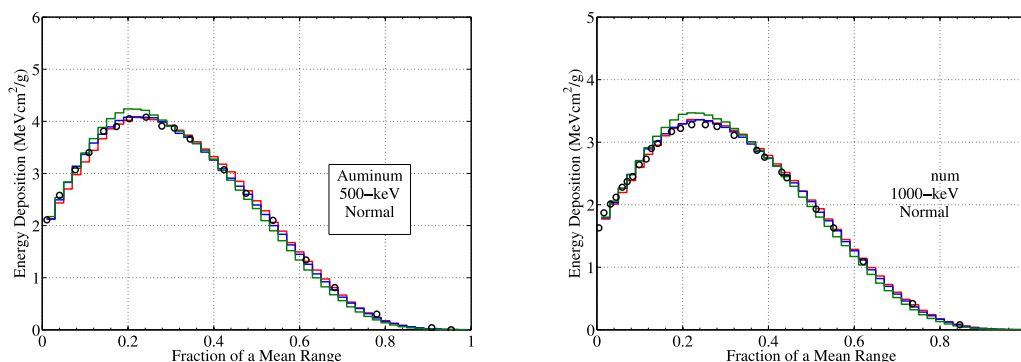


Figure 33: Comparison with Lockwood data for 500-keV (left) and 1000-keV (right) electrons normally on aluminum slab.

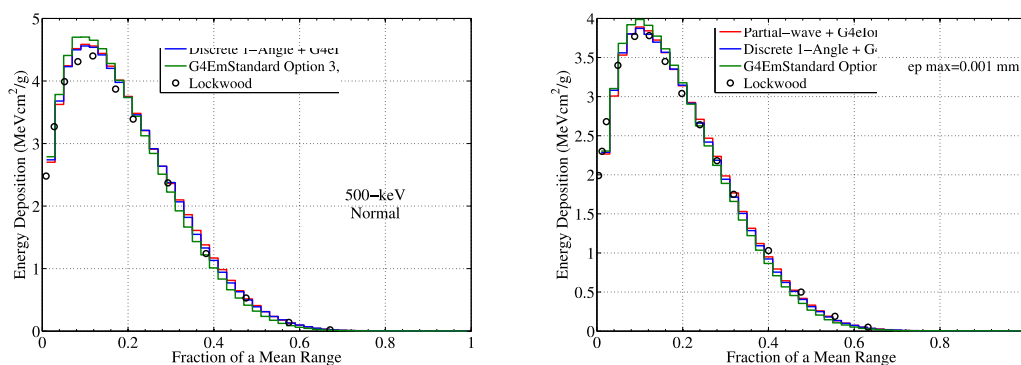


Figure 34: Comparison with Lockwood data for 500-keV (left) and 1000-keV (right) electrons normally on molybdenum slab.

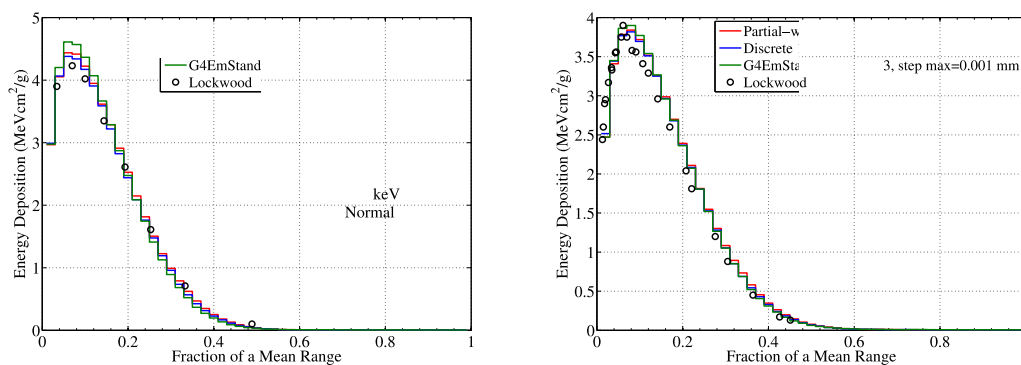


Figure 35: Comparison with Lockwood data for 500-keV (left) and 1000-keV (right) electrons normally on tantalum slab.

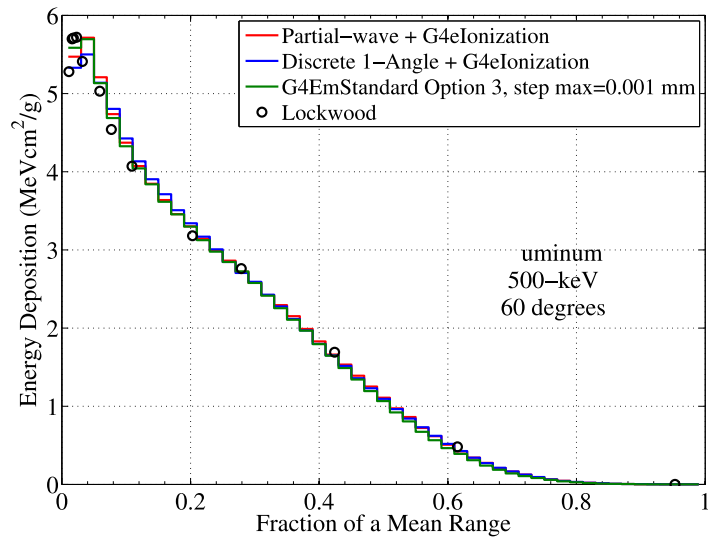


Figure 36: Comparison with Lockwood data for 1000-keV electrons with 60 degrees off-normal incidence on aluminum slab.

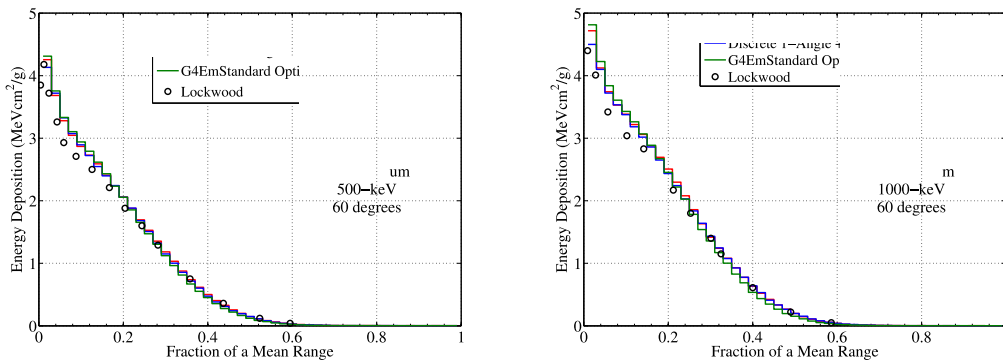


Figure 37: Comparison with Lockwood data for 500-keV (left) and 1000-keV (right) with 60 degrees off-normal incidence on molybdenum slab.

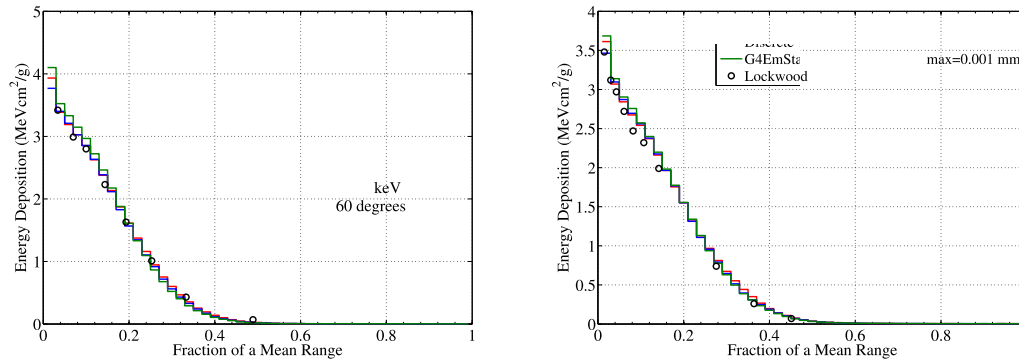


Figure 38: Comparison with Lockwood data for 500-keV (left) and 1000-keV (right) electrons with 60 degrees off-normal incidence on tantalum slab.

5.4.2. Charge Deposition Profiles

Another important electron transport result is charge deposition. Charge deposition is important to understanding charge buildup in nonconductive materials. Below, charge-deposition profiles are compared with experimental results from Tabata et al. [73]. Among the published experimental results of charge deposition distributions, those of Tabata et al. [74] cover the widest regions of absorber atomic number (from 4 to 79) and incident-electron energy (from 4.09 to 23.5 MeV) [73].

Calculations of charge deposition distributions were performed for normally incident electron pencil beams with energies of 5000-keV, 10000-keV, and 20000-keV on aluminum and gold targets of thickness $2.5r_0$, where r_0 is the CSDA range. A total of 2.4×10^5 source particles were simulated. The target regions were divided into 80 sub-regions for scoring (scoring regions are not physical boundaries) for 5000-keV source particles and 40 sub-regions for 10000-keV and 20000-keV source particles. Particles are tracked down to 250-keV.

Figure 39 through **Figure 44**, present comparisons of charge-deposition and dose distributions generated using the partial-wave elastic DCS or a discrete DCS with the default Geant4 inelastic physics for electrons and the default Geant4 physics for positrons and photons. The charge-deposition distributions are compared with experimental results from Tabata et al. [73]. In general the correct behavior of the charge-deposition distribution is captured for all energies and materials tested. In aluminum, agreement with the experimental benchmark is satisfactory with exception of a slight shift in the distribution. In gold, agreement with the experimental benchmark is again satisfactory with exception of the 5000-keV results where the charge deposition is overestimated. Notice that the analog solution and the discrete solution are in excellent agreement. Again, the conclusion is that an analog model that gives good agreement should be identified and it is assumed that the ROP models will provide similar levels of agreement. Further investigation is required to understand the disagreements seen below (in particular, 5000-keV electrons on gold).

The dose results in **Figure 39** through **Figure 44**, do show good agreement in gold but do not in aluminum. This result was not anticipated considering the level of agreement in the previous section and suggests that future validations should be avoided until this disagreement can be identified. Possible sources of the disagreement includes the increased presence of bremsstrahlung radiation at higher energies, an inconsistency between the Geant4 physics implementation and discrete model, or a coding error. Regardless, future work will include the use of an inelastic ROP model based on an improved inelastic DCS, so that reliance on the Geant4 physics is reduced.

Table 15: Timing results for charge deposition calculations for 5000-keV, 10000-keV, and 20000-keV electrons with normally incident on aluminum and gold semi-infinite slabs.

Energy (keV)	Material Type	Model Type	CPU time (hours)	Efficiency Gains
5000	aluminum	Analog	1.8	1
		Discrete 4-Angles	0.009	178
		Discrete 8-Angles	0.02	80
5000	aluminum	Analog	2.7	1
		Discrete 4-Angles	0.01	270
		Discrete 8-Angles	0.03	90
5000	aluminum	Analog	5.8	1
		Discrete 4-Angles	0.02	290
		Discrete 8-Angles	0.05	116
5000	gold	Analog	2.3	1
		Discrete 4-Angles	0.03	77
		Discrete 8-Angles	0.06	38
10000	gold	Analog	4.3	1
		Discrete 4-Angles	0.06	72
		Discrete 8-Angles	0.11	43
20000	gold	Analog	13.8	1
		Discrete 4-Angles	0.2	69
		Discrete 8-Angles	0.3	46

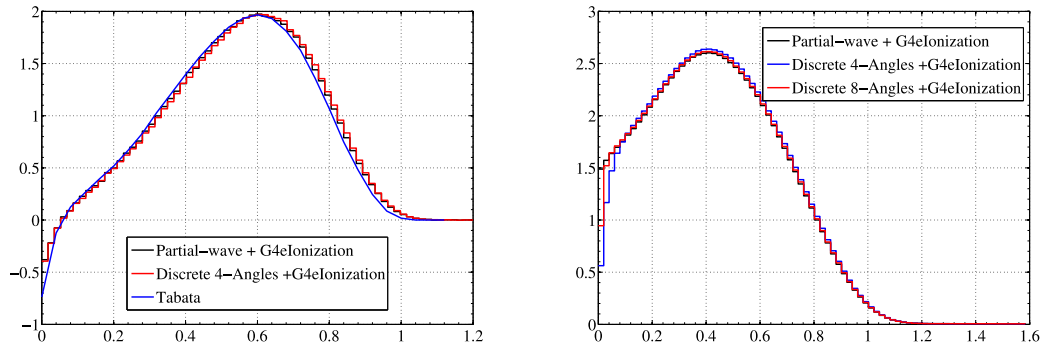


Figure 39: Charge deposition comparison with Tabata data (left) and dose comparison (right) for 5000-keV electrons normally incident on aluminum slab.

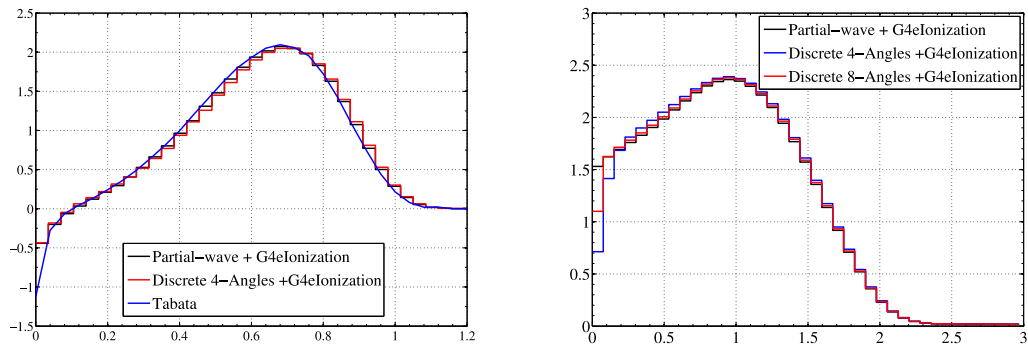


Figure 40: Charge deposition comparison with Tabata data (left) and dose comparison (right) for 10000-keV electrons normally incident on aluminum slab.

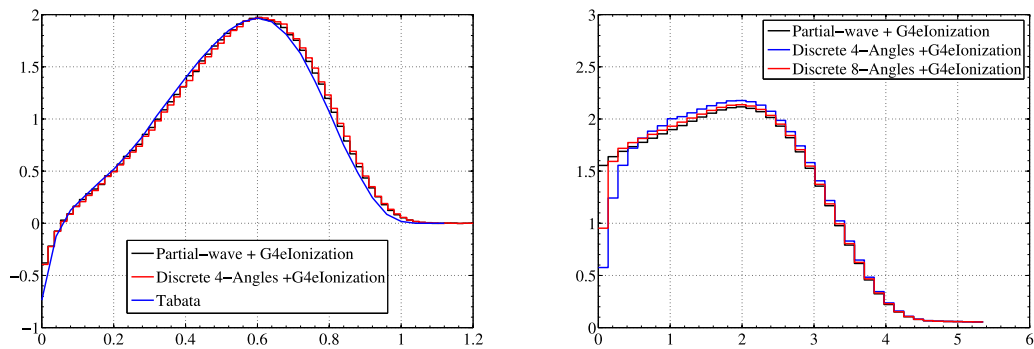


Figure 41: Charge deposition comparison with Tabata data (left) and dose comparison (right) for 20000-keV electrons normally incident on aluminum slab.

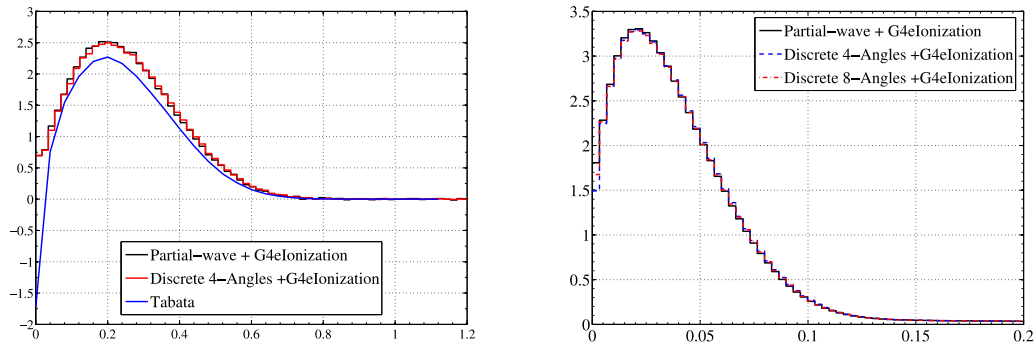


Figure 42: Charge deposition comparison with Tabata data (left) and dose comparison (right) for 5000-keV electrons normally incident on gold slab.

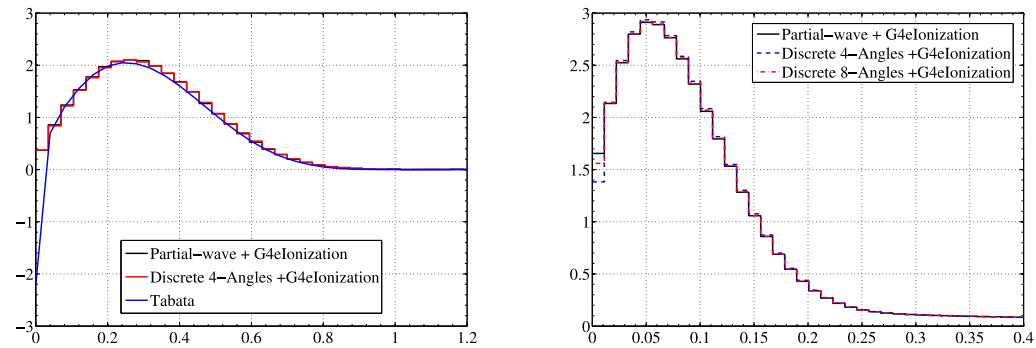


Figure 43: Charge deposition comparison with Tabata data (left) and dose comparison (right) for 10000-keV electrons normally incident on gold slab.

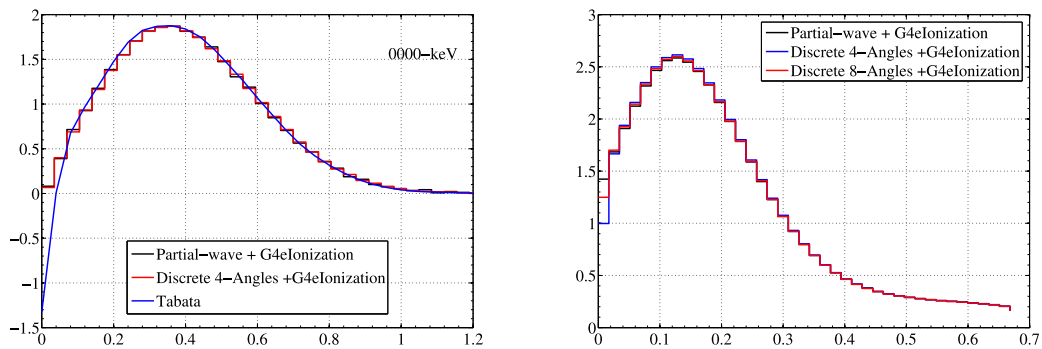


Figure 44: Charge deposition comparison with Tabata data (left) and dose comparison (right) for 20000-keV electrons normally incident on gold slab.

5.5. CEASE Response Function Calculation

Given the experimental validation and the associated level of confidence in the accuracy of the analog DCS models and the ROP DCSs constructed from such models, the CEASE response function calculation is revisited. Here, it is shown that the response function can be generated with an efficient ROP DCS model while remaining accurate. For this calculation, three models were tested each with the same positron, photon, and electron inelastic physics. What varies for each of the models is the elastic scattering physics. An analog model given by the partial-wave elastic DCS is tested and a single-angle discrete model based on the partial-wave elastic DCS is compared. In addition, the response function is also calculated using the default Geant4 electromagnetic physics option 3. In **Figure 45**, response functions generated using each different model are compared. The analog and the discrete model are in excellent agreement, while the Geant4 physics (that is, class II CH with out a user applied step limitation) shows significant disagreement at higher energies. Assuming the analog model is the most accurate, the Geant4 physics tends to under predict the detector response at higher energies. This could be an effect of the collimator, as it is known that the Geant4 physics, without step limitation, tends to overestimate energy deposition in high-Z materials. Therefore, it is possible that electrons do not fully penetrate the collimator because they lose too much energy in the tungsten collimator. See **Figure 46** for an example of trajectories penetrating the collimator. The collimator is in green; the detectors are in blue; and the electron tracks are in red.

The efficiency gains associated with the discrete DCS are outstanding. To complete an analog simulation of 1116 runs for 18 source angles and 62 source energies with 1000 source particles each, it requires roughly 46 processor-days, while for the discrete model it only takes roughly five processor-days. That is an order of magnitude efficiency gain. The CH runs were roughly 10 times faster than the discrete model or 0.5 processor-days.

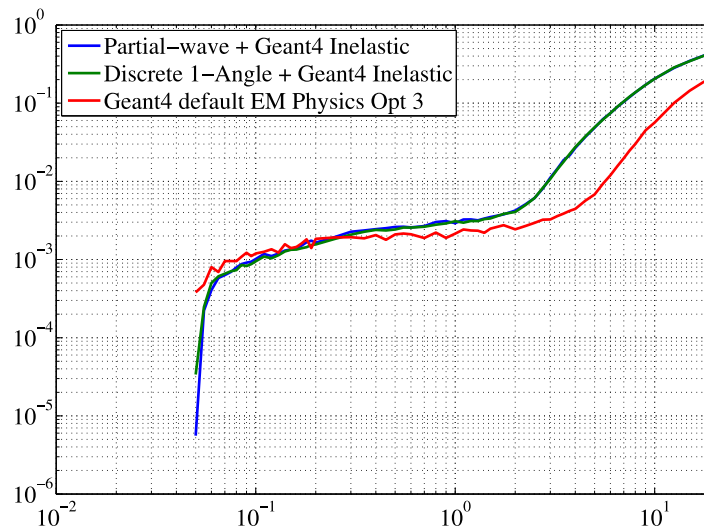


Figure 45: Comparison of response functions generated using the analog model, the discrete model, and the Geant4 multiple-scattering model.

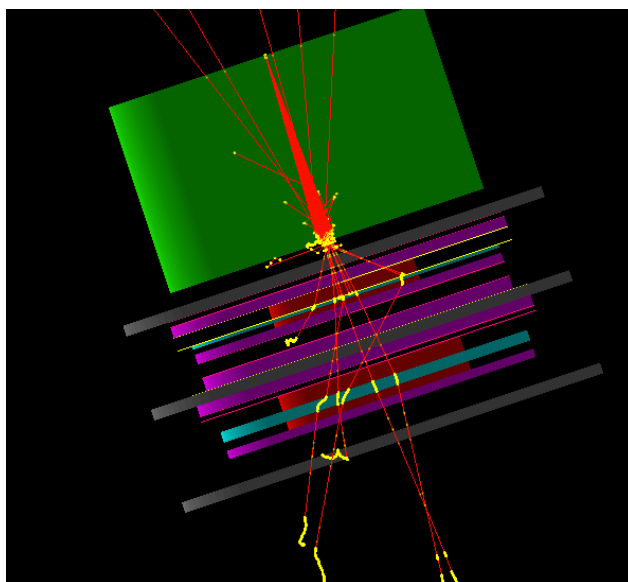


Figure 46: Electrons traversing the CEASE telescope.

5.6. Detector Modeling and Simulation

The following section present related work including the modeling of detectors associated with the AFRL Demonstration and Science Experiment (DsX) detectors for use in response function determination. Modeling and analysis was completed for the Compact Environmental Anomaly Sensor (CEASE), the High Energy Proton Spectrometer (HEPS), and the Low Energy Electrostatic Analyzer (LEESA). Each detector was modeled using MCNPX (Monte Carlo N-Particle Extended) particle transport software. The detector models were completed by constructing an MCNPx input file with detail of the detector consistent with the available information (e.g. detector drawings, and so on).

Given the highest possible fidelity detector models, electron and proton simulations were completed for a wide range of particle energies and angles of incidence. The output or result from the individual simulations was detailed particle-by-particle energy deposition for each region of interest (that is, sensitive detector regions). In the CEASE detector the sensitive regions included two silicon PIPS detectors; whereas, the HEPS detector contains three silicon PIPS detectors and three plastic scintillators, or six sensitive regions.

With detailed energy deposition information for the relevant source particle energies and angles, and detector logic, the response function for various detector channels and or the total response function is determined. To do so, a data processing algorithm is required where the details of such an algorithm are given in [1]. Ultimately, the response functions generated using models built by UNM and the UNM algorithm for data processing were satisfactory. That is, good

agreement was found between the UNM generated response functions for CEASE and HEPS and relevant response functions from Brautigan et al. [1].

The focus for LEESA was on familiarization with the detector system and high fidelity modeling of the detector, rather than conducting analysis. Familiarization with the detector and an extensive model was completed. Once the model was completed, emphasis was shifted to the completing the research under consideration for the grant.

6. CONCLUSIONS

It is of interest to develop an alternative to the CH method that is free of the limitations inherent to CH. The subject of this report, or the Moment-Preserving method, is such an alternative and therefore, the accuracy and efficiency of this method must be demonstrated and contrasted (to some degree) with the CH method. To do so, the theoretical development of the method was discussed in great detail, emphasizing how elements of accuracy and efficiency are inherent to the method, while also providing an exhaustive numerical demonstration including validation of the method.

Through theoretical development, it was shown that in the Moment-Preserving method a reduced order physics (ROP) transport equation is formed by replacing the analog DCS with ROP DCSs that are less peaked with longer mfps. By doing so, solution to the ROP transport equation using a single-event Monte Carlo method is computationally efficient with respect to analog Monte Carlo. To simply replace the analog DCSs with another more ideal DCS requires a process for constructing such a DCS that guarantees accurate results. This is achieved by applying a theory ubiquitous in electrons transport methods, or Lewis theory, that relates moments of the analog DCS to moments of the solution. By recognizing the importance of Lewis theory, a process was developed for constructing ROP DCSs by applying a moment- preservation constraint, where both elastic and inelastic ROP DCSs are constructed such that they preserve some finite number of moments of the analog DCS exactly and higher-order moments are approximated in terms of the lower-order moments. The resulting ROP DCSs preserve key physical moments like the mean scattering cosine, the transport cross-section, the stopping power, and the straggling coefficient, along with any other user specified higher-order moments. Furthermore, by constructing the ROP DCSs such that one point is required to coincide with the nearly-singular point of the analog DCS, the method takes advantage of a convenient cancellation of in-scatter and out-scatter due to these nearly-singular points about zero changes- in-state resulting in a reduction of the total cross-section. Between the moment preserving constraint and the cancellation of the nearly-singular points, moment- preserving ROP DCSs that are less-peaked with a longer mfp (up to four orders of magnitude longer than the analog mfp) can be generated and accurate solutions to the corresponding ROP transport equation can be obtained efficiently. These findings, though satisfactory, only partially satisfy the objective of the research, which is to develop and demonstrate an alternative for electron transport.

To completely satisfy the objectives, a numerical demonstration of the Moment-Preserving method was presented. The results associated with the numerical demonstration, served to extend and modernize the significant body of work completed by Franke and Prinja in 2005 [58]. By extending their study, several key features of this method were addressed including: systematically controllable accuracy, efficiency, mathematical robustness, versatility through the independence of

the method from the form of the analog DCS, flexibility of the method through usage of both the discrete and hybrid DCS, and simplicity easing implementation in transport codes. The accuracy and efficiency of the method was demonstrated through calculation of both differential and integral quantities in both highly-peaked scattering regimes and less- peaked scattering regimes for a wide variety of target materials and source energies. Results including reflected and transmitted angular distributions and energy-loss spectra in thin slabs, longitudinal and lateral distributions in infinite media, dose deposition in 1-D and 2-D slabs, and charge deposition were presented. For the theoretical problems where the method is compared to an analog benchmark, analog level accuracies were achieved with efficiency gains up to three orders of magnitude greater than analog level efficiencies. For the validation results, the accuracies and efficiencies were similar to the default Geant4 electromagnetic physics with a factor of two improvement in efficiency for off-normal incidence source problems. Although the Moment-Preserving method was not a dramatic improvement over the default Geant4 electromagnetic physics, this was a first attempt at validating the method and much work remains in identifying an analog DCS model for inelastic scattering. Improvements in accuracy beyond what was reported herein are anticipated with such an inelastic DCS model. As it stands, the Moment-Preserving is a suitable alternative; however, with these improvements one can expect that the Moment-Preserving method will provide a clear advantage over the default Geant4 electromagnetic physics.

In its current state with regards to accuracy and efficiency, the Moment-Preserving method is a strong alternative to CH methods. Under conditions where CH methods and the Moment-Preserving method provide identical levels of accuracy and efficiency, the Moment-Preserving method has the added advantage of versatility and simplicity. That is, no changes to the source code or the algorithm are required to make significant changes to the underlying physics. The moment-preserving algorithms are completely independent of the form of the analog DCS that ultimately drives the accuracy of this method. Therefore, if an improved elastic or inelastic DCS is developed, one must simply generate an ROP DCS library corresponding to the improved models. In addition, initial implementation of the Moment-Preserving method is straightforward; especially, in transport codes with pre-existing single- scatter algorithms. As a result of the mathematical robustness of the method, no additional algorithms are required beyond what is typically used for a single-scatter algorithm that uses tabulated DCS data. The algorithm simply requires methods for table look-ups to obtain the total-cross section, methods for sampling DCS data without interpolation, and methods for processing the ROP DCS. In Geant4, this required utilization of the existing data classes and base classes for physics models and processes. Any maintenance associated with Moment-Preserving method would be a result of changes to the base classes from which the Moment-Preserving method physics inherit.

Given the accuracy, efficiency, mathematical robustness, versatility, flexibility, and simplicity of the Moment-Preserving method, this method provides a clear alternative to the prevailing electron transport method - Condensed History. This work establishes a modern basis from which further testing of this method will be completed.

REFERENCES

- [1] D. Brautigam, et al., Compact environmental anomaly sensor (CEASE): Response functions, AFRL-VS-HA-TR-2006-1030, Air Force Research Laboratory, Hanscom AFB, MA (March 2006).
- [2] M. J. Berger, Monte Carlo calculation of the penetration and diffusion of fast charged particles, in: Methods in Computational Physics, Vol. 1 of Statistical Physics, Advances in Research and Applications, Academic Press, pp. 135-215, (1963).
- [3] S. Agostinelli, et al., Geant4—a simulation toolkit, NIMA 506, pp. 250-303 (2003).
- [4] L. Evans and P. Bryant, LHC machine, Jinst 3, S08001; DOI: 10.1088/1748-0221/3/08/S08001 (2008).
- [5] V. N. Ivanchenko, et al., Geant4 electromagnetic physics for LHC upgrade, J. Physics: Conf. Ser. (2014).
- [6] T. Aso, et al., A geant4 based simulation for proton therapy, Computing in High Energy Physics, CHEP 2010, Taipei, Taiwan (October 2010).
- [7] H. Paganetti, et al., Clinical implementation of full Monte Carlo dose calculation in proton beam therapy, Phys. Med. Biol., 53, pp. 4825-4853 (2008).
- [8] D. Brautigam, Compact environmental anomaly sensor (CEASE): Geometric factors, AFRL-RV-HA-TR-2008-1129, Air Force Research Laboratory, Hanscom AFB, MA (2008).
- [9] M. Y. Kim, J. W. Wilson, and F. A. Cucinotta, Description of transport codes for space radiation shielding, Health Phys., 10, pp. 621-639 (2012).
- [10] E. R. Parkinson, Monte Carlo analysis of the EMP response of a random-lay cable, IEEE Trans. Nucl. Sci. NS-29, pp. 1920-1923 (1982)
- [11] G. I. Bell and S. Glasstone, Nuclear Reactor Theory, Van Nostrand Reinhold Inc., New York (1970).
- [12] L. Carter, and E. Cashwell, Particle transport simulation with the Monte Carlo method, TID 36607, Los Alamos Scientific Laboratory, Technical Information Division, Los Alamos, NM (1975).
- [13] B. G. Carlson, Solution of the transport equation by S_n approximations, LA 1891, Los Alamos Scientific Laboratory, Los Alamos, NM (1955).
- [14] F. Salvat, J. M. Fernandez-Varea, and S. Segui, Analog electron physics interaction cross-sections, in: Advanced Monte Carlo for Radiation Physics, Particle Transport Simulation (2001).

- [15] S. M. Seltzer, An overview of ETRAN Monte Carlo methods, in: T. M. Jenkins, W. R. Nelson, A. Rindi (Eds.), Monte Carlo Transport of Electrons and Photons, Vol. 38 of Ettore Majorana International Science, Physical Sciences, Plenum Press, pp. 153-181 (1988).
- [16] G. Wentzel, Implementation of the model of multiple scattering based on 00047, Z. Phys., 40, p. 590 (1927).
- [17] F. Salvat, A. Jablonski, and C. J. Powell, ELSEPA—Dirac partial-wave calculation of elastic scattering of electrons and positrons by atoms, positive ions and molecules, Comp. Phys. Comm., 165, pp. 157-190 (2005).
- [18] R. Evans, The Atomic Nucleus, tenth printing Edition, McGraw-Hill, New York (1955).
- [19] S. T. Perkins, D. E. Cullen, and S. M. Seltzer, Tables and graphs of electron interaction cross-sections from 10 eV to 100 GeV derived from the LLNL evaluated electron data library (EEDL), Z=1-100, UCRL-50400, University of California Radiation Laboratories (1997).
- [20] Author Unknown, MacCallum, Monte Carlo Calculations of Electron Backscattering, Bulletin of the American Physical Society Series II, Vol 5, p. 379 (1960).
- [21] J. M. Fernandez-Varea, D. Liljequist, S. Csillag S, R. Rätty, and F. Salvat, Monte Carlo simulation of 0.1-100 keV electron and positron transport in solids using optical data and partial wave methods, Nucl. Instr. Meth. B, 108, pp. 35-50 (1996).
- [22] G. Hughes III, Recent developments in low-energy electron/photon transport for MCNP6, Progress in Nuclear Science and Technology, International Conference on Radiation Shielding and 17th Topical Meeting of the Radiation Protection and Shielding Division of ANS, Nara, Japan (2012).
- [23] Ivanchenko, et al., Recent improvements in geant4 electromagnetic physics modeling, Progress in Nucl. Sci. Tech., 2, pp. 898-903 (2011).
- [24] F. Salvat, J. M. Fernandez-Varea, and J. Sempau, PENELOPE-2011: A Code System for Monte Carlo Simulation of Electron and Photon Transport, Universitat de Barcelona (July 2011).
- [25] W. R. Nelson, H. Hirayama, and D. W. O. Rogers, The EGS4 Code System, Stanford Linear Accelerator Center, SLAC-265, Menlo Park, CA (1985).
- [26] W. Bothe, Handbuch der Physik 22, unpublished, 1 (1933).
- [27] B. Rossi, High Energy Particles, Prentice-Hall, Englewood Cliffs, New Jersey (1952).
- [28] U. Fano, Degredation and range straggling of high-energy radiations, Phys. Rev., 92, p. 328 (1953).

- [29] R. D. Birkhof, Handbuch der Physik 34, unpublished, 53 (1958).
- [30] S. Goudsmit and J. L. Saunderson, Multiple scattering of electrons, Phys. Rev., 57, pp. 24-29 (1940).
- [31] S. Goudsmit and J. L. Saunderson, Multiple scattering of electrons. ii, Phys. Rev., 58, pp. 36-42 (1940).
- [32] L. Landau, On the energy loss of fast particles by ionization, J. Phys., 8, p. 201 (1944).
- [33] P. V. Vavilov, Ionization losses of high-energy heavy particles, Sov. Phys. JETP, 5 (4), pp. 920-923 (1957).
- [34] D. W. O. Rogers and A. F. Bielajew, A comparison of EGS and ETRAN, in: T. M. Jenkins, W. R. Nelson, A. Rindi (Eds.), Monte Carlo Transport of Electrons and Photons, Vol. 38, Ettore Majorana International Science, Physical Sciences, Plenum Press, pp. 323-342 (1988).
- [35] S. M. Seltzer, and M. J. Berger, Transmission and reflection of electrons by foils, Nucl. Instr. Meth., 119, p. 157 (1974).
- [36] D. W. O. Rogers, Low energy electron transport with EGS, Nucl. Instr. Meth. A A227, p. 535 (1984).
- [37] E. W. Larsen, Generalized Fokker-Planck approximations of particle transport with highly forward-peaked scattering, Ann. Nucl. Energy, 19, pp.701-714 (1992).
- [38] A. Bielajew, and D. W. O. Rogers, PRESTA: The parameter reduced electron-step transport algorithm for electron Monte Carlo transport, Nucl. Instr. Meth. B, 18, pp. 165-181 (1986).
- [39] D. Jensen, Monte Carlo calculation of electron multiple scattering in thin foils, Ph.D. thesis, Naval Postgraduate School (1988).
- [40] R. L. Keith, and R. P. Kensek, Order-of-convergence study of a condensed-history algorithm implementation, in: International Conference on Mathematics, Computational Methods and Reactor Physics 2009, American Nuclear Society, Saratoga Springs, New York, on CD-ROM, 2009.
- [41] G. C. Pomraning, The Fokker-Planck operator as an asymptotic limit, Math. Mod. Meth. Appl. Sci., 2, pp. 21-36 (1992).
- [42] C. Borgers, and E. Larsen, Fokker-Planck approximation of monoenergetic transport processes, Trans. Am. Nucl. Soc., 71, pp. 235-236 (1994).
- [43] P. A. Haldy, and J. Ligou, A multigroup formalism to solve the Fokker-Planck equation characterizing charged particle transport, Nucl. Sci. Eng., 74, pp. 178-184 (1980).
- [44] T. M. Tran, and J. Ligou, An accurate numerical method to solve the linear Fokker-Planck equation characterizing charged particle transport, Nucl. Sci. Eng., 79, pp. 269-277 (1981).

- [45] J. E. Morel, Fokker-Planck calculations using standard discrete ordinates transport codes, Nucl. Sci. Eng., 79, pp. 340-356 (1981).
- [46] J. E. Morel, An improved Fokker-Planck angular differencing scheme, Nucl. Sci. Eng., 89, pp. 131-136 (1985).
- [47] J. Ligou, Fusion reaction product transport in inertially confined plasmas, in: Proc. ANS-ENS Int. Topl. Mtg. Advances in Mathematical Methods for the Solution of Nuclear Engineering Problems, Fachinformationszentrum Energie, Physik, Mathematik GmbH, Karlsruhe, West Germany (1981).
- [48] K. Przybylski and J. Ligou, Numerical analysis of the Boltzmann equation including Fokker-Planck terms, Nucl. Sci. Eng., 81, pp. 92-109 (1981).
- [49] M. Caro and J. Ligou, Treatment of scattering anisotropy of neutrons through the Boltzmann-Fokker-Planck equation, Nucl. Sci. Eng., 8, pp. 242-252 (1983).
- [50] M. Landesman and J. E. Morel, Angular Fokker-Planck decomposition and representation techniques, Nucl. Sci. Eng., 103, pp. 1-11 (1989).
- [51] D. P. Sloan, A new multigroup Monte Carlo scattering algorithm for neutral and charged-particle Boltzmann and Fokker-Planck calculations, SAND83-7094, Sandia National Laboratories, Albuquerque, NM (1983).
- [52] J. E. Morel, L. J. Lorence, Jr., R. P. Kensek, J. A. Hableib, and D. P. Sloan, A hybrid multigroup/continuous-energy Monte Carlo method for solving the Boltzmann-Fokker-Planck equation, Nucl. Sci. Eng., 124, pp. 369-389 (1996).
- [53] G. C. Pomraning, Higher order Fokker-Planck operators, Nucl. Sci. Eng., 124, pp. 390-397 (1996).
- [54] A. K. Prinja and G. Pomraning, A generalized Fokker-Planck model for transport of collimated beams, Nucl. Sci. Eng., 137, pp. 227-235 (2001).
- [55] C. L. Leakas and E. W. Larsen, Generalized Fokker-Planck approximations of particle transport with highly forward-peaked scattering, Nucl. Sci. Eng., 137, pp. 236-250 (2001).
- [56] H. W. Lewis, Multiple scattering in an infinite medium, Phys. Rev., 78, pp. 526-529 (1950).
- [57] A. K. Prinja, Lewis theory for energy straggling in thin layers, Nucl. Instr. Meth. B, 330, pp. 99-102 (2014).
- [58] B. C. Franke and A. K. Prinja, Monte Carlo electron dose calculations using discrete scattering angles and discrete energy losses, Nucl. Sci. Eng., 149, pp. 1-22 (2005).

- [59] D. Dixon, A. K. Prinja, and B. C. Franke, Geant4 implementation of a novel single-event Monte Carlo method for electron dose calculations, Trans. Am. Nucl. Soc. (2015)
- [60] D. Dixon, A. K. Prinja, and B. C. Franke, Application of the generalized Boltzmann Fokker-Planck method to electron partial-wave expansion elastic scattering differential cross sections within the geant4 toolkit, in: RPSD 2014, Radiation Protection and Shielding Division of the ANS, Knoxville, Tennessee (2014).
- [61] B. C. Franke, A. K. Prinja, R. P. Kensek, and L. J. Lorence, Discrete scattering-angle model for electron pencil beam transport, Trans. Am. Nucl. Soc., 86, pp. 206-208 (2002).
- [62] B. C. Franke, A. K. Prinja, R. P. Kensek, and L. J. Lorence, Ray effect mitigation for electron transport with discrete scattering-angles, Trans. Am. Nucl. Soc., 87, pp. 133-135 (2002).
- [63] ICRU Report No. 77, Elastic scattering of electrons and positrons, Journal of ICRU 7, date unknown.
- [64] E. Benedito, J. M. Fernandez-Varea, F. Salvat, Mixed simulation of the multiple elastic scattering of electrons and positrons using partial-wave differential cross-sections, Nucl. Instr. Meth. B, 174, pp. 91-110 (2001).
- [65] R. M. Sternheimer and R. F. Peierls, General Expression for the Density Effect for the Ionization Loss of Charged Particles, Phys. Rev. B, 3, p. 3681 (1971).
- [66] ICRU Report No. 37, Stopping powers for electrons and positrons, Journal of ICRU, date unknown.
- [67] D. Dixon, A computationally efficient moment-preserving Monte Carlo electron transport method with implementation in geant4, Ph.D. thesis, University of New Mexico (2015).
- [68] W. Gautschi, Numerical Analysis, second Edition, Birkhauser, New York, NY, (2012). [69]
- [69] G. H. Golub, Some modified matrix eigenvalue problems, SIAM Rev., 15 (2), pp. 318-334 (1973).
- [70] G. H. Golub and J. H. Welsch, Questions of numerical condition related to orthogonal polynomials, Studies in Numerical Analysis, 24, pp. 140-177 (1984).
- [71] G. H. Golub and J. H. Welsch, Calculation of Gauss quadrature rules, Math. Comp., 23 (106), pp. 221-230 (1969).
- [72] G. J. Lockwood, L. E. Ruggles, G. H. Miller, and J. A. Halbleib, Calorimetric measurement of electron energy deposition in extended media: theory vs. experiment, SAND79-0414, Sandia National Laboratories, Albuquerque, NM (1987).

- [73] T. Tabata, P. Andreo, K. Shinoda, and R. Ito, Depth profiles of charge deposition by electrons in elemental absorbers: Monte Carlo results, experimental benchmarks and derived parameters, Nucl. Instr. Meth. B, 95, pp. 289-299 (1995).
- [74] T. Tabata, R. Ito, S. Okabe, and Y. Foujita, Charge distribution produced by 4- to 24-MeV electrons in elemental materials, Phys. Rev. B, 3 (3), pp. 572-583 (1971).
- [75] T. Tabata, P. Andreo, and R. Ito, Energy-deposition distributions in materials irradiated by plane-parallel electron beams with energies between 0.1 and 100 MeV, Atomic Data and Nuclear Data Tables, 56, pp. 105-131 (1994).
- [76] T. Tabata, P. Andreo, K. Shinoda, and R. Ito, Range distributions and projected ranges of 0.1 to 100-MeV electrons in elemental absorbers, Nucl. Instr. Meth. B, 108, pp. 11-17 (1996).
- [77] E. H. Darlington, Backscattering of 10-100 keV electrons from thick targets, J. Phys. D: Appl. Phys., 8, pp. 85-93 (1975).
- [78] P. Libby, G. Hughes III, and J. Goorley, Electron transmission and backscatter verification calculations using mcnp5, LA-UR-03-5751, Los Alamos National Laboratory, Los Alamos, NM (2003).
- [79] B. A. Faddegon, et al., Accuracy of EGSnrc, Geant4, and PENELOPE Monte Carlo systems for simulation of electron scattering in external beam radiotherapy, Phys. Med. Biol., 54, pp. 6151-6163 (2009).
- [80] S. Elles, V. N. Ivanchenko, M. Marie, and L. Urb', Geant4 and Fano cavity test: where are we?, J. Phys.: Conf. Ser. 102 (2009).
- [81] E. Poon, J. Seuntjens, and F. Verhaegen, Consistency test of the electron transport algorithm in the geant4 Monte Carlo code, Phys. Med. Biol., 50, pp. 681-694 (2005).
- [82] O. Kadri, V. N. Ivanchenko, F. Gharbi, and A. Trabelsi, Geant4 simulation of electron energy deposition in extended media, Nucl. Instr. Meth. B, 258, pp. 381-387 (2007).
- [83] V. N. Ivanchenko, O. Kadri, M. Marie, and L. Urb', Geant4 models for simulation of multiple scattering, J. Phys.: Conf. Ser. 219 (2010).

LIST OF SYMBOLS, ABBREVIATIONS, AND ACRONYMS

AFRL	Air Force Research Laboratory
DCS	Differential Cross Section
GBFP	Generalized Boltzmann Fokker-Plank
MFP	Mean Free Path
UNM	University of New Mexico

DISTRIBUTION LIST

DTIC/OCF	
8725 John J. Kingman Rd, Suite 0944	
Ft Belvoir, VA 22060-6218	1 cy
AFRL/RVIL	
Kirtland AFB, NM 87117-5776	2 cys
Official Record Copy	
AFRL/RVBXR/Adrian Wheelock	1 cy